THE FLORIDA STATE UNIVERSITY

COLLEGE OF ARTS AND SCIENCES

AUTONOMOUS AND GUIDED MOTION OF ACTIVE COMPONENTS AT INTERFACES

By

PRAJNAPARAMITA DHAR

A Dissertation submitted to the
in partial fulfillment of the
requirements for the degree of
Doctor of Philosophy

Degree Awarded:
Spring Semester, 2008

The members of the Committee approve the Dissertation of Prajnaparamita Dhar defended on .

Thomas Fischer
Professor Directing Dissertation

Wiedenhöver
Outside Committee Member

Oliver Steinbock
Committee Member

Brian Miller
Committee Member

The Office of Graduate Studies has verified and approved the above named committee members.

This dissertation is dedicated to ma, baba, Pinu, dadu and Prasad.

ACKNOWLEDGEMENTS

First and foremost, I sincerely thank my dissertation advisor, Dr. Thomas Fischer. He has been a constant source of encouragement, inspiration and support. This work would not have been possible without his incredible technical advice, personal guidance, enthusiasm, and understanding. I have learnt a lot from him during the course of my PhD. I will remain for ever grateful to him. I hope he realizes how much my association with him means to me.

I would also like to thank my collaborators, Priya Pal and Dr. Brian Miller at the Florida State University; Yang Wang, Yanyan Cao , Dr. Timothy Kline, Dr. Ayusman Sen and Dr. Thomas Mallouk at the Pennsylvania State University and Vikram Prasad and Eric Weeks at Emory University. This work would not have been possible without their collaboration and their promptness and willingness to work together. Thanks are due to Dr. Joan Hare, from whom I have not just learnt about cell culture but a lot more. I would also like to acknowledge Donny Magana for helping with all the SQUID measurements.

A special thank-you to Dr Robert Fulton for "adopting" me and for being there. I would like to thank Dr. Oliver Steinbock for all the support during difficult times and all the google sessions which increased my trivia I.Q. Thanks to Dr. Harry Kroto for giving me a chance to contribute to his GEO mediasite, which I thoroughly enjoyed.

I would also like to thank my lab alumni, Hanzhen, Jing, Pietro and all the others for making the office/lab a fun place to work in.

Last but not the least, I would like to thank committee member, Dr. Ingo Wiedenhöver, and faculty members Dr. Sanford Saffron, Dr. Colin Byfleet, and Dr. Naresh Dalal for their support.

Since no amount of thanking would be enough, I would only like to mention my parents, brother, grandfather and fiance, Prasad, for always being there for me. You are, therefore I am.

TABLE OF CONTENTS

LIST OF TABLES

LIST OF FIGURES

ABSTRACT

Nature presents active components in the form of proteins and molecular motors that are involved in locomotion and intercompartmental transport. Inspired by nature, this dissertation focuses on presenting experimental means to understand the motion of active components at interfaces. Active Components are defined as components that either autonomously move or start to move in a viscous fluctuating environment. We investigate mechanisms by which energy may be converted into directed motion in case of synthetic nanomotors. Strategies for achieving guided motion along predetermined paths by overcoming fluctuations are explored. In addition we attempt to use dissipation in these systems to achieve guided motion at interfaces. Thus, this dissertation lays some of the foundations necessary for an understanding and smart design of synthetic motors.

CHAPTER 1

Introduction

Movement is an essential concept in all living organisms. On the macro scale, animals and microbes move towards their food and away from their enemies. Even on the micro scale, nutrients and other materials need to be transported to and from various locations. Living organisms either depend on advective flow or on molecular motors for transport. Examples of advective flow include the motion of blood transporting nutrients in animals, and water delivering minerals from the soil to the leaves in plants. Nature presents her own set of molecular motors that have been in use and perfected for performance and design for billions of years. A vast majority of the natural molecular motors are protein-based. Protein-based natural molecular motors are involved in performing various cellular tasks, including, but not limited to, transport of molecular cargo, cell trafficking, and energy conversion by catalyzing reactions. Rotary motors, like ATP-synthase, [2] are involved in the generation of ATP (adinosine triphosphate), the energy currency of biological systems [3].

Transport motors, such as kinesin and myosin motors, are tiny vehicles that transport molecular cargoes (organelles, lipids or proteins) [4]. These motors move unidirectionally along pathways or tracks composed of protein polymers (actin filaments and microtubules), which depend on ATP as fuel for their proper functioning. Unicellular organisms, such as *E.coli*, depend on flagellar motion for their motility to seek more favorable conditions. The helical filaments of the flagella extending out of the body of the organism are connected to molecular motors. The rotary motion of these motors helps the bacteria to swim. Instead of depending on ATP for energy, these motors are powered by energy stored in proton gradients generated across a phospholipid membrane. [5] The flagellar motors allow the bacteria to move with speeds of 25 $\mu m/s$ with direction reversals occurring approximately 1 per second [6]. Whatever the actual mechanism of operation, a common principle followed

by each of these motors is the use of catalysis to convert chemical energy to mechanical energy.

As the race for miniaturized machines continues in the modern world, the exquisite solutions of nature in the form of these naturally occurring biological motors has been a constant source of inspiration for the scientists. Conceptualizing, designing, and building artificial nanomachines by mimicking nature have become a few of the great endeavors in contemporary science.

Advancement in the fields of microfluidics and nanofluidics have also influenced the development of miniaturized devices. A microfluidic device usually consists of micron-sized open or closed channels through which small amounts of fluids are manipulated. The integration of various complex functions allows these devices to perform as efficient miniaturized machines, which were, in fact, primarily developed to serve as miniaturized analytical tools.

The unique ability of microfluidic devices to process microliter volumes of complex fluids with speed and efficiency, along with their properties of small size, low volume requirement of samples, short reaction time and rapid analysis without the need for an expert operator, provides lab-on-chip and microfluidic technologies tremendous potential to serve as portable point-of-care medical diagnostic systems [7–9]. Such cheap and efficient point-of care diagnostic tools can enable better and more efficient diagnosis of infectious diseases and could be easily affordable in the developing countries, where poverty and diseases are strongly correlated. A typical vision of the point of care device in diagnostics is the ability to use a single chip, about the size of a credit card, connected to desktop-scale peripheral instruments that would require only a microliter of biological fluid to efficiently analyze the sample to detect a patients condition. These devices are therefore of great interest to safety, military and health departments, who would greatly benefit from having portable chemical detection systems. Presently, most of the transport on microfluidic chips however involves advective flow of the suspended or dissolved material. The generic components that form the essential elements of the microscopic "factories" on a chip (lab-on-chip) require a variety of devices, such as pumps, valves, mixers and microanalytical detectors [10]. Efforts are on to develop active components (involving active actuation), like valves [11, 12],micro-stirrers, and micropumps [13], which may be fine tuned or better controlled to work more efficiently on a microchip. Apart from using cheap and flexible organic, plastic, or electric

components researchers are also looking for better ways to control or tune components. One of the ideas is to use molecular devices, which could propel in small amounts of fluid, and at the same time work as micropumps [14], micro or nanorotors, and actuators. Moreover, using molecular machines in the active transport of fluid or material, mimicking the active transport in biology, would further improve the efficiency of the microfluidic devices.

In addition to the more widely used applications towards faster and more reliable analysis, microfluidics and nanofluidics provide more realistic model studies at the system level of active transport in biology. Scientists and bioengineers, inspired by the active transport in biology are extensively using the two most studied motor proteins, kinesin and myosin, to study their behavior in open and closed micron and submicron sized channels [15–17]. These molecular motors seemed like the most obvious choice for such studies since they are already available in nature, are designed to move along the cytoskeleton in a directed manner, have the ability to bind cargo, and also possess mechanisms that regulate their activity [18]. The kinesin and myosin are extremely efficient in converting chemical energy to mechanical energy having an efficiency exceeding 50% [19, 20], they move very fast (example: kinesin makes 100 steps of length 8 nm per second) and have specific binding to their complementary filaments (microtubules for kinesin, actin filaments for myosin). The kinesin and myosin motors are used extensively in combination with the microfluidic devices where they mimic typical systems involved in active transport within cells or in biology in a non biological environment. For example, the submicron sized closed channels where microtubules have been confined by van den Heuvel et al. [21], mimic the dimensions of axons, in which motor-driven transport plays a central role. These model systems are studied to understand the working of molecular motors in nature.

Apart from being involved in the biological transport, biomolecular motors can also exert localized forces on nanostructures. Thus, they can cause conformational changes, such as the stretching of coiled DNA molecules into a linear configuration [22], or the rupture of intermolecular bonds. Molecular motors can also push supramolecular assembly and disassembly processes away from chemical equilibrium and generate dynamic, nonequilibrium structures [23].

One of the major challenges faced while using these biomolecular hybrid motors is their compatibility in synthetic environmental conditions and their limited lifetimes (presently in the orders of hours to a few days [24]). Although biological nanomotors are efficient

machines, they are limited by their instability and restrictions while functioning in non-biological environmental conditions. Longterm storage of these nanomotors in their inactive state, although not impossible, is not as yet completely efficient. They are also limited by their small power density. Furthermore, while nature has the ability to maintain and repair damaged molecular systems, current techniques in nanotechnology are not capable of such complex repair mechanisms. Successful development of complex nanotechnology therefore requires synthetic systems that can tolerate a more diverse range of conditions than biological machines, and work efficiently with longer lifetimes in synthetic environments.

Being inspired by the active transport in cells, involving the kinesin and myosin proteins, one could build synthetic prototypes, where we would have complete control on the directionality of the motors. Although various synthetic nanomotors have been reported in the recent years, compared to the molecular motors occuring in nature, a major difficulty still lies in achieving control of the motion of these nanomotors. It is, of course, true that nature did have a head start of 4.6 billion years compared to humans. It can be safely said that achieving control over the directionality of nanomotors remains one of the important challenges in science and engineering. Control on the micron and nano scale is especially desirable for obtaining motors working in a synthetic environment for application in devices involving active transport through a fluid.

As mentioned above, a common principle governing the function of the biological motors is the conversion of free chemical energy of the surroundings into useful work by catalysis. Although the work done by the motors involves co-ordination between all the mechanistic pathways, individual protein motors are able to harvest local chemical energy independent of one another and operate autonomously. On the other hand, most of the synthetic nanomotors presently developed depend on external stimuli for their fuel/energy and control. Stimuli-responsive rotaxanes (molecular shuttles), the earliest examples of artificial molecular motors, depend on external stimuli like light, redox chemistry [25–27], pH changes [28], and cis-trans isomerization triggered by light for achieving linear molecular motors, molecular rotors, molecular switches and valves [29].

It has been noticed that more often than not asymmetry in the system holds the key to achieving directional control on molecular motors. Indeed, Brownian motors in nature efficiently use the *Brownian ratchet effect* to achieve net directional movements. Limited (120°) unidirectional rotation around a single carbon carbon bond in a modified molecular

ratchet was achieved by Kelly and co workers, using phosgene as the chemical fuel [30]. Light may also be used as a fuel for continuous unidirectional rotary motion where it triggers the cis-trans isomerization of a carbon-carbon double bond, which in turn allows for a 180° rotation of one part of the molecule with respect to the other [29]. Rotaxanes based systems containing a ring component that shuttles reversibly between shafts, controlled by various external stimuli are typical molecular machines that perform translation motion. Balzani and co-workers have developed an autonomous photo-driven rotaxane to convert light-driven motion in these molecules to useful work [31]. Artificial molecular muscles, where two interlocked rotaxanes allow for elongation and contraction by binding different metal ions, have also been reported. Multi component molecular machines, where mechanical motion of different units work in concert, have been constructed recently. The rotary motion of one part of the multicomponent molecular machine is coupled to the linear motion of another part, for example a "molecular elevator" and a "nanocar" [32].

It is very important to carefully consider the various forces at play when designing a molecular motor. The force of gravity, typically active in the macroscopic world, has little or no influence on the machines in the nanoworld. On the other hand, random thermal fluctuations due to Brownian motion play a significant part in the proper functioning of these motors. Moreover, dissipation becomes a major concern upon miniaturization. To function in such "fluctuating" environment, the molecular motors can either accept the dominance of thermal fluctuations and exploit it to their advantage, or overcome it. Most of the molecular motors operating on the principle of the Brownian ratchet system harness Brownian fluctuations selectively to achieve net directed motion. To design molecular motors that can overcome the Brownian motion one can either make micrometer sized devices moving in solution, or immobilize machines on a surface without the machines losing their functionality. Berna et al. [33] have reported the successful directional transport of a liquid droplet on a photo-responsive surface created by using the nanometer displacement of the components of light-switchable molecular shuttles to expose or conceal fluoro-alkane residues, and thereby modify the surface properties. Light driven unidirectional molecular rotors have been immobilized on nanoparticle gold surfaces to yield an azimuthal motor. Microscale glass rods could be rotated when placed on a liquid crystal doped with light driven molecular motors [34].

Immobilizing molecular motors at surfaces is a step forward in their direct application in

developing more efficient microfluidic devices. Most of the linear and rotary motion thus far achieved by the synthetic molecular motors have been on the nanometer scale. However, the ultimate goal of scientists is to integrate the molecular motion to achieve directed macroscopic motion, for example by mimicking the operation of myosin/actin driven movement of muscle. Achieving macroscale motion would be especially useful for active motion of components in microfluidic devices. Synthetic motors that can sort, transport, and drop off cargo would make the functioning of lab-on-chip devices more robust and efficient. This would help not just the development of analytical devices but also build a platform outside the biological environment to study and better understand the working of many complicated functions of biological motors in nature.

Inspired by both the natural biomolecular motors, as well as recent scientific efforts towards mimicking the functions of these biomolecular motors, the work described in this dissertation focuses on understanding the motion of active components. Active components are defined as components that either (a) autonomously move in the hydrodynamic assembly, or (b) start to move due to the application of a dynamic electric or magnetic field. The size of the particles is also important in determining the various forces and kinds of motion that can be achieved by them. Therefore, an important question that arises is determining the size of the molecular motor for achieving the optimal functioning conditions. It is known that for particles above 50 μm , deterministic Newtonian motion dominates, while for objects that are smaller than 1 μm in size, the inherent Brownian motion in the system randomizes the motion of the particles. Our active components are in the size range of 1 μm to 10 μm, a range where the boundary between the dominance of Brownian motion and Newtonian motion is not clearly defined. Therefore, it is the focus of this work to understand the motion of active components of the aforementioned size, and answer questions relating to the fundamentals of their functioning.

The active components studied here are of synthetic origin. Although they are nonmolecular, they perform overall linear or rotary motion on the microscale. Our experiments can, thus, provide an insight into the design and realization of molecular motors that can perform integrated motion on the macroscopic scale.

In all the experiments described in this dissertation, the active components are placed either into or close to an interface. Liquid interfaces posses their own hydrodynamic properties. The competition between the interfacial and bulk dissipative processes defines

a crossover length. This crossover length maybe larger or smaller than the size of the active components. A change in crossover length can interfere with the length scale of the chemo-mechanical energy conversion process and thereby unravel some of the ways these nano-motors function. Monolayers at liquid-liquid interfaces are very good model systems to mimic the presence of membranes along or across which the biomolecular motors move. Nano motors move at interfaces according to hydrodynamic rules that are significantly different from the rules for macroscopic motors [35].

Similar strategies are used when observing the motion of active components close to a solid/liquid interface. Here the solid/liquid interface is structured magnetically to create a magnetic heterogeneous environment that challenges the proper performance of the navigators. Solid-liquid interfaces are typical in all microfluidic lab-on-chip devices. To apply molecular motors for further development of microfluidic devices, one therefore needs to understand their functioning in such environments. Pertinent questions regarding the effect of interfaces on the speed, friction, and overall functionality of active components are addressed in this dissertation. One of the major concerns in the manufacturing of nano motors is dissipation. While the power of a motor often scales with it's volume, the dissipation scales with the surface area of the motor. Upon miniaturization, the ratio of dissipation versus the driving power increases when using the same power source. Systems are studied where dominance of dissipation is accepted to achieve directed and controlled motion of nanomotors. A primary motivation of this work has also been in attempting to achieve control over the transport of materials on the micron, submicron and nanoscale range. Properly functioning active components or nano machines require reliable navigational data to perform tasks assigned to them. Navigational data will tell the nano shuttles where they are, or where they should go, and will prevent these nano machines from getting lost. Most non-biological synthetic motors moving through fluids presently depend on external fields generated by macroscopic sources to achieve control. These fields may be magnetic electric, thermal, or concentration fields [36]. In fact, external fields have been used even in directing the motion of biomolecular motors at interfaces. Scientists van den Heuvel and colleagues [21] have used an electric field to steer the microtubules into one of two arms of a Y junction. Developing on this idea, our work has also focused on using magnetic field gradients to achieve control over their motion. Most of the current magnetic manipulation techniques depend on fields that vary on the cm-scale. However, developing magnetic techniques that

use the full potential of possible manipulations, requires relying on magnetic fields that vary on the length scale of the particles. In our experiments the active components are manipulated by using magnetic field gradients on the micron scale. This heterogeneity aids in designing more practical ways of controlling the motion of synthetic nanomotors.

In nature, the motion of biological motors occurs in heterogeneous environments. Part of the intra-cellular transport relies on autonomous motion of nano shuttles in a chemically heterogeneous environment. For example, cholesterol is synthesized in the Golgi apparatus, but accumulates in the plasma membrane of the cell. Vesicles transport the cholesterol from its origin (the Golgi apparatus) to its destination (the plasma membrane) [37]. The vesicles need to navigate in a heterogeneous system that is subject to strong thermal fluctuations. This dissertation therefore addresses questions such as how do the thermal fluctuations influence the navigation of the nano-motors, and how does one adapt the navigation when there is a network of targets instead of just one direction? Possibilities to guide the nano shuttles through a heterogeneous environment by applying homogeneous time-dependent external fields are explored. Thermal fluctuations are also exploited to achieve control over the motion of the active components. Answers to such questions provide an insight into the principles involving transport mechanisms in biological cells.

Miniaturization of assays also introduces a new area of fluid dynamics that needs to be explored and understood. In nature all essential biological functions, such as cell locomotion and intercompartmental transport, are accompanied by small-scale hydrodynamic flow. The flow is generated by the active components, which consume and convert energy. Microscopic active components differ quite significantly from their macroscopic analogues in the following ways:

1. the microscopic active components operate in an environment confined by interfaces, and

2. they move in a fluctuating heterogeneous environment, and their mean motion is an average of states in which the active components are locally trapped or free to move.

As a consequence active components on the micron or sub-micron scale move according to hydrodynamic rules that are significantly different from the rules for macroscopic motors. Most artificially tailored lab-on-chip devices depend on low Reynolds number fluid flow at solid/liquid and liquid/air interfaces. The low Reynolds number in case of the motion of

smaller particles through fluids arises because the viscous forces arising from the shearing motions of the fluid predominate over the inertial forces associated with the acceleration or deceleration of fluid particles. The behavior of these particles is governed by the so-called *creeping motion*, or the Stokes equations. Since the active components in the work described in this dissertation are incorporated at the solid/liquid, liquid/liquid and liquid/air interfaces, this study has also been successful in understanding the interfacial flow properties and the resulting flow patterns of surfaces that contain active components. This fundamental understanding is essential for the optimum design of motors working at the interfaces, and for developing optimal lab-on-a-chip designs.

The rest of this dissertation is divided into 5 chapters, each of which aims at understanding or achieving one of the goals outlined in the above frame. One of the active components studied extensively in this work is a bimetallic nanorod of platinum and gold, which moves autonomously in a hydrogen peroxide solution by using a catalytic reaction involving the breaking down of hydrogen peroxide to oxygen and water. The other active components that were incorporated into interfaces in this work are biological cells, bacteria and fluorescent beads. Our model interfaces are the air/water, the water/decane, and the magnetic garnet film/water interfaces. For a complete and thorough study we begin with trying to answer some fundamental questions about the bimetallic nanorods, like the questions relating to

1. the factors that decide the direction of motion of the active component

2. the correlation between the velocity of the active components and the rheological properties of the surrounding interfaces, and

3. the use of active components to measure rheological properties of biologically relevant interfaces.

Next, different strategies of guided navigation of both natural and synthetic active components in heterogeneous magnetic fields are investigated. In the fourth chapter we focus on using dissipation in the system to our advantage to guide the orientation of transversely magnetized nanorods incorporated in a solid/liquid interface in the presence of a precessing magnetic field. The fifth chapter focuses on the use of non equilibrium fluctuations to induce directed guided motion in magnetically labeled active components like paramagnetic colloids

and mouse macrophages. The sixth chapter uses the Brownian motion of charged differently sized colliodal beads to obtain an insight into their geometrical arrangement in the interface.

The results discussed in this dissertation contribute towards the understanding of both basic and applied research. The results also provide more insight into the fundamentals of the functioning of active components at the interface. The experimental results of the microspheres at the liquid/air interface tries to solve the long-standing argument amongst scientists regarding the effects of electrostatic forces on microspheres at interfaces, and the size effects that control their influences. Moreover, these studies also provide new applications for lab-on-chip devices. Achieving guided motion of autonomously moving nanorods will be useful in drug delivery or transport of materials along a fixed path which prevents the navigators from getting lost. Our approach to guide the orientation of the transversely magnetized nanorods may be used as efficient dynamic switches when incorporated into microfluidic devices. The transversely magnetized rods could be externally controlled to be used as microgates for microchannels, or as microstirrers just by altering the frequency of the externally applied magnetic field. The induced motion of mouse macrophages opens up a whole new area of diagnostic methods in lab-on-chip applications. This method may be especially useful when we wish to separate and transport a particular cell type from a collection of cells. For this separation, the cell of interest could be labeled magnetically by specific antibodies, and could then be separated from a mixture and moved to another region of interest. Moreover, it can also be used for single cell assay studies on a lab-on-a-chip, as well as for studies where we want to be able to track the cells while moving them around. Drug delivery using ferrofluids is becoming a common technique, and our method may be able to aid in studies relating to the efficiency of this technique. Although our active components are not of the size of the molecular motors, they are successful in mimicking the functions of the biomolecular motors. What remains to be done is the application of some of the lessons learned from this work while designing and downsizing the nanomotors to build more robust synthetic molecular machines with wider functional abilities than currently available in the technological nanoworld.

CHAPTER 2

Autonomously Moving Nanorods at a Viscous Interface

Since this dissertation involves the study of the motion of active components at interfaces we begin by studying the directed motion of one of the most extensively studied active component in this dissertation, namely the catalytic nanorod. In this chapter we study the autonomous motion of these catalytic nano-rods in Gibbs monolayer. The rods move at the interface due to the catalytic activity of the rods on the hydrogen peroxide aqueous subphase performing a Levy-walk super diffusive motion which can be decomposed into thermal orientation fluctuations and an active motion of the rods with a constant velocity along their long axis. A detailed analysis of this motion reveals a crossover from ballistic motion to normal diffusive motion while increasing the surfactant concentration which is explained by a loss of friction asymmetry of the rod. Miniaturization of the autonomous nano-rods also allows for precise measurements of surface shear viscosities as low as a few nNs/m.

2.1 Background and Introduction

Active Components are defined as components that either (a) autonomously move in the hydrodynamic assembly or (b) start to move due to the application of a dynamic electric or magnetic field. Their size varies from single proteins [38], over nanometers [39, 40], to the millimeter scale [41, 42]. Active components give rise to emergent phenomena such as dynamic self assembly [41–43], anomalous fluctuations [38, 44] and diffusion [45–47]. The experimental study of soft condensed matter systems targets behavior of systems under non-equilibrium conditions. Realistic models for the dynamic behavior of the biological cell and for hydrodynamics of lab-on-a-chip devices [47] have to account for these nonequilibrium properties. Active components present in dynamic complex fluids play an important role in maintaining stationary non-equilibrium conditions. A complete study of the behavior of these active components can lead to an understanding of the dynamic complex fluids in which they move. The first step in understanding dynamic complex fluids is the design of the active components. Active nano sized components involve flow that is dominated by the hydrodynamic boundary conditions at the interfaces. Understanding the energetics, interfacial hydrodynamics [48] and interactions of active nano components will thus also lead to efficient design of hydrodynamic nano devices and motors. The work described in this chapter is therefore motivated by a desire to understand the properties of active components at interfaces.

2.1.1 Autonomously moving nanorods

Active components most extensively studied in this dissertation are autonomously moving nanorods. These are bimetalic rods of platinum and gold of length 1 μm for each segment while the diameter of the rods is 300 nm (hence the name "nanorods"). These rods, synthesized by two groups at Penn State, were found to move autonomously when placed in a bulk solution of hydrogen peroxide [39, 49]. This was believed to be a result of a catalytical reaction between the hydrogen peroxide and the platinum which acts as a catalyst in the breakdown of the hydrogen peroxide to water and oxygen. Infact nanosized bubbles of oxygen were also seen on the rods. However, contrary to expectations, it was noticed that unlike the micron sized rods of Whitesides group [41], these rods moved with the platinum end forward. An analysis of the concentration of hydrogen peroxide revealed that the optimum

concentration was 3% at which speeds upto 20 μm/s were reached. It was also observed that to obtain the fastest moving rods, the length ratio of platinum to gold segments was 1:1.

In this chapter we address questions relating to the autonomous motion of nanorods. The motion of the nanorods at a viscous interface is studied to answer questions relating to a) what decides the direction of motion of the active component, (b) what is the correlation between the velocity of the active components and the rheological properties of the surrounding interfaces, (c) how to use active components to measure rheological properties of biologically relevant interfaces?

Nano motors move at interfaces according to hydrodynamic rules that are significantly different from the rules for macroscopic motors at interfaces. Further, Saffman and Delbrück [35] showed that the mobility of the motors at the interface is dominated by its size with respect to the Boussinesq length scale, l_B which is characteristic of a coupled membrane/bulk phase system and is defined as a ratio of the 2-dimensional surface viscosity η_s and the 3-dimensional bulk viscosity η. Heterogeneities in the interface on length scales below l_B lead to hydrodynamic behavior that is a complex mixture of 2d and 3d hydrodynamic interactions.

Gibbs-monolayers are assemblies of soluble surfactants at the liquid/liquid interface that can alter the hydrodynamic behavior of the interfaces. The rheological properties of the liquid/liquid interface can be widely tuned via the surface density of surfactants that is easily controlled by the bulk concentration that is in thermodynamic equilibrium with the surface. In a very dense monolayer with proteins incorporated into the interface, the typical surface shear viscosity can be of the order of 10^{-5} Ns/m and higher, while in a liquid phase it is at least six orders of magnitude lower. If the viscosity is high, one usually encounters viscoelastic behavior of the interface [50–55], while for small viscosities the surface can be considered to be only viscous [56–63].

The autonomously moving nanorods [39] are placed on a liquid/liquid interface and the rheological properties of the interface are varied by placing various concentrations of a soluble surfactant (forming a Gibbs monolayer) at the interface. The rods move at the interface due to the catalytic activity of the rods on the hydrogen peroxide aqueous subphase. They perform a Levy walk super diffusive motion that crosses over to normal diffusion for Boussinesq number $\mathcal{B} > 1$. This is explained as a loss of friction asymmetry of the rods. The motion of the rods at this interface also aids in the precise measurement of the rheological properties of the liquid/liquid interface.

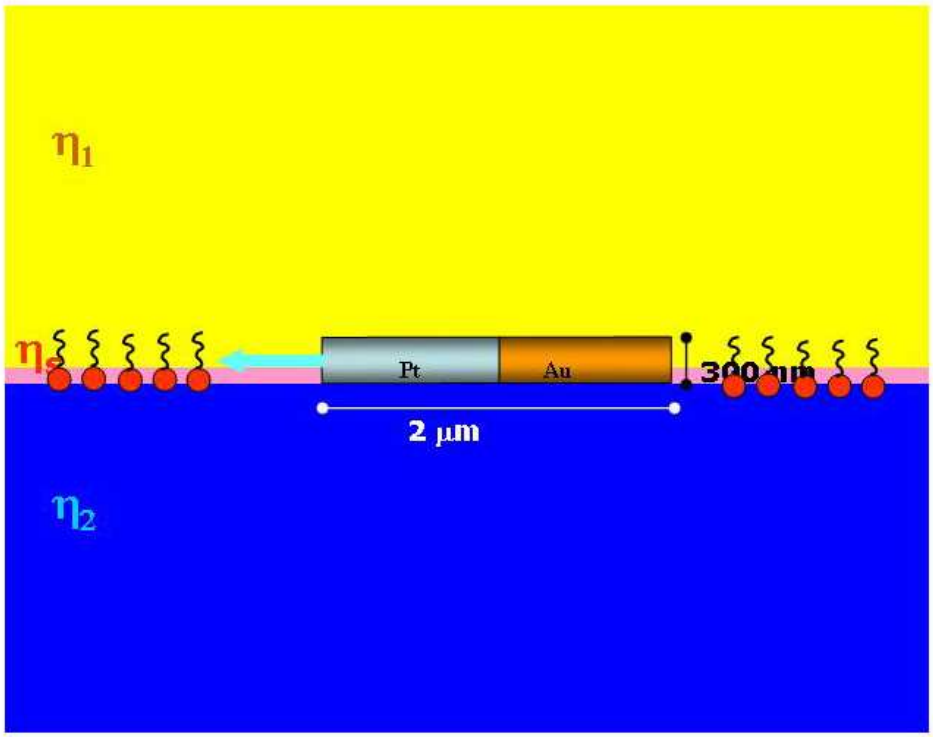

Figure 2.1: Schematic of the experimental setup. The bulk viscosity of the subphase (aqueous solution of H_2O_2) is η_2 while that of superphase (decane) is η_1. The surface viscosity of the interface is η_s where the interface is infinitely thin and for all mathematical calculations the rod is considered infinitely thin as well. The rheological properties of the interface is altered by the presence of a soluble surfactant forming a Gibbs monolayer at the interface.

2.2 Experimental Setup

Platinum/gold nanorods are synthesized as described in the chapter Materials and Methods, 7.1. Rods dispersed in water are dialyzed and resuspended in methanol. These are then carefully spread on an aqueous solution of 4 % hydrogen peroxide and then decane is added on top to form an oil/water interface. The rheological properties of the interface between the aqueous hydrogen peroxide and decane is varied by dissolving different concentrations of sodium dodecyl sulphate (SDS) in the aqueous solution at concentrations 0-1 mM such that it forms a Gibbs monolayer at the interface. The critical micelle concentration of SDS is 0.8

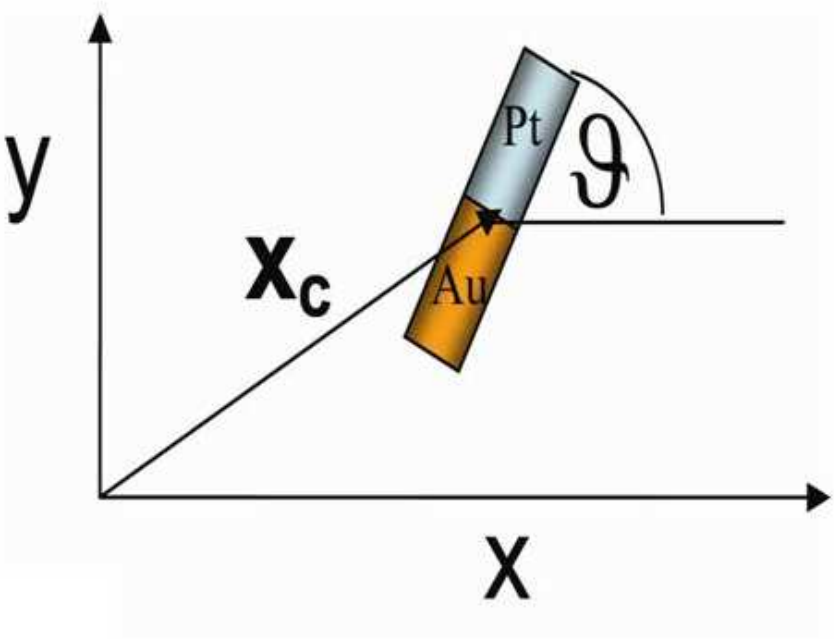

Figure 2.2: Schematics defining the center of mass X_c and orientation ϑ of the rod

mM. Each individual rod is visualized using a microscope (DLMP, Leica) in the transmission mode using a 100x oil immersion objective. The kinetics of the rod is followed and recorded using a black and white camera. The schematics of the setup is outlined in Figure 2.1.

2.3 Results and Discussion

The kinetics of an individual rod is followed for an analysis of the results. Each rod is described by its position of the center of mass $\mathbf{X_c}(t)$ and orientation $\vartheta(t)$ where the angle ϑ is defined as the angle between the long axis of the rod and an arbitrary chosen laboratory defined axis as shown in Figure 2.2. The raw data $\mathbf{X_c}$(t) and ϑ(t) are extracted for individual rods for each instant of time using the digitized images of the rod motion. Figure 2.3 shows a typical trajectory of the center of mass as well as the angular fluctuations of the rod on the bare decane-water interface as a function of time. The trajectory of the rod is a more open structure than a typical Brownian motion trajectory indicating that the motion is due

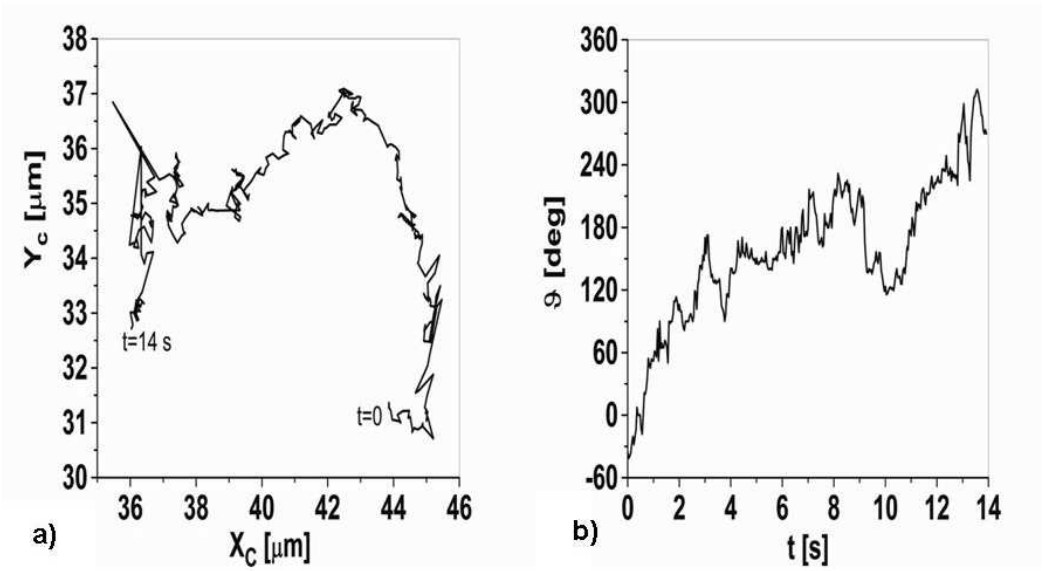

Figure 2.3: a) Levy-walk type trajectory of a rod on a bare (no SDS) H_2O_2(aqu) /decane interface, b) orientation fluctuations of the same rod on a bare H_2O_2(aqu) /decane interface

to the active motion of the rods. It is a fractal structure like those found in a Levy-walk superdiffusive processes [64]. A Levy walk is a random walk with frequent long periods where the particles move in one direction with a defined velocity.

All diffusive processes may be characterized by a correlation function

$$C(\tau) = \langle (X_c(t) - X_c(t+\tau))^2 \rangle \tag{2.1}$$

Often this correlation function shows a power law behavior according to

$$C(\tau) = \langle (X_c(t) - X_c(t+\tau))^2 \rangle \propto \tau^{\alpha} \tag{2.2}$$

where $\alpha = 1$ corresponds to *normal diffusion*, $\alpha = 2$ corresponds to *ballistic motion* and $1 < \alpha < 2$ to a *superdiffusion* motion.

Figure 2.4(a) shows a double logarithmic plot of the correlation function $C(\tau)$ of the position of the center of mass of the rod as a function of lag time τ accumulated over a period of time as indicated in the plot. We find that at low SDS concentration the rods move away from their initial position following a power law, $C(\tau) = 4Dt^{\alpha}$ where $\alpha = 1.6 \pm 0.1$ which is typical for a Levy-walk type of diffusion. The superdiffusive constant D is the largest for bare

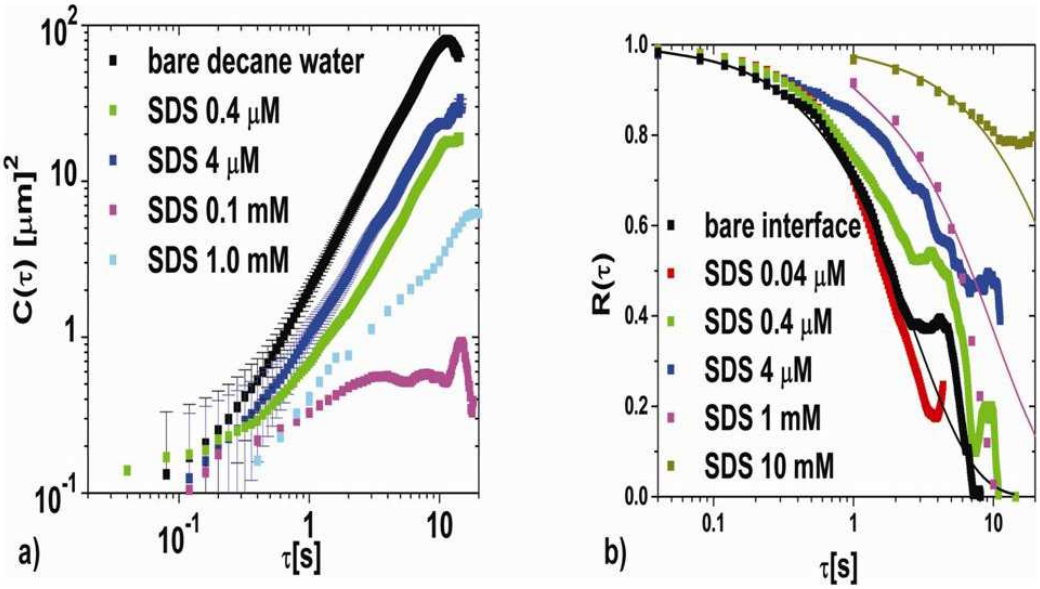

Figure 2.4: a) Plot of the correlation function C(τ) versus time τ accumulated over a period T $\approx$ 10 γ^{-1} (T=14s for the bare air water surface, T=140 s for the 10mM SDS solution) by following a single rod. The errorbars (0.2 μm^2) reflect the accuracy (400 nm) in the determination of X_c. b) Plot of the angular correlation function R(τ) of the rods on a H_2O_2(aqu) /decane interface for various subphase concentrations of SDS. The lines are fits according to $R(\tau) = e^{-\gamma\tau}$. The experimental curves deviate from the theory at large τ due to lack of statistics because of a finite accumulation time T. The relative statistical error from the finite accumulation time T is of the order $\sqrt{\tau/T}$ and not depicted in the figure.

decane water interface and decreases as the concentration of SDS at the interface increases. In fact it is observed that the exponent also decreases with increasing SDS concentration and it crosses over to $\alpha = 1 \pm 0.1$(typical for normal diffusion) for very high SDS concentrations. Thus with increase of the SDS concentration there is a cross over from Levy walk kind of motion to normal diffusive motion.

To better understand the kinetics of motion of the rod we also plot the rotational correlation function as shown in figure 2.4(b)

$$R(\tau) = \langle \cos(\vartheta(t) - \vartheta(t+\tau)) \rangle \tag{2.3}$$

As is seem in the figure 2.4(b), the angular correlation decays exponentially $R(\tau) = e^{-\gamma\tau}$ with increasing SDS concentration. In fact the rotational diffusion constant, γ obtained

from this analysis decreases with increasing SDS concentrations. It was also seen that the rotational data is independent of the presence of hydrogen peroxide indicating that the origin of the orientation fluctuations is purely thermal in nature.

The origin of the rotational motion is important to the understanding of the overall motion of the rod. Our measurements indicate that the origin of the rotational motion is thermal and so we may use the fluctuation dissipation theorem to calculate the frictional force acting on the rod. The torque T on a solid rod of length l and diameter d rotating with angular frequency ω in a bulk fluid of viscosity η was calculated first by Burgers [65]

$$T = \frac{\pi/3}{\ln(2l/d) - 0.8} \cdot \eta l^3 \omega \tag{2.4}$$

Now, since our rod is at the interface, we assume that only half of this torque acts on the subphase while the other half acts on the superphase. At the interface we would also have contributions to the torque from the Marangoni forces and the surface forces. The total torque is therefore approximated to be the sum of the surface and bulk contributions.

$$T = (f_s + f_b)(\eta_1 + \eta_2) l^3 \omega \tag{2.5}$$

where f_b is half of the bulk contribution to the torque according to Burgers, f_s is the surface contribution (calculated as a function of the Boussinesq number $\mathcal{B}$), η_1 and η_2 are the bulk viscosities of the two phases. The Boussinesq number $\mathcal{B}$ is defined as :

$$\mathcal{B} = \frac{\eta_s}{(\eta_1 + \eta_2) l} \tag{2.6}$$

The surface contribution f_s to the torque calculated in the limit of a vanishing rod (appendix A.2) is plotted as a function of $\mathcal{B}$ as shown in figure 2.5.

In the figure, the asymptotic value for $\mathcal{B} \to 0$ indicates the contributions from the Marangoni forces while the contributions from the surface viscosity are accounted for in the values for $\mathcal{B} \to \infty$. From the Stokes- Einstein relation

$$f_s(\mathcal{B}) = \frac{k_B T}{(\eta_1 + \eta_2)\gamma l^3} - f_b \tag{2.7}$$

Using our rotational motion data we can obtain γ for the various SDS concentrations and translate it to the corresponding value for the Boussinesq number. The surface viscosity of the interface can then be obtained by using 2.7

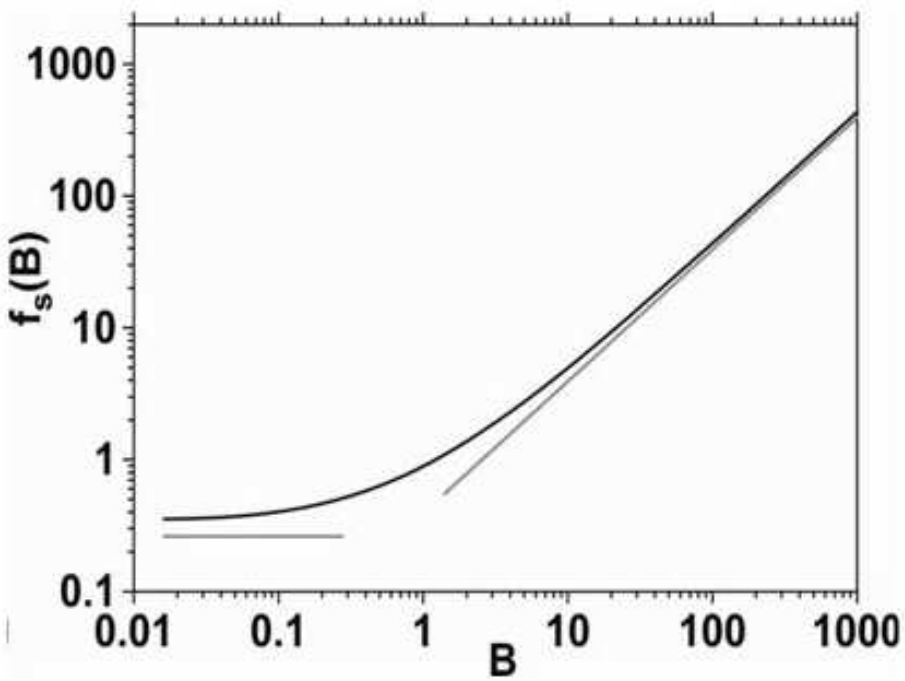

Figure 2.5: Surface torque coefficient $f_s(\mathcal{B})$ as a function of the Boussinesq number. The gray lines are the asymptotic relations given in A.2

Figure 2.6 shows a plot of the surface viscosity as a function of the SDS concentration. This data agrees with data from Bouchama and di Meglio [66] and of Khattari et al. [1] thus implying that the origin of the orientation fluctuations is indeed thermal. In case of long rotating rods the chemophoretic flow may introduce an apparent slip velocity along the boundary of the rod. Thus the chemophoretic motion couples to the translation motion only along the long axis of the rod.

It can then be concluded that the Levy walk motion of the rod is a superposition of translational motion of the rod along its long axis with the thermal orientational fluctuations. To better understand this motion we therefore need to decouple the motion of the rod into its parallel and perpendicular displacements. The resultant velocity of the rod is given by the time derivative of the center of mass $\mathbf{v} = \dot{\mathbf{X}}_\mathbf{c}$ We define a $\mathbf{c}$ director, $\mathbf{c} = (\cos\vartheta, \sin\vartheta)$, which

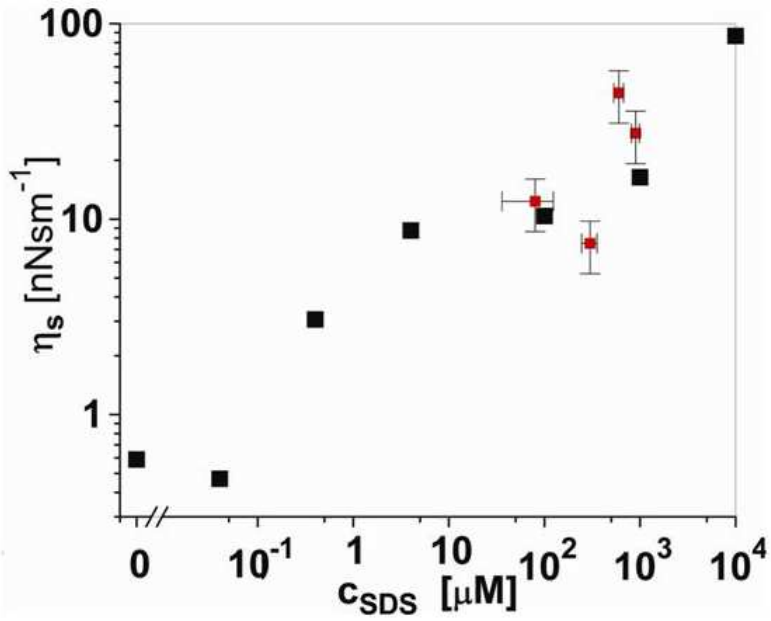

Figure 2.6: Surface shear viscosity of the decane/water interface (black) as determined from the angular correlation function R(τ) of the rod orientation. The red data is the surface shear viscosity of SDS in a stearic acid monolayer at the air/water interface as measured by Khattari et al. [1]

decouples the displacement of the rod along its parallel and perpendicular components. The distance the rod moves along its long axis is then given by $s_{\parallel}(t) = \int_0^t \mathbf{c}(\mathbf{t}') \cdot \mathbf{v}(\mathbf{t}')\, dt$ while the distance the rod moves perpendicular to the platinum end of the rod is given by $s_{\perp}(t) = \mathbf{e_z} \cdot \int_0^t \mathbf{c}(\mathbf{t}') \times \mathbf{v}(\mathbf{t}')\, dt$ where $\mathbf{e_z}$ is the unit vector perpendicular to the interface. The correlation functions of the motion of the rod parallel to the long axis is then given by

$$C_{\parallel}(\tau) = \langle (s_{\parallel}(t) - s_{\parallel}(t+\tau))^2 \rangle$$

while the correlation functions of the motion of the rod perpendicular to this direction is given by

$$C_{\perp}(\tau) = \langle ((s_{\perp}(t) - s_{\perp}(t+\tau))^2) \rangle$$

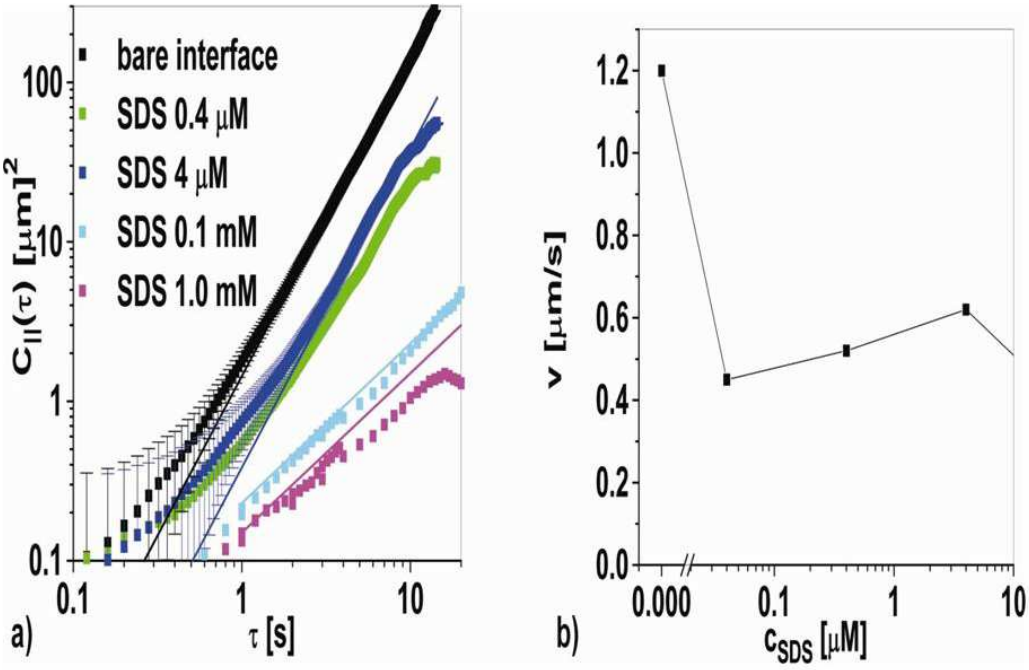

Figure 2.7: a) Correlation function of the rod motion parallel to its long axis for various SDS subphase concentrations calculated from the same raw data as in fig. 2. The correlation functions follow the law $C_{\|}(\tau) = v^2\tau^2$(black and blue lines) at low SDS concentration and a diffusive behavior $C_{\|}(\tau) = 2D_{\|}\tau$ (cyan and magenta line) at high SDS concentration. The velocity v is shown as a function of the SDS concentration in b) for $c_{SDS} < 10\mu M$.

Figure 2.7 shows the parallel correlation function of the motion of the rod. The perpendicular motion is not shown since we found there is negligible motion in this direction as expected from previous observations of the rod motion [39]. From figure 2.7 we again find that the parallel correlation function $C_{\|}$ obeys a power law for both low and high SDS concentration. However this time the exponent $\alpha_{\|} = 2.0 \pm 0.1$ for low SDS concentrations such that $C_{\|}(\tau) = v^2\tau^2$ and we can obtain the ballistic velocity of the rods. The velocity is found to decrease as we increase the SDS concentration (shown in figure 2.7 right). Moreover as the concentration of SDS is increased the exponent changes such that at $c_{sds} > 0.1mM$ the exponent $\alpha_{\|} = 1 \pm 0.1$, which is typical of normal edge on diffusion, i.e. $C_{\|}(\tau) = 2D_{\|}\tau$, with $D_{\|}$ the diffusion coefficient for rods diffusing along their long axis. Thus we find a crossover from ballistic motion to normal diffusion motion as we change the SDS concentration. In

fact it is found that this crossover occurs at Boussinesq numbers $\mathcal{B} \approx 1$. These observations direct us to better understand the translational and rotational motion of the rod.

Although it is known that the rods move in an aqueous solution of hydrogen peroxide with the Pt end forward the exact mechanism of motion in the Pt direction has not been explained satisfactorily prior to this work. Our hypothesis from the analysis of the raw data of the rod motion is that the direction is dictated by a hydrodynamic friction asymmetry and the rod will move in the direction of minimum friction. If a rod moves with the platinum end forward then the oxygen released at the platinum end gets advected to the gold end and helps lubricate the surface of the rod. This significantly lowers the viscous drag on the rod since the viscosity of oxygen is three orders of magnitude lower than the viscosity of water. On the other hand if the rod were to move with the gold end forward then the oxygen released at the platinum end does not get advected to the gold end and hence there is not much lubrication of the rod. Thus moving with the platinum end forward introduces a reduction in the viscous friction as opposed to the other direction. Considering the chemistry of the reaction, whatever is the mechanism of motion, the chemical reaction leads to a symmetric arrangement of both products and reactants around the platinum section. These symmetric fluctuations would cause a motion in an arbitrary direction. However the presence of the asymmetric friction causes a mean rod motion in the direction of the platinum end since this is the direction of minimal friction. This hypothesis is analogous to a thermal ratchet where the thermal noise is replaced by chemical noise and the asymmetric potential is replaced by asymmetric friction.

The crossover from ballistic to diffusive motion occurring at Boussinesq number $B \approx 1$ supports this hypothesis. The flow profile of a rod as calculated by Fischer [63] identifies a region closer than the Boussinesq length, $l_B = \mathcal{B}l$, and another farther away than l_B from the rod. In the regions closer to the rod than l_B, the velocity varies approximately logarithmic with the distance from the rod, while further away it varies inversely with the velocity. Thus neglecting the weak logrithmic decay, the surface viscosity increases the effective hydrodynamic radius of the rod. In other words, the rod moves in the viscous interface as if a rigid object of radius greater than that of the rod, by a length l_B, would move in a non viscous interface. The size l_B effectively renders the asymmetric rod hydrodynamically more symmetric. The oxygen produced at the platinum end will now be able to lubricate the rigid region of size l_B surrounding the rod irrespective of the direction the rod decides to

move. If l_B becomes larger than the gold section of the rod the friction becomes symmetric in both directions and as a result there is no longer a preferential direction for the rod to move. Although the surface viscosity quenches both the thermal diffusive and the H_2O_2 propelled motion, the quenching of the propelled motion is more pronounced since the friction is now symmetric. This change from active motion to diffusion is observed as a crossover in the exponent $\alpha_{\parallel}$ from 2 to 1 at $\mathcal{B} \approx 1$.

The rotational and translation motion imply that the motion of the rod is a Levy-walk superdiffusive motion which is a superposition of the orientational fluctuations of thermal origin and an active ballistic motion of the rods with a constant velocity along their long axis.

2.4 Summary and Conclusion

The detailed analysis of the translational and rotational motion of the rods indicate that their motion consists of a superposition of translation motion along the long axis of the rod and orientation fluctuations of thermal origin. The thermal orientational fluctuations slow down by the addition of a soluble surfactant. These orientational fluctuations can therefore be used to measure the surface viscosity of the Gibbs monolayer forming at the interface as a function of the subphase concentration. The translation motion of the rod is such that if the length of the rod is larger than the Boussinesq length (low SDS concentration) then the rod is propelled forward along its long axis towards the platinum end. However if the Boussinesq length becomes greater than the rod length then the translational motion of the rod reduces to normal diffusion motion along the rod. The results of our analysis support the hypothesis that the rods move due to an asymmetric friction which creates an effect similar to a thermal ratchet motion. The catalytic reaction of the hydrogen peroxide produces fluctuating forces in the system which would lead to motion in an arbitrary direction. However, the oxygen helps in the lubrication of the whole rod including the gold segment if the rod moves with the platinum end forward. This in turn leads to an asymmetry in the hydrodynamic friction. Thus the friction asymmetry causes a directed motion along the direction of minimum friction. Adding a surfactant has the net effect of increasing the length of the rod by a rigid segment, l_B, of the size of the Boussinesq length, on both ends of the rod, which tries to restore the symmetry. If the length of the rod becomes smaller than the Boussinesq length, then the symmetry in the hydrodynamic friction is restored. The crossover of the active motion to a diffusive motion is a consequence of this restoration of the symmetry in the friction. The superposition of the orientational fluctuation along with translation motion along the long axis gives rise to a Levy walk motion of the rods. For the most effective motion we require equal proportions of the platinum and gold segments. It is also believed that miniaturization of these rods would create more effective performance of the rod motion. The understanding of the motion of the rods at an interface is important for better design of nanomotors. The insight into the hydrodynamic rules of motion for these rods will help promoting their use in microfluidic devices. These nanomotors are active components which can be controlled externally to achieve directed motion. Later in this dissertation we will also talk about the guidance of these nanorods in microfluidic devices.

Designing ways to control the motion of these rods will provide navigational data to the rods which in turn would serve the purposes of delivery of materials from one place to another along a fixed direction.

CHAPTER 3

Guided Motion of Autonomous Navigators

In Chapter 2 we explained a possible mechanism of motion of the autonomously moving bimetallic nanorods. In this chapter different strategies of guided navigation in heterogeneous magnetic fields are investigated using natural and synthetic autonomously moving micro- and nano-navigators placed on top of a magnetic garnet film with uniaxial anisotropy creating a dense stripe domain structure. Initially, the motion of magnetotactic bacteria on the magnetic garnet film is investigated. The results from these investigations are then used to study the nanorods of Chapter 2. These rods are rendered either para or ferromagnetic by the addition of suitable magnetic sections to the nanorods. By following different strategies for the design, different modes of motion i.e. roving motion and guided motion, are achieved for these differently magnetized ferromagnetic and paramagnetic nano- navigators. These different modes of motion can be utilized for distinct processes, such as the delivery and distribution of molecular cargo attached to synthetic navigators.

3.1 Background and Introduction

Properly functioning nano machines [39, 49, 67, 68] operate in the unexplored realm of nanoscience. The motion of micro- and nanoscale objects is being used in nature for cell trafficking and the delivery of metabolized products. In nanoscience one mimics strategies from nature and applies them to the nanoscale motion of roving sensors, drug delivery and effective transport systems. Depending on the application, one tries to either guide the motion along well-established paths or one uses a roving statistical motion for the fast spreading of components over a broad range. In either case, nano shuttles on the colloidal scale, depend on reliable navigational data in order to fulfill their tasks in a usually heterogeneous environment. Navigational data will tell the nano shuttles where they are, or where they should go and will prevent the nano machines from getting lost.

In this chapter we present a variety of autonomously moving natural and synthetic navigators in heterogeneous magnetic fields of their surroundings. The response of magnetotactic bacteria to the heterogeneous magnetic field is studied and the results utilized for the various strategies of design of synthetic para- and ferromagnetic [49,67] nanorods for guided motion. We show that the motion of ferromagnetic magnetotactic bacteria and the motion of catalytic para- and ferromagnetic nanorods can be understood by controlling the relative strengths of their magnetism, their propulsion, and their thermal fluctuating properties. There is a surprisingly complex interplay of these interactions when the nano shuttles are placed in a heterogeneous magnetic field on top of a magnetic garnet film. This allows us to continuously vary the motion from an enslaved guided motion, via a partially controlled anomalous diffusion, toward an autonomous statistical roving motion. While performing their autonomous motion the navigators report information on the local direction of the magnetic field via the orientational order of their long axis. Catalytic nanorod and bacterial propulsion compete with the magnetic forces acting in the magnetic heterogeneities. The nano navigator distribution in the heterogeneities is therefore dominated by the interplay of propulsion and orientation, and significantly differs from an equilibrium Boltzmann distribution. The navigators are also able to sample the magnetic field in regions that are energetically unfavorable by multiples of the thermal energy. Four different nano probes, magnetotactic bacteria (Magnetotacticum gryphiswaldense) and three types of catalytic magnetic nanorods, were released in an aqueous solution on top of a magnetic $Y_{2.5}$ $Bi_{0.5}$

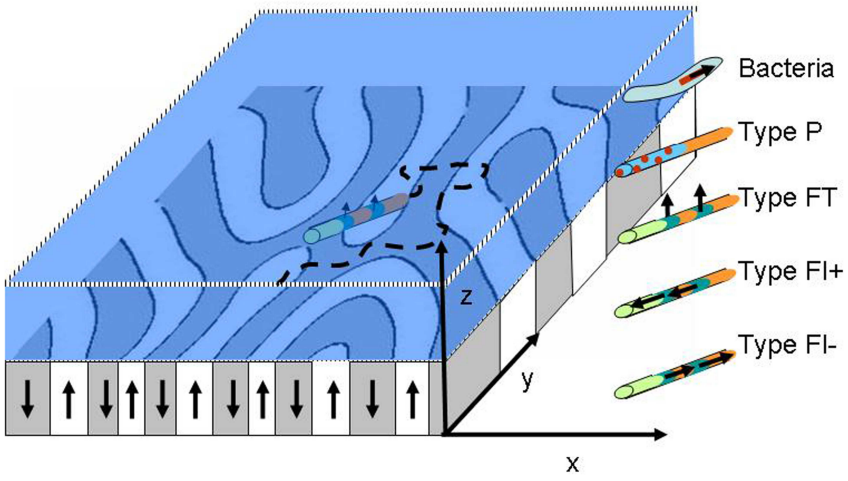

Figure 3.1: Scheme of a magnetic garnet film with upward (white) and downward (gray) magnetized domains forming a labyrinth pattern. Autonomously moving navigators, i.e. magnetotactic bacteria, paramagnetic or ferromagnetic rods of type P, FT, FL are placed in an aqueous solution above the garnet film

$Fe_{5-q}Ga_qO_{12}$ (q = 0.5-1) garnet film where they moved according to the constraints set by the inhomogeneous magnetic field of the stripe domain pattern in the uniaxial anisotropy garnet film.

3.1.1 Magnetic Garnet Films

The magnetic garnet film is a 4 μm thick film, as shown in Figure 3.1, of composition $Y_{2.5}$ $Bi_{0.5}$ $Fe_{5-q}Ga_qO_{12}$ (q = 0.5-1) [69]. The film has a normal spontaneous magnetization (M_s=11 kA/m), with domains forming stripes alternating between up and down magnetization as shown in figure 3.2. A typical wavelength of the structure is around λ =2 π/k $\approx$ 10 μm, i.e. larger than the length of the nanorods and on the order of the length of the bacteria. The stripes run in irregular directions with a persistence length of approximately 100 μm. The stripe pattern can take on a variety of shapes and sizes depending on the temperature, the composition q, or the presence of an external magnetic field H_{ex} perpendicular to the film.

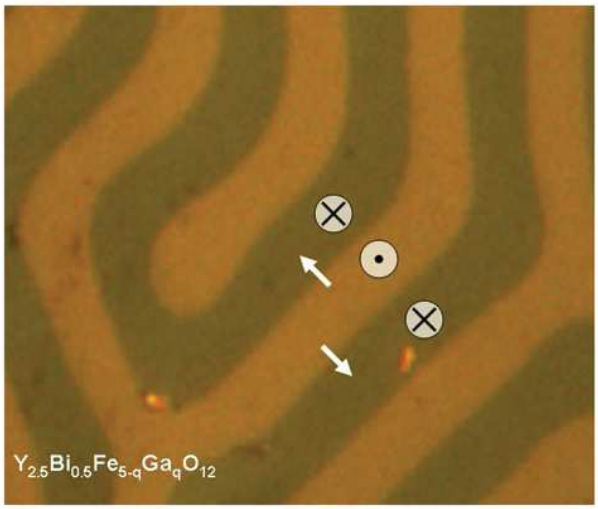

Figure 3.2: Polarization microscope image of the magnetic garnet film showing domains forming stripe patterns. The brighter region have magnetization pointing out of the plane while the darker regions have magnetization pointing into the plane.

Since the persistence length exceeds the size of the rod, and the domain wall width is much smaller than the rod length, we use the limit of infinite persistence length and negligible domain wall width in the mathematical treatment of the problem. The magnetic field above the film is then the solution to a two-dimensional Laplace Equation and we write it as the gradient of the magnetic potential where

$$\mathbf{H} = \nabla \Re \Psi \qquad \Psi = [2i/\pi(\text{dilog}(1 - e^{ik}))] \tag{3.1}$$

The domains can be visualized using the Faraday effect and depending on the direction of magnetization they appear as dark and bright domains as shown in Figure 3.2. The direction of the magnetic field above the walls is shown by the white arrows. Just above the magnetic film, the magnetic field always points from the bright to the dark region. Since the magnetic field strength varies logarithmically with the distance from the wall, the magnetic fields are

strongest at the domain wall such that magnetic particles are usually attracted to the wall.

3.1.2 Magnetotactic Bacteria

Some of the most exciting magnetic micro-navigators in nature are magnetotactic bacteria which are geomagnetically sensitive and navigate along the earths magnetic field. They were first discovered in 1970 by a graduate student Richard Blakemore [70] and have been studied extensively since then. *Magnetotacticum gryphiswaldense* (see Figure 3.3) are bacteria of length 6.5 μm and diameter 0.7 μm that use intracellular organelles called magnetosomes to navigate along the earths magnetic field. The magnetosomes are membrane-encapsulated vesicles containing ferromagnetic nanoparticles of magnetite, Fe_3O_4. Their typical size ranges from 35-120 nm long crystals. This size range is within the permanent single-magnetic-domain size range for magnetite. The crystals align in one or more long chains along the long axis of the bacteria [71] to maximize the magnetic moment. In this arrangement the total magnetic dipole of the cell is the sum of the magnetic moments of the individual magnetosome particles. The magnetic moment of the bacteria [72] is of the order of $m \approx 1.5 \times 10^{-15}$ Am^2. As a result the bacteria align along the geomagnetic field lines and behave like tiny self propelled magnetic compass needles. Bacteria from the northern hemisphere swim preferentially parallel to the magnetic field corrosponding to a northward migration in the geomagnetic field, i.e they are "north-seeking" bacteria. On the other hand, most of the bacteria growing in the southern hemisphere swim antiparallel to the magnetic field and are known as "south-seeking". Since the geomagnetic field is inclined downwards from the horizontal in the northern hemisphere and upwards in the southern hemisphere the preferential migration of the bacteria helps direct them towards growth favoring oxic - anoxic zones [71] in sediments at the bottom of natural waters.

3.1.3 Synthetic Nanorods

To obtain autonomously moving rods we use the same propulsion mechanism as in Chapter 2. However in order to be able to achieve confinement and guidance we now need to magnetically label them. Three different types of nanorods were synthesized by the Penn State group with different magnetic properties. Depending on the design they either mimic or differ from the

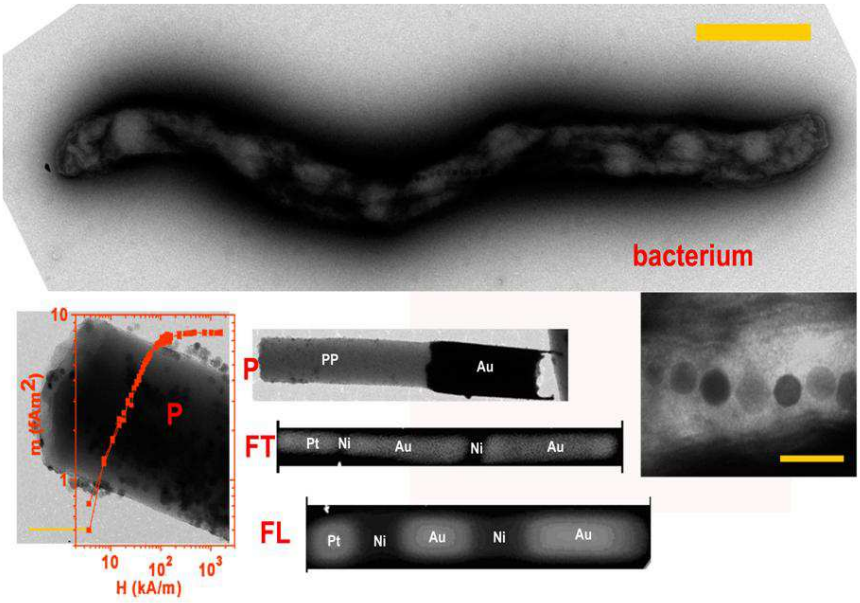

Figure 3.3: Electron micrographs (EM) of a magnetotactic bacterium (top) and of nanorods (bottom middle), type P, FT and FL, showing the different segments of each rod. Bottom left: EM image showing a magnification of the polymer section of a type P rod containing Fe_3O_4 nanoparticles. A SQUID measurement of the magnetic moment of a type P rod versus the magnetic field showing the paramagnetic behavior of the rod is overlayed in the image. Bottom right EM image showing a magnification of a magnetotactic bacterium highlighting a chain of vesicles (magnetosomes) that contain Fe_3O_4 nanoparticles. Scale bar (orange) corresponds to 100 nm for the high resolution images to the bottom left and the bottom right, to 1 μm for the full images of the nanonavigators.

magnetic properties of the magnetotactic bacteria.

Paramagnetic nanorods (type P nanorods, figure 3.3) of diameter $2r = 400$ nm and length $l = 2.3\mu$m are subdivided into two segments, one consisting of gold l_{Au}=0.9 μm followed by another consiting of polypyrrole l_{PP} =1.4 μm. The polypyrrole segment contains 5-20 nanometer diameter Fe_3O_4 particles (synthesized as in [73]). The individual particles are superparamagnetic but their dispersed arrangement in the polypyrrol renders the entire rod paramagnetic (figure 3.3). The rods have a saturation magnetic moment $m \approx 7.4 \times 10^{-15}$ Am^2 that is reached at an external magnetic field of the order of 100 kA/m. However at the fields of the garnet film, *i.e* 12 kA/m, these behave paramagnetic as indicated by the SQUID data(overlay figure 3.3). The saturation magnetisation is relatively higher than the permanent magnetic moment of the magnetotactic bacteria.

Ferromagnetic nanorods [49] consisting of Pt-Ni-Au-Ni-Au segments were synthesized by the Penn State group using electrochemical deposition of metals into alumina pores as described in the chapter 7.1. Depending on the size of the nickel segment with respect to the diameter the rods are either transversely or longitudinally magnetized (type FT and type FL). They are 2.6(FT)/2.5(FL) μm long and are subdivided into segments where l_{Pt}= 468/356 nm, $l_{Ni,1}$=64/311 nm, $l_{Au,1}$ = 957/533 nm , $l_{Ni,2}$ = 106/444 nm and $l_{Au,2}$=1.021/0.889 μm as shown in Figure 3.3 (bottom middle). The type FT rods have nickel segments with an oblate geometry ($l_{Ni} \ll r$) and hence they favor the alignment of the nickel magnetization perpendicular to the rod (transversal magnetization). The type FL rods have prolate Ni segments with a magnetization pointing along the long axis (longitudinal magnetization). In case of the type FT rods the size of the nickel segments are chosen ensuring that they have single ferromagnetic domains but are not superparamagnetic. The magnetization of the rods is estimated to be $M = 310$ A/m from the rod alignment in water in a magnetic field of $H = 1$ kA/m **??**. It was shown earlier [49] that once magnetized, the FT/FL rods align with their long axis perpendicular/ parallel to a magnetic field.

3.2 Experimental Setup

The rods were extracted as described in 7.1 while the bacteria were grown according to the protocol described in 7.5. A 7 % aqueous solution containing the rods dispersed in solution and bacteria resuspended in HEPES buffered solution [74] was placed on the magnetic garnet

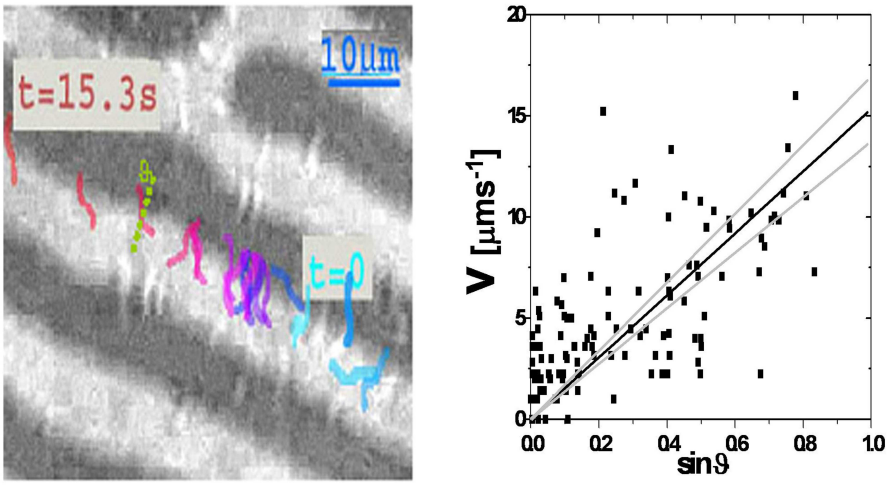

Figure 3.4: (Left) Polarization microscope image of magnetotacticum gryphilswaldense (bright) on a magnetic garnet film. Domains are visualized (crossed polarizer and analyzer) using the Faraday effect. A time sequence ($\Delta t = 0.9s$) of the tangential motion of one bacterium (colored) along a domain wall is shown. (Right) The velocity of the bacterium along the domain wall correlates with the projection of its director onto the stripe direction.

film (treated as described in chapter 7.4) as shown in Figure 3.1. An efficient interplay between the electrostatics and gravity is able to confine the nanonavigators to a plane located a few nanometers above the surface of the film. The navigators as well as the film surface is viewed under a polarization microscope LEICA DMP using a 63 x water immersion lens and images are taken using Basler13 color camera. Videos of the motion of the navigators are recorded using the Streampix software which allows us to digitize the videos. Adobe Photoshop was used for all image overlays.

3.3 Results and Discussions

3.3.1 Magnetotactic Bacteria on magnetic garnet films

It was found that most of the bacteria are trapped at the domain walls. Figure 3.4 (left) shows the time sequence of the position of one north seeking bacterium, marked in color,

overlaid on an image of the film. As seen in figure 3.4, the bacteria do move vigorously due to the motion of the flagella, however they are unable to escape from the magnetically strong domain walls. As a result they are confined to the wall and move transversely along the wall depending on their orientation with respect to the wall. Figure 3.4(right) proves that indeed the tangential velocity is roughly proportional to the projection of the bacterial long axis onto the domain wall.

Sometime one finds a bacterium that is able to escape the wall. Figure 3.5 shows examples of such an escape and the behavior of the bacterium under these circumstances.

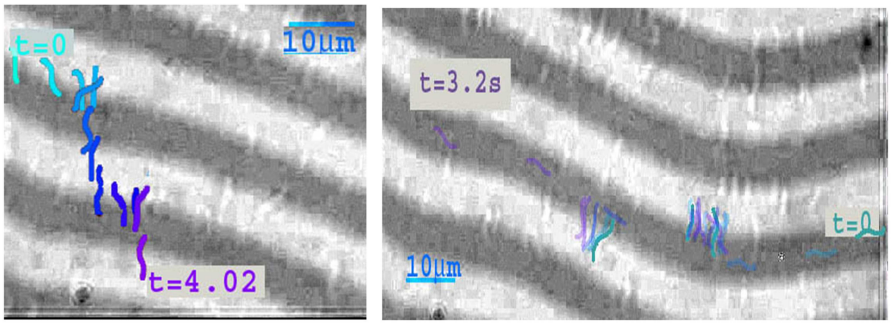

Figure 3.5: (Left) A time sequence ($\Delta t = 0.3$ s) of the tangential motion, escape, recapture and second escape from a domain wall of one bacterium (colored) is shown. (Right) Two bacteria are trapped at the domain wall, while one bacterium that has escaped to the dark domain avoids traveling antiparallel to the magnetic field by following the stripe direction.

Figure 3.5 (left) shows a bacteria trapped at one wall. This bacterium escapes and traverses to the next wall. Since the direction of the magnetic field above a domain wall alternates between parallel and anti-parallel, the magnetization at this wall is antiparallel to the magnetosomes and hence it is unfavorable for the bacteria. Therefore it easily goes through this wall and gets recaptured at the next wall where the magnetosomes are again parallel to the magnetization direction. However once it escapes this wall it gets captured at the next wall as well, which is an unfavorable wall. Although initially this surprised us, we found that Kalmijn et.al. [75] have shown that microsecond pulses of the order of 50 kA/m may be enough to remagnetize the bacteria. While moving across the domain wall,

the bacterium experiences a field pulse of lower magnitude but longer duration at the wall and thus might get remagnetized. Such a remagnetization of the bacteria probably occurred, which explains the trapping at the initially unfavorable wall.

On the other hand the bacteria after escaping from a wall may completely avoid the domain wall and move parallel to the stripe pattern at high speeds (27 μms^{-1}) since it is unable to penetrate the unfavorable wall. To align itself parallel to the field the bacterium has to point downwards into the film, but this direction is blocked by the garnet surface. Moving up or crossing the domain wall toward a bright domain would mean traveling anti-parallel to the magnetic field and here the bacterium avoids such motion by choosing the more favorable direction, which is perpendicular to the magnetic field (along the dark stripe). Thus while bacteria trapped at the domain walls undergo motion along the domain wall, a bacterium stuck in the dark domain travels along the stripe and perpendicular to the magnetic field.

Thus guidance along the stripe pattern is achieved only for the small fraction of dynamically frustrated bacteria that are strong enough to escape the field gradients of the domain wall.

3.4 Synthetic Nanonavigators

3.4.1 Strategies for the design to achieve guided motion

Learning from our experience with the natural navigators we devise several design strategies for achieving better guidance of our synthetic nanonavigators. In section 3.3.1 it was seen that the ferromagnetic orientation of the magnetotactic bacteria was in conflict with the desired propulsion direction along the stripe pattern. It was further noted that guidance was only achieved for the small fraction of bacteria by dynamic frustration. This conflict of orientation maybe resolved by the following strategies.

1. One could achieve synergy between the rod motion and magnetism by orienting the magnetic compass perpendicular to the long axis. As a result the long axis lies along the domain wall of the garnet film and the magnetic moment points parallel to the magnetic field of the domain wall. This strategy was followed by using type FT rods.

2. One may also simply reduce the longitudinal ferromagnetic moment of the rods relative

Figure 3.6: Polarization microscopy image of transversally magnetized type FT nanorods (bright) on a magnetic garnet film. The position of a nanorod is overlayed on the image of the garnet film. We also show the definition of the angle between the nanorod director **c** and the local **k**-vector of the stripe pattern

to that of the magnetotactic bacteria. This last strategy is implemented by using type FL rods.

3. One may resolve the conflict of orientation by using paramagnetic instead of ferromagnetic rods, which will always establish a magnetic moment in the direction of the magnetic field. This leaves the navigators more options to move in various directions. This strategy was implemented with type P rods.

In the following section we discuss the success of each of these strategies.

3.4.2 Transversally magnetized ferromagnetic rods

A time sequence of the position of a type FT rod is overlaid on the image of a garnet film in Figure 3.6.

Contrary to our expectations of being confined by the domain walls the rods follow a statistical fractal path that frequently crosses the stripes showing little correlation to the garnet structure. In order to extract the statistical correlation between the rod motion and the garnet structure further analysis was done on the digitized video. The probability density, *f*, of finding the rod at a certain distance s ($0 < s/\lambda < 1$) from a domain wall was measured. Low s values correspond to dark stripes, while high s values correspond to bright stripes. In addition, the time-averaged rod orientation $\langle \cos 2\theta \rangle$, at this location s is also extracted from the images where $-\pi/2 < \theta < \pi/2$ is the angle between the long axis of the rod and the local **k**-vector of the stripe pattern (Figure 3.6). These results are summarized in Figure 3.7. The **k**-vector is to point in the same direction as the normal component of the rod velocity. Since the magnetic forces are small compared to the rod's stalling force, the absolute value of the rod velocity is constant. The probability density fulfills the equation of continuity

$$\partial f/\partial t + \nabla \cdot (f\vec{v}) = 0 \tag{3.2}$$

Since the equilibrium distribution must be time independent, $\partial f/\partial t = 0$ and f can depend only on the position s, $\nabla \cdot (f\vec{v}) = 0$ or $fv_n = const.$ Now $v_n = v \cos\theta$ such that

$$f \propto \langle 1/\lambda |\cos\theta| \rangle \approx 2\lambda/(\sqrt{(1 + \langle \cos 2\theta \rangle)}) \tag{3.3}$$

Figure 3.7(a) shows the orientation $\langle \cos 2\theta \rangle$ vs s/λ in the absence of an external field. $\langle \cos 2\theta \rangle < 0$ indicates a parallel orientation with respect to the domain wall while $\langle \cos 2\theta \rangle > 0$ indicates a perpendicular orientation. $\langle \cos 2\theta \rangle \simeq 0$ implies no preferred orientation. In Figure 3.7(a) we find that as expected there is hardly any preferred orientation of the rods above the domain walls. This is because the equipotential plane is parallel to the garnet surface which allows the rod to orient equally well in either the x- or y- direction of the equipotential surface. However at the domain walls the rods orient parallel to the wall since the equipotential surface is normal to the domain wall. Figure 3.7(b) shows the probability density *f* vs s/λ. There is good agreement between the observed value of *f* and that calculated from equation 3.3 (red and green crosshatched data) indicating that the probability density, *f*, is indeed a result of the orientation of the rod and its forward motion. Figure 3.7(c) and (d) shows the orientation $\langle \cos 2\theta \rangle$ and the probability vs s/λ in the presence of an external field. Since the field strength above the domain walls decreases in the presence of an external field the orientation of the rods parallel to the domain walls is no longer enforced. However,

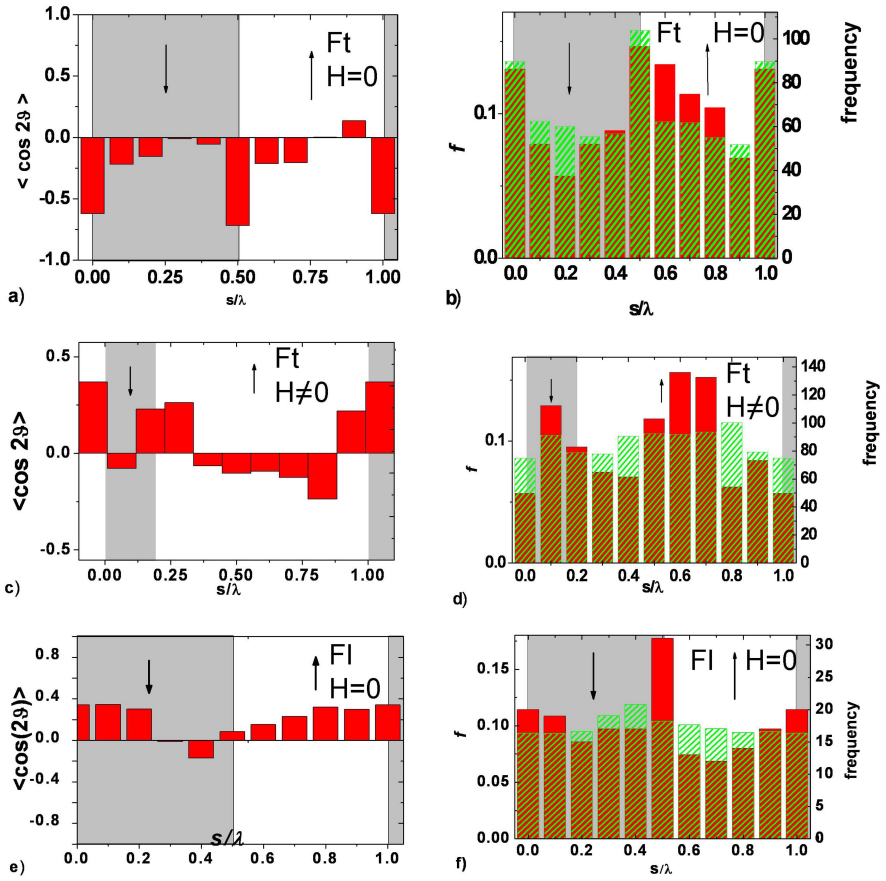

Figure 3.7: a), c) and e) show the orientation $< \cos 2\theta >$ and c), d) and f) probability density f of (i) type FT (a-d) and (ii) type FL (e and f) nanorods above the garnet film as a function of the position s/λ in the labyrinth. The data in a), b), e) and f) are all in the absence of an external field, while figures c) and d) correspond to an external field of H_{ex} =6.5 kA/m. The red data were obtained in a 7% aqueous H_2O_2 solution. The green crosshatched data of the probability density was calculated from the orientational data to the left via equation 3.3

there seems to be a slight preference for an orientation of the rods perpendicular to the domain walls. According to equation 3.3, this would result in a preference for the rods to reside in the interior of the domains as observed in Figure 3.7(d). The preference for the stripe interior however, appears to be larger (red columns) than what is expected on the basis of the orientational data (Figure 3.3(c)) as indicated by the green crosshatched columns. Overall we find the rods are less oriented and distributed more uniformly across the labyrinth structure as compared to the no field case.

3.4.3 Longitudinally magnetized ferromagnetic rods

In case of the type FL rods, the magnetic moment points either in (type FL+) or against (type FL-) the direction of the platinum end. Figure 3.7(e) and (f) shows the orientation $< \cos 2\theta >$ and the probability versus s/λ for type FL+ rods. As a result of the direction of the magnetic moment the orientational order of these rods differs significantly for the domain walls located at $s/\lambda = 0$ and $s/\lambda = 1/2$. Figure 3.7(e) shows the orientation of the rods. The rod prefers to pass normal ($\langle \cos 2\theta \rangle > 0$) over a $s = 0$ domain wall with the magnetic field oriented in the direction of motion. If the magnetic field above the domain wall is antiparallel to the direction of motion, then $s/\lambda = 1/2$ and the rod passes over the domain wall at an oblique angle showing no preferred orientation. Figure 3.7(f) shows the probability density, *f*, of the (type FL+) rods versus s/λ. As expected from equation 3.3 we observe a minimum of *f* at $s/\lambda = 0$ and a maximum at $s/\lambda = 1/2$. These data prove that the distribution of rods above the heterogeneous garnet film is dominated by the autonomous motion, which does not require the rods to comply with the magnetic energy considerations.

3.4.4 Paramagnetic Rods on a Garnet film

Figure 3.8 shows a time sequence of the position of a Type P rod on the garnet film. As indicated by figure 3.8, the domain walls are strong enough to confine the rods above the garnet film since the rods try to minimize their magnetic energy by placing themselves above the domain walls. As a result the rods are oriented parallel to the domain wall and their motion is purely one-dimensional with the rods traveling along the path dictated by the domain walls. In fact all the rods are guided by the garnet structure.

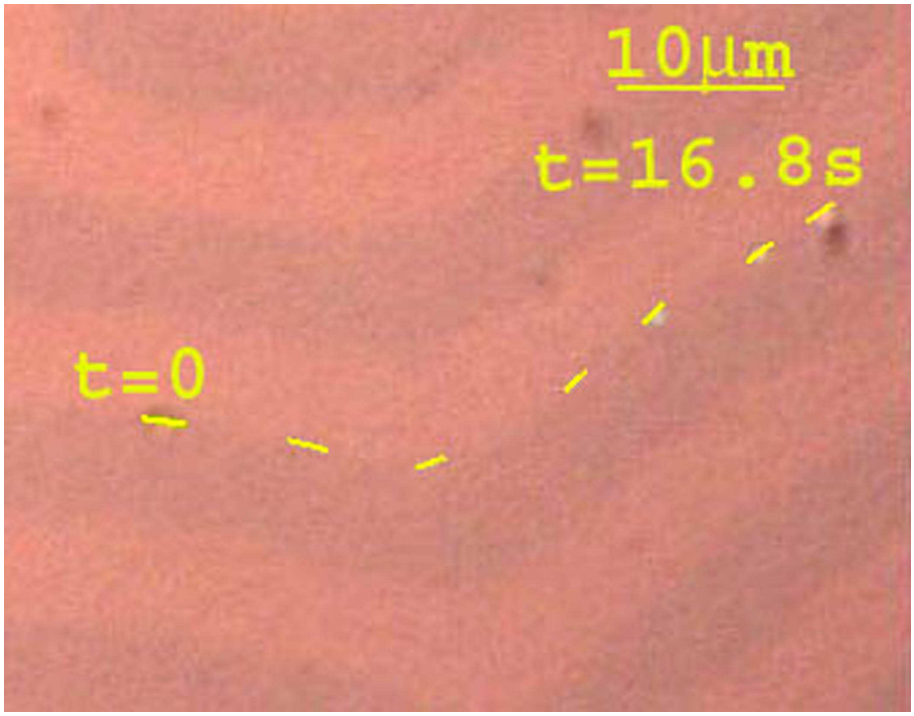

Figure 3.8: Overlay of polarization microscope images of a type P rod (yellow) on a magnetic garnet film. A time sequence ($\triangle$t=2.8 s) of the motion along a domain wall of one rod (t=0,.. 16.8s) is shown.

Therefore the strategy of using paramagnetic instead of ferromagnetic rods for achieving guided motion was successful in our case. The ferromagnetic rods performed a roving motion while the paramagnetic rods performed a guided motion. The reason behind this difference in the motion was understood by looking at the energies involved. As indicated in the table the thermal energies of the magnetotactic bacteria and rods are weak when compared with the magnetic and propulsion energies. The magnetic energy of the type P rods is larger than the propulsion energy and the opposite is true for type FT rods. For the magnetotactic bacteria and the type FL rods these energies are comparable. Therefore one can say that there is an interplay of the energies that cause the different kinds of motion. For the type P rods since the magnetic energy is higher, it confines the rods to the domain walls and the propulsion power moves it forward. On the other hand in case of the ferromagnetic rods the

Navigator	E_m/k_BT	$P/\gamma k_BT$
Magnetotactic Bacteria	4.6×10^3	5.5×10^3
type P	5.7×10^3	100
type FT	22	100
type FL	98	100

Table 3.1: Magnetic and propulsion energies of the navigators above the garnet film. Magnetic energies were calculated as $E = \mu_0 m M_s$, (μ_0 is the permeability of vacuum, M_s the magnetization of the garnet film). The magnetic moment m is the permanent ferromagnetic moment for the ferromagnetic navigators and the induced paramagnetic moment is taken from the SQUID measurement in figure 3.3at a field of H=M_s. The propulsion energy is obtained by measuring the power a $P = f\eta l v_2$ with $f \approx 20$ the friction coefficient of the navigator, η the viscosity of water, l the length of the navigator and v its velocity outside the magnetic field. $\gamma = v/l$ is the shear rate.

propulsion power of the rod easily overcomes the magnetic energy landscape. The random distribution in Figure 3.7 (red columns) also indicates that the motion of the rod eliminates the equilibrium behavior, and the location of the rod is dominated by autonomous motion rather than by magnetic energy.

3.5 Summary and Conclusions

The results suggest that guidance of the navigators is best achieved if they are paramagnetic and there is synergy between the autonomous motion and the field guidance. For the ferromagnetic bacteria the field direction is in conflict with the desired propulsion direction. In case of dominating magnetic energies this leads to trapping of the bacteria at the domain walls. Frustrated guidance was achieved for the minority fraction of freed magnetotactic bacteria along the stripe direction. The ferromagnetic rods performed a roving motion while the paramagnetic rods performed a guided motion. It is clear from the results that an interplay of the magnetic and propulsion energies leads to these differences in motion. If the magnetic energy is larger than the propulsion energy the navigators are trapped by the domain walls. Conversely dominating propulsion power overcomes the magnetic constraints leading to an overall statistical motion of the rods. Thus in principle one could switch between the roving and guided motion by merely changing the ratio of magnetic energy versus propulsion power of the navigators. Therefore it is desirable to identify magnetic nano shuttles with tunable propulsion properties such that varying the propulsion power would allow a switching between guided and roving motion simply by varying the amount of propellant, while keeping both the magnetic and the propulsion energy well above the thermal energy. One might also use a paramagnetic to ferromagnetic transition to control the different modes of navigation. This might be done by changing the temperature or in some cases by photoexcitation. This would enable future magnetic nano shuttles to be guided to a specific target and then allowed to disperse at will. Such navigators have the potential to find widespread application in drug delivery and distribution.

CHAPTER 4

Orientation of Overdamped Magnetic Nanorods

In the preceeding chapters we outlined the different aspects of motion of the bimetallic nanorods. As was indicated in the introduction, miniaturization also causes thermal and nonthermal fluctuations to play an important role in the motion of active components. Therefore, dissipation is also a major concern in the manufacturing of nano motors. Upon miniaturization the ratio of dissipation versus the driving power increases when using the same power source. Therefore in this chapter we will focus our attention towards using dissipation in the system to our advantage to guide the orientation of transversely magnetized nanorods when placed in a precessing magnetic field on a surface in a viscous liquid. We show that over damped magnetic nanorods driven by a rotating magnetic field undergo a series of reorientations when sedimenting on top of a surface in a viscous liquid. By changing the amplitude and the rotation frequency of the driving magnetic field the nanorod either synchronizes or desynchronizes with the field and rotates either around its long or short axis. The motion of the nanorods are coupled to creeping flow equations to theoretically describe the different regimes of the orientation. It is shown that friction anisotropy plays an important role for the orientation of the nanorods.

4.1 Background and Introduction

Gyroscopes on the macroscale are important for navigation. The operation of a gyroscope depends on the stability of a top to be oriented upright while spinning at high frequency. Miniaturization would require effective navigation tools as well. However gyroscopes on the nanoscale are rare [76–78] since dissipation becomes a major concern upon miniaturization.

Upon miniaturization the ratio of dissipation versus the driving power increases when using the same power source which hinders the proper functioning of the nanomotor. To overcome these limitations one is required to use more energetic chemical power sources compared to physical power sources. The recent synthesis of a rich variety of molecular motors [79] , shuttles [80–82] and rotors [83, 84] has inspired scientists to create artificial machines based on chemical, biochemical or optical interactions. One example is a molecule undergoing a unidirectional $\pi/3$ intramolecular rotation around a single bond [30] . Others use successive isomerization [85, 86] or stimuli induced binding affinity changes in mechanically interlocked molecular rotors for the rotation [87] .

On the other hand one could completely accept this dominance of fluctuations and dissipation and exploit it to achieve directed motion. Brownian motors [88], molecular transport processes [89], thermally activated transitions in a potential landscape [90], thermal fluctuations in an optical trap [91], parametrically modulated magnetic traps, or stochastic resonance [92], all use these fluctuations to their advantage to achieve directed motion.

In this chapter we focus our attention towards using dissipation in the system to our advantage to guide the orientation of transversely magnetized ferromagnetic nanorods when placed in a precessing magnetic field on a surface in a viscous liquid. We show that the rod undergoes a series of reorientations as a function of the frequency and amplitude of the rotating magnetic field. These reorientations result from a competition between the tendency to minimize the gravitational energy of the system, the power supplied to the rod by the rotating magnetic field, and the power dissipated by the rotating rod to the viscous liquid. The different regimes of the reorientation will also be theoretically explained. Since we are at low Reynolds number the creeping flow equations (explained in Appendix A) are coupled to the motion of a rigid rod.

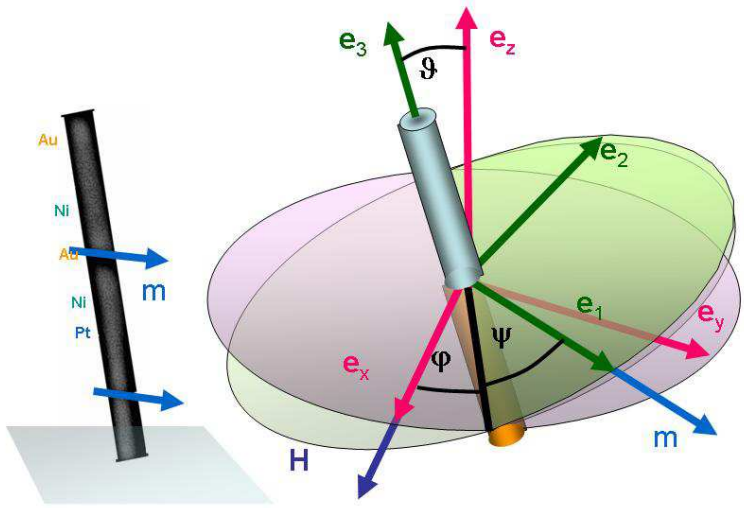

Figure 4.1: (Left) Electron microscopy image of a magnetic nanoscope of length 2.6 μm, showing the different nonmagnetic and magnetic segments of the rod. The rod is placed on top of a glass surface and is set into rotation by a magnetic field precessing around the surface normal. The scheme on the right shows the rod in the rest frame of the magnetic field together with the definition of the three Euler angles, ϑ, ϕ, ψ

4.2 Experimental Setup

The transversely magnetized FT rods, described in subsection 3.1.3, are dispersed in a viscous fluid (water or glycerol/water mixture) and placed on the top of a glass surface. An in-plane rotating magnetic field of frequency Ω is applied by two coils placed perpendicular to each other connected to an amplifier being fed by a wave generator. The alternating currents applied to the two coils differ in phase by $\pi/2$ such that the net magnetic field in the plane rotates around the z-axis with frequency Ω.

The rods sediment at the glass surface and are observed in the transmission mode

using a microscope (Leica, DMLP). The observations were recorded using a Basler A300 color camera. Magnetic fields were recorded using a Gaussmeter. Figure 4.1 describes the experimental setup.

4.3 Results and Discussions

It is found that rods undergo a series of reorientations as the frequency of the applied field is changed. Initially, for low frequencies ($\Omega < 9Hz$), the rods rotate synchronously with the magnetic field around the z-axis normal to the glass surface ($\vartheta = \pi/2$). As the frequency is increased, at a certain threshold frequency ($\Omega_1 = 9Hz$), the rods suddenly switch orientation from a planar ($\vartheta = \pi/2$) to a vertical ($\vartheta = 0$) alignment. Above Ω the rod starts to rotate around its long axis (which appears as a point in the plane of observation). When we further increase the frequency, the rods switch their orientation once again and lie down in the plane. However this time they rotate asynchronously with an angular frequency $\omega < \Omega$ less than that of the applied magnetic field. The lower threshold frequency Ω_1 seems to be nearly independent of the magnetic field while the upper threshold frequency, Ω_u, monotonously increases with the magnetic field ($d\Omega_u/dt > 0$). It is also observed that there exists a minimum magnetic field $H_{min} = 56A/m$ at which the lower and upper threshold frequency becomes the same. Below this field there is no vertical alignment of the of the rods whatever the frequency. We also found that both Ω_1 and Ω_u decreases as we increase the viscosity of the fluid by using glycerol/water mixtures while H_{min} increases as the viscosity increases. These results are summarized as a phase diagram in Figure 4.2.

The reorientation of the rod is explained as the tendency of the system to minimize the potential energy if the system is close to static (small Ω) or if there is insufficient power supply (small H). If the system is dynamic (large Ω) and the supply of power is sufficient (large H) the system will try to minimize the entropy production and rotate around the axis of least friction (the long axis). The dynamics of the motion of the rod can be attributed to three torques - a magnetic torque , a gravitational torque and a viscous torque. To calculate the effects of these we consider two moving Cartesian coordinate systems. As shown in Figure 4.1 the first system (x,y,z) is spanned by the direction of the magnetic field along the x-axis, the y-axis and the z-axis normal to the glass surface. The system rotates with frequency Ω with respect to the laboratory system. The second coordinate system is fixed to the rotating

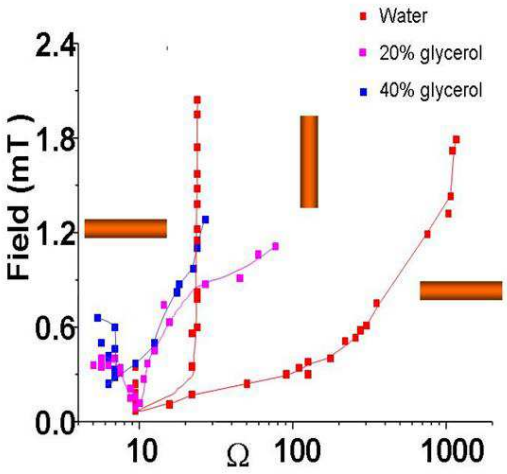

Figure 4.2: Phase diagram for the rod orientation as a function of the precession frequency Ω and field strength $\mathbf{H}$ of the magnetic field for different viscous fluids.The plot shows both Ω_1 and Ω_u decrease as we increase the viscosity of the fluid by using glycerol/water mixtures while H_{min} increases as the viscosity increases.

rod with unit vectors $(\mathbf{e}_1, \mathbf{e}_2, \mathbf{e}_3)$. The unit vector $\mathbf{e}_1$ points along the magnetization of the rod and $\mathbf{e}_2$ is normal to the rod while $\mathbf{e}_3$ lies along the long axis of the rod. A rotation matrix $R(\vartheta, \phi, \psi)$ transforms the (x,y,z) system to the rod coordinate system $(\mathbf{e}_1, \mathbf{e}_2, \mathbf{e}_3)$. The angles ϑ, ϕ, ψ are the Euler angles. Thus using these Euler angles the (x,y,z) system in the rod system is given by

$$\begin{pmatrix} \hat{\mathbf{e}}_\mathbf{x} \\ \hat{\mathbf{e}}_\mathbf{y} \\ \hat{\mathbf{e}}_\mathbf{z} \end{pmatrix} = \begin{pmatrix} a_{11} & a_{12} & a_{13} \\ a_{21} & a_{22} & a_{23} \\ a_{31} & a_{32} & a_{33} \end{pmatrix} \begin{pmatrix} \hat{\mathbf{e}}_\mathbf{1} \\ \hat{\mathbf{e}}_\mathbf{2} \\ \hat{\mathbf{e}}_\mathbf{3} \end{pmatrix}$$

where

$$a_{11} = \cos\psi\cos\phi - \cos\vartheta\sin\phi\sin\psi \tag{4.1}$$

$$a_{12} = \cos\psi\sin\phi + \cos\vartheta\cos\phi\sin\psi \tag{4.2}$$

$$a_{13} = \sin\psi\sin\vartheta \tag{4.3}$$

$$a_{21} = -\sin\psi\cos\phi - \cos\vartheta\sin\phi\cos\psi \tag{4.4}$$

$$a_{22} = -\sin\psi\sin\phi + \cos\vartheta\cos\phi\cos\psi \tag{4.5}$$

$$a_{23} = \cos\psi\sin\vartheta \tag{4.6}$$

$$a_{31} = \sin\vartheta\sin\phi \tag{4.7}$$

$$a_{32} = -\sin\vartheta\cos\phi \tag{4.8}$$

$$a_{33} = \cos\vartheta \tag{4.9}$$

The magnetic torque given by $\boldsymbol{\tau_{mag}} = \mu_0\mathbf{m} \times\mathbf{H}$ drives the motion of the rod (μ_0 is the vacuum permittivity, $\mathbf{m}$ is the magnetic moment of the rod and $\mathbf{H} = H\mathbf{e_x}$ is the magnetic field). The gravitational torque, written as $\boldsymbol{\tau_g} = mgl/2(\mathbf{e_3} \times \mathbf{e_z})$ (m is the mass of the rod, l its length and g the gravitational acceleration) destabilizes the upright orientation of the rod. While these two torques set the rod in motion the viscous torque $\boldsymbol{\tau_{vis}} = -\eta l^3\mathbf{k} \cdot (\boldsymbol{\omega} - \Omega\mathbf{e_z})$ (η is the viscosity of the fluid, $\boldsymbol{\omega}$ is the momentary angular frequency, and $\mathbf{k}$ is the friction coefficient tensor) counteracts the magnetic and gravitational torque. If we neglect the effect of the glass surface on the hydrodynamic dissipation the friction coefficient tensor is diagonal in the rod coordinate system with

$$k_{11} = k_{22} = \pi/(3(\ln 2l/d) - 1.45) + 7.5(1/((\ln 2l/d) - 0.2)^2) \qquad k_{33} = \pi(d/l)^2$$

where d is the diameter of the rod [93].

Using a balance of the three torques in the rod system we get three differential equations for the three Euler angles given by

$$\begin{aligned} \dot{\vartheta} &= \sin\vartheta[1 + \hat{H}\sin\phi\sin\psi] \\ \dot{\phi} &= \hat{\Omega} - \hat{H}\sin\phi\cos\psi \\ \dot{\psi} &= -\hat{H}(\kappa\sin\phi\cos\vartheta\cos\psi + \sin\psi\cos\phi)/(1-\kappa) \end{aligned} \tag{4.10}$$

To make the equations dimensionless we have used non-dimensional frequency $\hat{\Omega} = 2\eta l^2 k_{11}\Omega/mg$, time $\hat{t} = tmg/2\eta l^2 k_{11}$, magnetic field $\hat{H} = 2\mu_0 mH/mgl$ and the friction

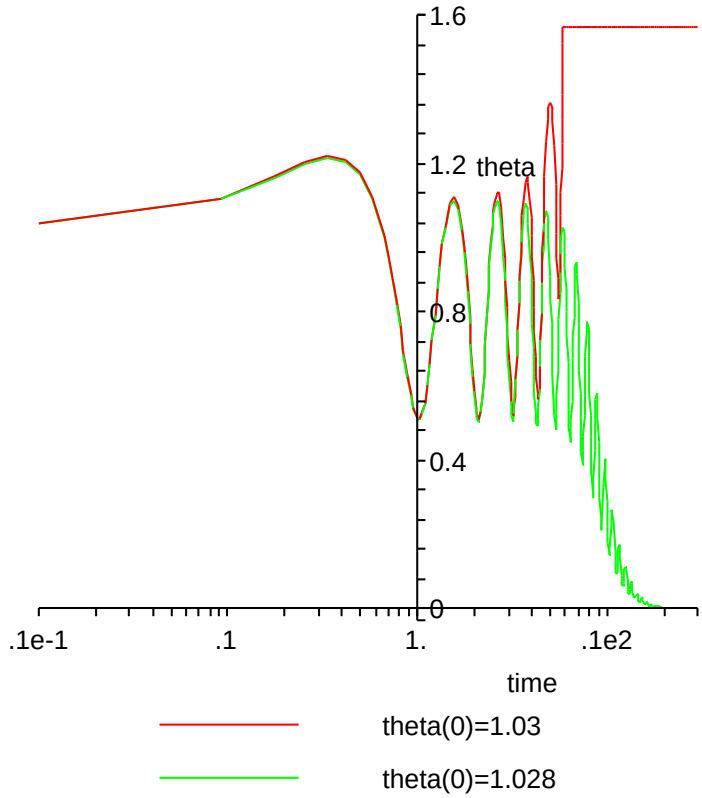

Figure 4.3: Plot shows the stability analysis of the orientation of two curves with slightly different initial conditions for θ in the unstable intermediate region

anisotropy $\kappa = (k_{11} - k_{33})/k_{11}$ with $0 \leq \kappa \leq 1$. The presence of the glass surface restricts ϑ to values below $\vartheta < \pi/2$. $\vartheta = \pi/2$, $\sin\phi = \Omega/H$ is a simple stationary planar solution if $\hat{H} > \hat{\Omega}$. $\vartheta = 0$, $\sin(\phi + \psi) = (1 - \kappa)\hat{\Omega}/\hat{H}$ is a vertical stationary solution for equation 4.10 if $\hat{H} > (1 - \kappa)\hat{\Omega}$. A third intermediate solution , $\tan\psi = 1/\hat{\Omega}$, $\sin\phi = \sqrt{1 + \hat{\Omega}^2}/\hat{H}$, $\cos\vartheta = -\sqrt{\hat{H}^2/(1 + \hat{\Omega}^2)}/(\kappa\hat{\Omega})$, for a magnetic field range $\hat{H}_2 < \hat{H} < \hat{H}_3$ where $\hat{H}_2 = \sqrt{1 + \hat{\Omega}^2}$ and $\hat{H}_3 = \sqrt{(1 + \kappa^2\hat{\Omega}^2)(1 + \hat{\Omega}^2)}$.

The linear stability analysis shows that the planar solution is stable for $\hat{H}_2 < \hat{H}$, the vertical solution is stable if $\hat{H}_2 < \hat{H} < \hat{H}_3$ or if $\hat{H}_1 < \hat{H} < \hat{H}_3$ where $\hat{H}_1 = \sqrt{4 + (1 - \kappa^2)\Omega^2}$ whereas the intermediate solution is unstable in the complete region of its validity. Therefore

the region $\hat{H}_2 < \hat{H} < \hat{H}_3$ is a coexistence region between planar and vertical stationary solutions and the system relaxes to either one of these stationary conditions depending on the initial conditions in the system. The unstable intermediate solution lies on a separatrix where the initial conditions relaxes back to the planar or vertical position. Figure 4.3 shows an example of this. For the two curves operating in the region $\hat{H} = 5$ and $\hat{\Omega} = 6$ ($\kappa = 0.8$), the rods attains either a stable vertical orientation ($\theta \to 0$) or a stable horizontal orientation ($\theta \to \pi/2$) depending on a slight variation in the initial condition for θ ($\theta = 1.03$ and $\theta = 1.028$). This shows that in the coexistence region (shown in pink in figure 4.4) both an upright orientation and laying flat are allowed depending on the initial orientation of the rod. As the intermediate stationary solution moves from $\vartheta = 0$ towards $\vartheta = \pi/2$ $\psi = \pi$, $\phi = -\arctan 1/\hat{\Omega}$, on lowering the magnetic field from $\hat{H} = \hat{H}_3$ to $\hat{H} = \hat{H}_2$, the catchment area of initial conditions for the vertical stationary solution increases continuously until it covers the entire accessible region where $\vartheta < \pi/2$. For magnetic field ranges between $\hat{H}_1 < \hat{H} < \hat{H}_2$ the vertical stationary solution is the only stable solution. For magnetic fields below $\hat{H}_1$ and $\hat{H}_2$ the system attains an asynchronous planar solution.

The results of this analysis along with the experimental results for the rods in water are summarized in the figure 4.4. We plot $\hat{\Omega}$ vs $\hat{H}$ for $\kappa = 0.8$. The experimental data is in blue overlaid on the theoretical regions. The coexistence region between the vertical and planar orientation is depicted in pink while the vertical phase is in red. We find reasonable agreement for the experimental upper threshold frequency Ω_u and theoretical lower threshold magnetic field while poor agreement is obtained for the experimental lower threshold frequency Ω_1 and the upper magnetic field $\hat{H}_3$. In fact the experimental vertical phase extends much further into the region of larger magnetic fields than $\hat{H}_3$ and the system is bound not by the magnetic field but by the lower threshold frequency. This discrepancy may be attributed to the fact that the problem was simplified in not taking into account any hydrodynamic interactions between the rod and the surface of the glass. The hydrodynamic interactions will destabilize the planar phase in favor of the vertical phase since the entropy production of the rod rotating synchronously increases in this case. At $H \approx H_0$ such destabilization does not occur since there is no sufficient power to stabilize the vertical orientation of the rod. In this case the viscous drag sets up a phase lag between the magnetization of the rod and the magnetic field such that the magnetic torque may lift the rod into the vertical position. Thus one would need to take into considerations facts such as the exact distance of the rod

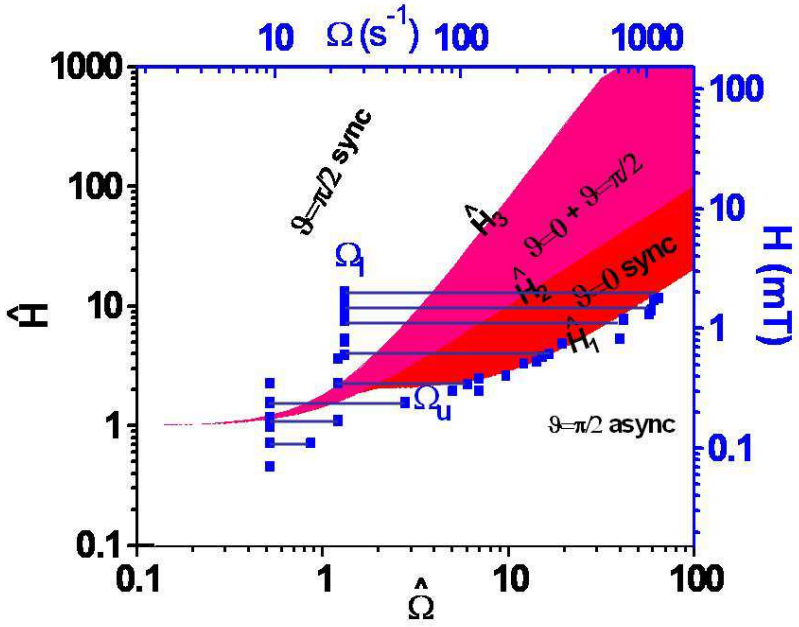

Figure 4.4: Experimental (blue) and theoretical phase diagram for the rod orientation as a function of the precession frequency Ω and field strength **H** of the magnetic field. The vertical orientation of the rod is for large frequency and large magnetic field (experimental region shaded blue, theoretical region in pink and red).

from the surface, etc. to get a more precise theory.

4.4 Summary and Conclusion

In this chapter we studied the effects of dissipation in the miniaturized system and showed that dissipation is important in micro and nanoscale objects. Here we used dissipation to our advantage to dynamically switch the orientation of transversely magnetized nanorods placed on a glass surface rotating in an external magnetic field from a horizontal to a vertical position. We found that by changing the amplitude and the rotation frequency of the driving magnetic field, the nanorod either synchronizes or asynchronizes with the magnetic field while rotating either around its long or short axis. We were able to theoretically explain the motion of the rod as a tendency of the system to minimize the potential energy or the entropy production and the power dissipated by the rotating rod to the viscous liquid. The creeping flow equations coupled to the motion of the rods provides theoretical regimes for the most stable orientation of the rods. It could also be concluded from the data analysis that friction anisotropy does have an important role to play as well in the exact definition of the boundaries for the different regimes. From here one could conclude that dissipation effects should be considered when designing efficient nanomotors and sometimes one can also use dissipation to ones advantage to have better guidance and control of the nanomotors. The nanorods used in our study can be used as efficient dynamic switches when incorporated into microfluidic devices. They could be used as microgates for microchannels or as microstirrers that exhibit chaotic intermittent motion when operated close to the planar to vertical transition.

CHAPTER 5

Curvature Driven Motion of Colloidal Particles using a Magnetic Ratchet Potential

In chapter 3 we explored the strategies for achieving guided motion of autonomously moving nanorods while in Chapter 4 we used dissipative motion to achieve orientation in the magnetic nanorods. In this chapter we use dissipative motion and Brownian motion to study the dynamics of induced motion in colloidal particles. Directed motion is induced in paramagnetic colloidal particles as well as magnetically labeled biological cells by using a ratchet effect. Ferrofluid ingested mouse macrophages were placed on a magnetic garnet film with alternating stripe domain patterns and a pulsating magnetic potential was provided by superposing an oscillating magnetic field normal to the film. The symmetry of the resulting periodic stripe potential was broken locally by the curvature of the stripes. We show both experimentally and theoretically that a minimum curvature of the stripe patterns in the film is required to induce this driven motion.

5.1 Background and Introduction

Colloidal particles are used extensively in medical, biochemical and biophysical fields because of their variety in chemical and biological functionalities. They have been used for novel forms of DNA-sequencing [94] , optical bar-coding [95], as carriers of biomolecules and proteins in microfluidic channels [96], and as fluorescent markers in microrheological experiments of the cytoskeleton [97–102]. Magnetic manipulation of paramagnetic colloidal particles and ferrofluids is used extensively in medicine and in developing microfluidic devices for biomedical analysis. Various biological cells like the Jurkat cells were separated from the blood using CD3 coated magnetic particles by trapping them in a microchannel [103]. Magnetic Eschera coli cells attached to 2.8 m Dynabeads were captured and isolated from blood samples on a microdevice using an external magnetic field [104]. Magnetic colloidal particles are also used in the hyperthermia treatment of cancer [105–108], in which magnetic field gradients are first used to collect and enrich these particles in the cancerous part of the human body and then destroy the cancerous tissue using high frequency magnetic fields that heat the particles and thus the tissue. Important issues such as the compatibility and non toxicity of these particles [109] in the human body have been addressed extensively and they can be used directly when manipulating the same kind of particles in vitro on microfluidic devices that analyze or detect specific chemical or biological species. Magnetic field gradients, generated by various means have also been employed to capture cells attached to paramagnetic beads. Magnetic fields created in microscopic devices are not just limited to spatial variations on the macroscopic scale but magnetic fields can be varied also on the colloidal scale.

In this chapter we use the magnetic fields varying on the colloidal scale to manipulate magnetically labeled biological cells. Magnetic heterogeneities are produced by the self assembled domains of the magnetic garnet film (Section 3.1.1). An external oscillating field modulation renders the magnetic field heterogeneities time dependent and the magnetic particles are in a non-equilibrium environment. Transport is then achieved by using a ratchet effect which relies on an asymmetric, symmetry broken periodic potential where non-equilibrium fluctuations or oscillations generate a net current. Ferrofluid ingested mouse macrophages and paramagnetic particles were placed on a magnetic garnet film and the dynamics was studied. Experimental and theoretical results reveal that a minimum curvature

of the stripe pattern is required to induce driven motion in the macrophages. It was further proved that a slight perturbation in the system in the form of a change in a parameter (for example a change in the particle size, or the friction coefficient) can influence the driven flow.

5.1.1 Ratchet Effect

Directed transport can be achieved on the colloidal scales by converting unbiased non-equilibrium fluctuations into useful work by using an asymmetric ratchet potential [110]. A ratchet potential is a periodic potential that exhibits a broken spatial symmetry. The most essential requirement of the ratchet effect is the presence of random or deterministic noise which plays a dominating role such that the direction of flow cannot be predicted a priori without any mathematical calculations. Further a certain periodicity is required in the operating device along with some broken symmetry and time dependent forces. These work together to produce a net current, the direction and quantitative description of which cannot be easily predicted.

Figure 5.1 shows a simple asymmetric potential where the direction of motion cannot be easily predicted. The ratchet effect is extremely sensitive to system parameters and one can achieve a "*current reversal*" upon a small variation of the system parameter [111]. A vanishing current is associated with an *accidental symmetry*. An *accidental symmetry* may be an exceptional occurrence or a fine tuning of the parameters which would not occur under typical experimental conditions. As a result of its "accidental" origins, this symmetry may be destroyed merely by a small perturbation. This is unlike the symmetry broken case where the symmetry once broken cannot be easily restored by a slight variation of a system parameter. For example an asymmetric potential maynot be easily converted to a symmetric potential (stable broken symmetry). On the other hand, in the case of an accidental symmetry, a slight change of any parameter of the model (size of particle, friction coefficient, viscosity) may cause an immediate reappearance of the current explaining the current reversal. Ratchet potentials can be of various kinds depending on the potential and the origin of the fluctuations. A rocking ratchet potential , a pulsating ratchet potential are a few examples.

In this work we use the magnetic garnet film from section 3.1.1 to create a pulsating magnetic

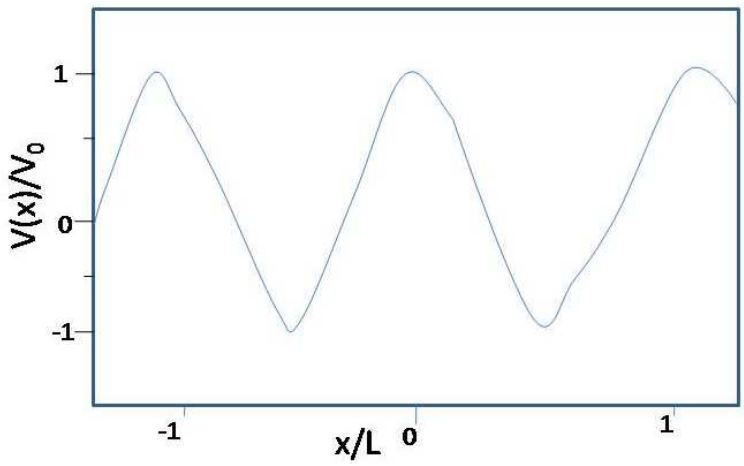

Figure 5.1: Asymmetric potential as a function of time

ratchet. The alternating stripe patterns produce a periodic potential while the curvature in the stripe pattern introduces an asymmetry in the system. An oscillating external magnetic field modulation introduces non-equilibrium fluctuations in the system. Thus this setup serves as a ratchet potential to induce motion in magnetic particles on the colloidal scale.

5.2 Experimental Set-Up

A physiological solution of Pixie H32.12 mouse macrophages (See Chapter 7.6 for a detailed description of the culture process) and aqueous solution of paramagnetic particles were placed on the magnetic garnet film. The cells were counted and checked for viability before they were used for the experiment. Figure 5.2 shows the schematic of the experimental setup.

An external modulating magnetic field of frequency 3 Hz oriented normal to the film was provided by a coil placed under the garnet film. The modulations in the field were achieved by connecting the coil to an amplifier being fed by a wave generator. An interplay between gravity and the electrostatics are efficiently able to confine the cells at a plane a few nanometers above the surface of the garnet film. The cells along with the stripe pattern

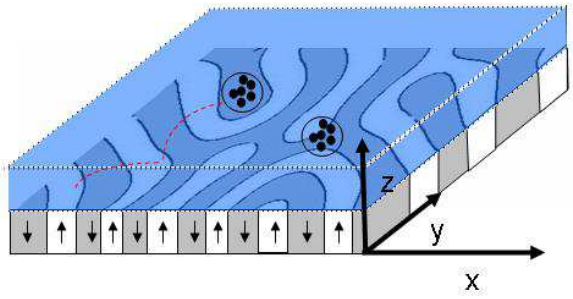

Figure 5.2: Scheme of a magnetic garnet film with alternating magnetized stripe domains. Cells doped with paramagnetic particles are immersed in an aqueous solution above the film and are transported perpendicular to the stripe pattern when the film is modulated with an oscillating external magnetic field normal to the garnet film.

were observed using a polarization microscope (Leica, DMLP). The motion of the cells was followed by using a color camera and videos were recorded at 25 fps.

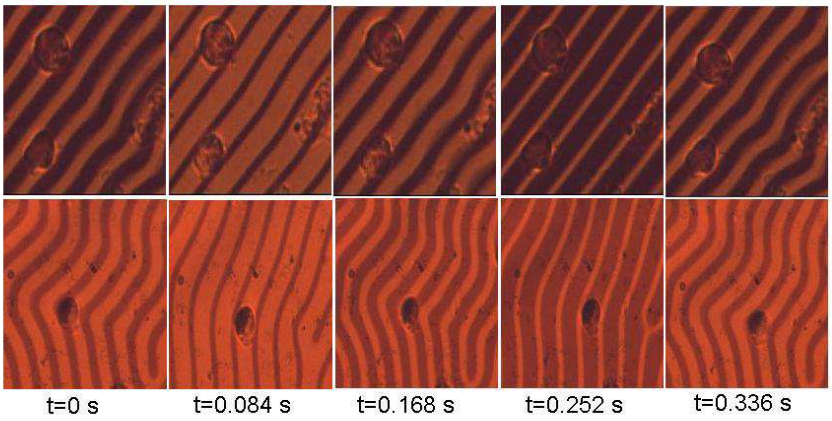

Figure 5.3: Polarization microscope images of a macrophage with phagocytized ferrofluid above the garnet film. The domain structure of the magnetic field is visualized making use of the polar Faraday effect. The sequence of images shows the motion of the macrophage above a straight (top) and above a curved (bottom) stripe domain pattern of the garnet film during one modulation period.

5.3 Results and Discussion

5.3.1 Mouse macrophages

As seen in figure 5.3, in the absence of an external magnetic field the magnetic domains of the garnet film have equal widths for the up and down magnetization. Consequently the fields above both domains have equal field strengths but are opposite in orientation. The strongest magnetic field lies at the domain walls. Thus the ingested ferrofluid and hence the macrophages are attracted to the domain wall as seen in Figure 5.3(t=0). Now

the application of an external field normal to the film would cause the domain having a magnetization parallel to the external field to increase in size while the size of the anti-parallel domain decreases (Figure 5.3). As a result the magnetic field strength above the majority domain increases at the expense of the minority domain. This causes the macrophages to move from the region above the domain wall to the interior of the majority domain since the ferrofluid gets attracted to the majority domain. At t=T/4 (=0.084s), the cells move into the upward magnetized majority domain as seen in Figure 5.3. At t=T/2 (=0.168s) the net external field is zero and the upward and downward magnetized domains are once again of the same width and so the cells return to a domain wall (Figure 5.3). During the next half cycle the applied magnetic field switches direction and so now the downward magnetization is parallel to the external applied field. Therefore at t=3T/4 (=0.252s) the cell is in the downward magnetized domain (dark stripes) as seen in Figure 5.3 while at the end of the cycle t=T (=0.336s) the cells come back to a domain wall. However there is a difference in the motion of the cells in Figure 5.3(top) and (bottom). Figure 5.3(top) shows a macrophage above a region with a straight stripe pattern while in Figure 5.3(bottom) the macrophage is above a curved pattern with curvature $\kappa \approx 0.085\mu m^{-1}$. As is clear from the images, the macrophage above a straight stripe returns to the original domain wall when the field returns to zero while the one over the curved path moves towards the next domain wall on the concave side of the stripe pattern. Thus a macrophage over a curved domain proceeds by one wavelength of the stripe pattern $\lambda = 12\mu$m in the concave direction at the end of one complete cycle of the external field while the macrophage over the straight domains comes back to the original wall where it was before the application of the field.

Thus for macrophages over the curved regions we obtain a net motion with speed $\upsilon = \lambda f$. This is seen in Figure 5.4 where the motion of the cells are followed over longer times up to 5 cycles. In figure 5.4 (top), the macrophage above the straight stripes remains at its location while the one above the curved stripes (figure 5.4 (bottom)) proceeds by 5 $\lambda = 60$ μm. Thus motion is induced in the macrophages depending on the shape of the stripe pattern on which it is positioned. The observation for 56 different macrophages is summarized in Figure 5.5. The probability, P, of the macrophage to move forward in the concave direction is plotted as a function of the normalized curvature $\kappa\lambda$. From our observations we concluded that macrophages are less inclined to move if the curvature is below $\kappa\lambda < 0.5$ but above this value they do move deterministically in one direction. Thus one may use the curvature of

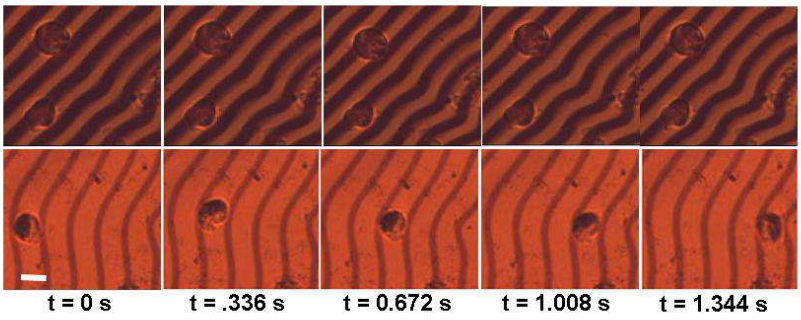

Figure 5.4: Polarization microscope images of a macrophage with phagocytized ferrofluid above the garnet film. The sequence of images shows the motion of the macrophage above a straight (top) and above a curved (bottom) stripe domain pattern of the garnet film during 5 cycles.

the stripe pattern to guide the macrophages along a predetermined path on top of the film. The motion is digital with an exact progression of one wavelength per cycle thus enabling us to have exact information of the location of each individual cell.

Similar to the mouse macrophages, the beads present at a curved domain wall hop towards the convex direction 5.6.

In the absence of an external magnetic field , the field strengths in the different domains are equal. The beads are therefore found at one domain wall. As external field increases the width of the domains changes and as before at t=T/4 (=0.084s) the beads move into the upwards majority domain while at t=1/2T they are back to a domain wall again. As the magnetic cycle proceeds the beads are pushed into the downward majority domain (t=3T/4)

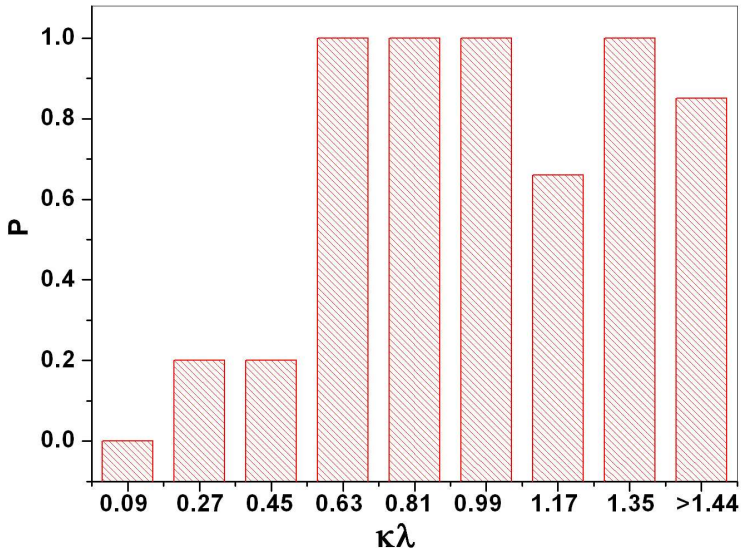

Figure 5.5: Experimentally determined probability, P, of hopping in the direction of the stripe curvature after one cycle, plotted as a function of the normalized stripe curvature.

while after one cycle the beads move to the next domain wall. However it was noticed that unlike the mouse macrophages, even the beads on the straight portions of the stripe pattern were found to hop in the same direction as the nearby beads on a curved domain wall. This can be attributed to the fact that a current reversal probably occurred by changing a parameter, namely the size of the magnetic particle resulting in a biased current directing the motion. This was further proved by the fact that we were able to apply an external field ($H_{x/y}$= 1.74 mT for a normal field of 0.35 mT) in the x/y direction which was able to stall this movement. Above this field the motion of the beads switched from being curvature driven to being driven by the direction of the external field in the x/y direction.

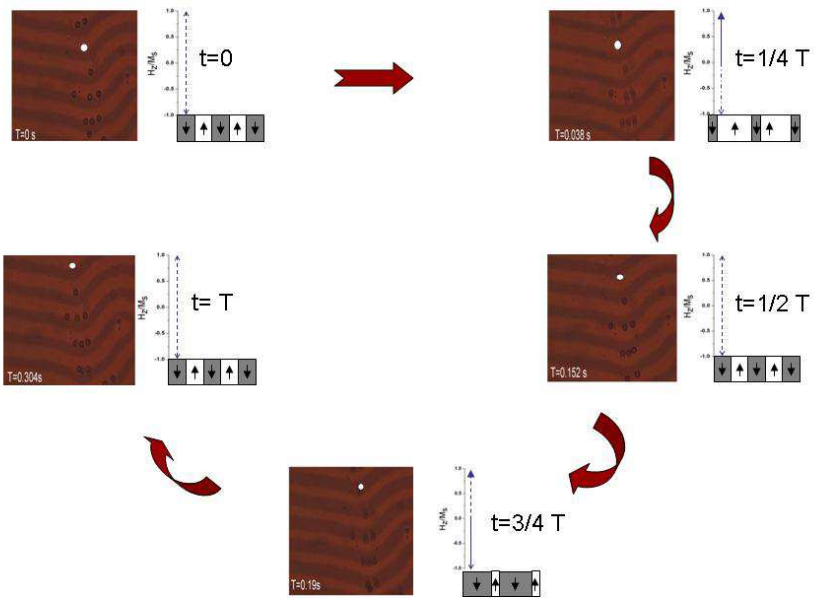

Figure 5.6: Image sequence of the motion of paramagnetic beads on a magnetic garnet film when a oscillating magnetic field is applied perpendicular to the film.

5.3.2 Simulation of Ratchet Potential

The motion of the magnetic particles can be modeled by an overdamped Langevin equation across a cylindrical symmetric (coordinates r,z,ϕ) stripe pattern

$$\nabla U(r,z,t) = -\eta \dot{\mathbf{x}} + \mathbf{F}_{random} \tag{5.1}$$

with a magnetic potential $U(r,z,t) = -\mu_0 \chi_{eff} V \mathbf{H^2}(r,z,t)$ that is proportional to the square of the magnetic field, $\chi_{eff} = 0.8$ and $V \approx 2.7 \times 10^{-15}\ m^3$ of the ingested ferrofluids and a fluctuating random force F_{random}. The magnetic field of the cylindrical stripe pattern of wavelength λ can be written as a sum of the magnetic fields $\mathbf{H} = \Sigma \pm \mathbf{H}_{m,\pm}$ from the magnetic bubble domains of radius $R_{m\pm} = m\lambda \pm d/2$, $m = 1, 2, 3 \ldots$ that are modulated in width as a function of time by $d = \lambda/2 + \hat{d} sin(\omega t)$. The magnetic field of a single bubble $\mathbf{H}_{m,\pm}$ is given by

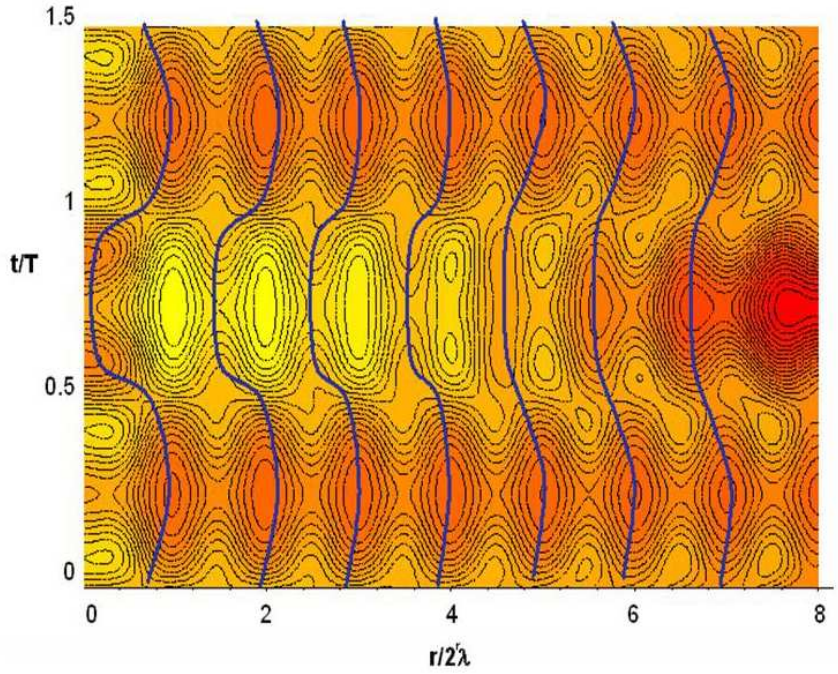

Figure 5.7: Image of the simulation of a ratchet potential above a magnetic garnet film

$$\frac{(H_{m\pm,r})}{M} = \mp\sqrt{\frac{R_{m\pm}}{r}}Q_{1/2}\frac{r^2+R_{m\pm}^2+z^2}{2rR_{m\pm}} \tag{5.2}$$

$$k_{m\pm} = \sqrt{\frac{4rR_{m\pm}}{z^2+(r+R_{m\pm})^2}} \qquad n_{\pm} = \frac{2r}{r\pm\sqrt{r^2+z^2}} \tag{5.3}$$

$$\begin{aligned}\frac{(H_{m,x\pm})}{M} &= \pm\frac{2}{\pi}\frac{(\sqrt{(r^2+z^2)}-R_{m\pm})(\sqrt{(r^2+z^2)}-r)\Pi(n_+,k_{m\pm})}{z\sqrt{(r+R_{m\pm})^2+z^2}} \\ &\quad +\frac{(\sqrt{(r^2+z^2)}+R_{m\pm})(\sqrt{(r^2+z^2)}-r)\Pi(n_-,k_{m\pm})}{z\sqrt{(r+R_{m\pm})^2+z^2}}\end{aligned} \tag{5.4}$$

$Q_{1/2}$ is a Legrendre Function of the second kind and Π is the complete elliptic integral of the third kind.

Figure 5.7 shows a plot of the potential as a function of the radius and time t for an elevation of the ferrofluid of z = 1.4 μm. The periodic modulation leads to a periodic

change of the position of the energy minima above the film. At zero external fields the energy minima is located above the domain walls. When the external field is applied the minimum continuously oscillates around the domain wall position at the larger radii (blue lines). The changes in the energy minimum position with time become more pronounced at the lower radii $r < 8$ showing that the macrophages are more susceptible to hop at the strongly curved domain walls. The direction of the hopping however cannot be explained by the potential alone. As is inherent to the nature of ratchet the direction of motion is a complicated function of the noise level in the system. The curvature of the stripe domain pattern breaks the symmetry of the magnetic potential and hence the generic situation is a net current pointing in or opposite to the direction of curvature. In our experimental case this direction is in the direction of the curvature.

5.4 Summary and Conclusion

The results reported in this chapter show the use of non equilibrium fluctuations to induce directed motion in systems. Motion was induced in ferrofluid ingested mouse macrophages and paramagnetic particles placed on a magnetic garnet film with alternating stripe domain patterns and a pulsating magnetic potential is provided by superposing an oscillating magnetic field normal to the film. The symmetry of the resulting periodic stripe potential is broken locally by the curvature of the stripes. It is shown both experimentally and theoretically that a minimum curvature of the stripe patterns in the film is required to induce this driven motion. The observation that this minimum curvature condition was not seen in paramagnetic particles was attributed to a current reversal in the system. Thus the successful transportation of magnetically doped biological cells as well as magnetic particles was achieved in a precise manner where one is able to predict the location of the particles at each instant. Since this method of transport prevents the cells from not just getting lost but also losing its identity which is typical with most other magnetic transport mechanisms, it can be especially used for single cell assay studies on a lab-on-a-chip as well as for studies where we want to be able to track the cells while moving them around. Another use would be to separate cells on a lab - on -chip device where the cell of interest could be labeled magnetically by specific antibodies and could be separated from a mixture and moved to another region of interest. Drug delivery using ferrofluids is becoming a common technique and our method may be able to aid in studies relating to the efficiency of this technique. We have also presented how different transport modes result from the time dependent magnetic heterogeneities. This knowledge provides new avenues of transport, separation and distribution of micromaterial to the microfluidic arsenal that may be useful when dealing with a large amount of micromaterial.

CHAPTER 6

Protrusion Effects of a Sphere at an Air/Water Interface

In chapters 2-6, viscous dissipition was used to probe the mechanism of motion of active components, to guide and orient them. In this chapter we study the dissipative motion of diffusing interfacial beads to probe the protrusion effects due to electrostatic charges on microspheres at an air/water interface. The drag on the sphere immersed in an incompressible viscous monolayer has been calculated numerically [112] where Marangoni forces are shown to contribute significantly to the drag coefficients. The change in the mobility of the sphere with the ionic strength of the solution is analyzed to study the presence or absence of the electrodipping effects. The change in the mobility of a sphere at an interface may be affected by the Marangoni forces, interfacial and bulk viscous effects as well as immersion depth. Sikkert et al. have reported on the change in mobility of the interfacial beads in Langmuir monolayers [61]. The observed change was attributed to changes in surface viscosity. Here, the mobility of a sphere at an air/water interface is analyzed using the single particle trajectories for a non-viscous interface. Using the numerical results for the single particle theory of the sphere along with the experimental single particle mean square displacement we investigate the effect of electrostatic forces on the protusion of the sphere. The electrostatic forces on the sphere are altered by varying the electrolyte concentration of the water. Since the surface viscous effects are negligible, and Marangoni effects are maximal, changes in the single particle mean square displacement of the spheres are attributed to the changes in the protrusion. As the electrolyte concentration is changed no effect is observed for large particles while nanoparticles seem to protrude deeper into the water for higher ionic

strength. This suggests a size dependence of the beads on the geometric arrangement of the beads at the interface.

6.1 Background and Introduction

The mobility of colloidal particles as tracer particles has been used to study the rheological properties of interfaces. In turn the effects of the interface on particles are revealed by studying the rheological properties at the interface. Spherical particles that have been immersed into Langmuir monolayers at the air/water interface [61, 63, 113–115], into lipid bilayers in the form of giant vesicles [116–118], and into polarized biological cells where they were coupled to the plasma membrane [119] have been studied recently. Microrheology is the study of the thermal motion of tracer particles introduced into a viscous or viscoelastic material. One of the practical problems of interfacial rheology is the realization of an exclusively 2-dimensional surface. For most practical purposes a 2d surface is coupled to a 3-dimensional reservoir which modifies the mobility of the tracer particles. The tracer particles exert forces onto the three dimensional fluids as well as the interface that separates them. These forces lead to mechanical responses of both the fluids and the interface in the form of three- and two-dimensional flow and pressure fields acting back onto the particle. As a result the interpretation of the results of the tracer particle motion is a complex issue.

In this chapter, the translational drag is measured and fit by a modified Stokes-Einstein formula from which the immersion depth is calculated. The electrostatic forces on the spheres are altered by changing the electrolyte concentration of the bulk fluid. Using particle tracking, the mobility of the microspheres is studied to obtain the single particle mean square displacement of the tracer particles. The results suggest that the immersion depth changes with the electrolyte concentration of the bulk fluid reservoir to which the interface is coupled, suggesting that the electrostatic forces on the sphere contribute to the immersion. However this is observed only for smaller beads (170 nm) and not seen in larger beads (0.5 microns) suggesting that the size of the particle plays a role.

6.2 Experimental Section

Fluorescent dyed carboxylate modified microspheres of diameter 170 nm (0.346 COOH groups per nm^2) and 500 nm (6.7 COOH groups per nm^2) dispersed in water are passed through a column of ion-exchange resin bed to remove the soluble surfactants. These beads are then dispersed in an aqueous solution containing 80 % isopropanol. Small aliqouts of this mixture are carefully spread on ultrapure water in a teflon Langmuir trough with a glass

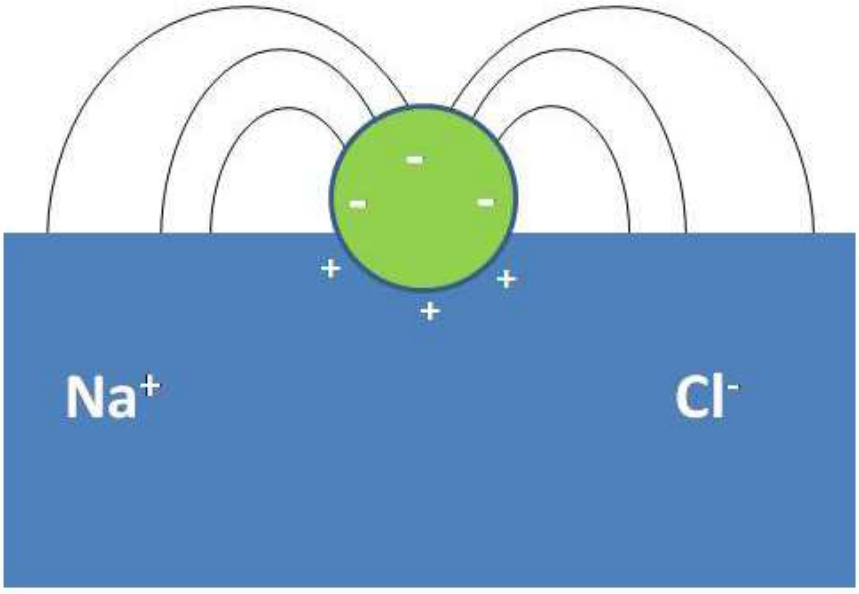

Figure 6.1: Scheme showing the experimental setup with the microspheres at an air/water interface. The electrostatic properties at the interface are varied by the addition of electrolytes into the bulk phase.

bottom. After waiting for more than half an hour to allow the isopropanol to evaporate the interface is observed using a LEICA fluorescence microscope connected to a CCD camera which is linked to a computer with WIN TV options. The macroscopic drifts in the system is reduced by using a plastic covering. The electrolyte concentration of the water is altered by adding various concentrations of NaCl solution. Images are recorded at 30 fps. Figure 6.1 shows the schematic of the experimental set-up.

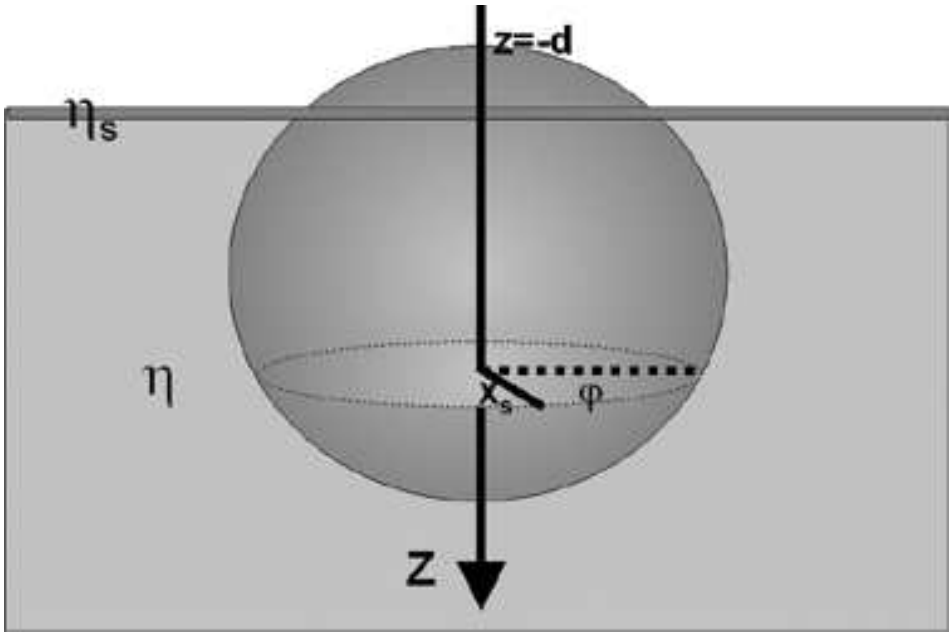

Figure 6.2: Image of the immersion of the sphere at the interface

6.3 Analysis and Results

After the evaporation of the isopropanol the carboxylate modified microspheres, when viewed under a fluorescence microscope, appear well separated and arbitrarily placed at the interface. They all perform Brownian motion. The movies are analyzed to track the mobility of the particles using a particle tracking program using the IDL software developed by John Crocker and David Grier with subroutines from Eric Weeks. The strategy followed here is to first process the 1st frame of the movie interactively to determine which particles need to be tracked (to make sure that we are not considering any aggregations of more than one particle and analyzing only particles at the interface) and then repeat everything for all the frames that need to be analyzed. Next one links the coordinates found in each frame together to form trajectories. The trajectories are then used to determine the vector displacements of the tracer particles $\Delta\mathbf{r}(t,\tau) = \mathbf{r}(t+\tau) - \mathbf{r}(t)$ where t is a absolute time and τ is the lag time. From the coordinates of the particles the one particle mean square displacements(MSD) are calculated, $\langle \Delta r^2(\tau) \rangle$. In 2-D interfacial systems coupled to a bulk fluid reservoir this one

particle MSD is related both to the immersion depth of the particle at the interface as well as the surface viscosity of the interface. In a normally diffusing system, the MSD is linearly increasing in time according to

$$\langle \Delta r^2(\tau) \rangle = 4D\tau \tag{6.1}$$

where D denotes the diffusion constant of the particle. The diffusion constant is related to the friction constant f via the Fluctuation-Dissipation Theorem (Stokes-Einstein relation):

$$f(\eta_s, d) = k_B T / D\eta a \tag{6.2}$$

where η_s denotes the surface shear viscosity, d the immersion depth (Figure 6.2) of the bead, η the bulk shear viscosity of water, k_B Boltzmann constant, T the temperature and a the bead radius. From the measurements of the MSD versus τ we may extract the diffusion constant D via equation 6.1. Inserting D into equation 6.2 then yields the friction coefficient $f(\eta_s, d)$.

Figure 6.3 shows the mean square displacement $\langle \Delta r^2(\tau) \rangle$ of the 170 nm microspheres as a function of τ at various electrolyte concentrations of the water for 1500 frames. From the plots it is seen that the slope of the curve decreases with increasing electrolyte concentration. Figure 6.4 shows the drag coefficient $f(\eta_s, d)$ as a function of the electrolyte concentration. The translational drag on a sphere is found to increase logarithmically with the electrolyte concentration.

Figure 6.5 shows the plot of the single particle MSD for larger particles with carboxylate modified surface (diameter = 0.5 microns) for two extreme limits of electrolyte concentrations ($I = 10^{-7}$ and $I = 0.01$). Here, the slopes of these two different sets are the same, i.e there is no significant change in the diffusion constant of the beads.

6.3.1 Fundamentals of a Sphere in a Monolayer

Hydrodynamic theories predict that the friction coefficient $f(\eta, d)$ depends on the rheological properties of the surface, the bulk rheological properties and the geometric arrangement of the bead in the interface. A proper understanding of the observed changes requires a theory that can explain the factors that may influence or induce a change in the diffusion constant. In the following, we discuss the different physical mechanisms acting on a diffusing bead.

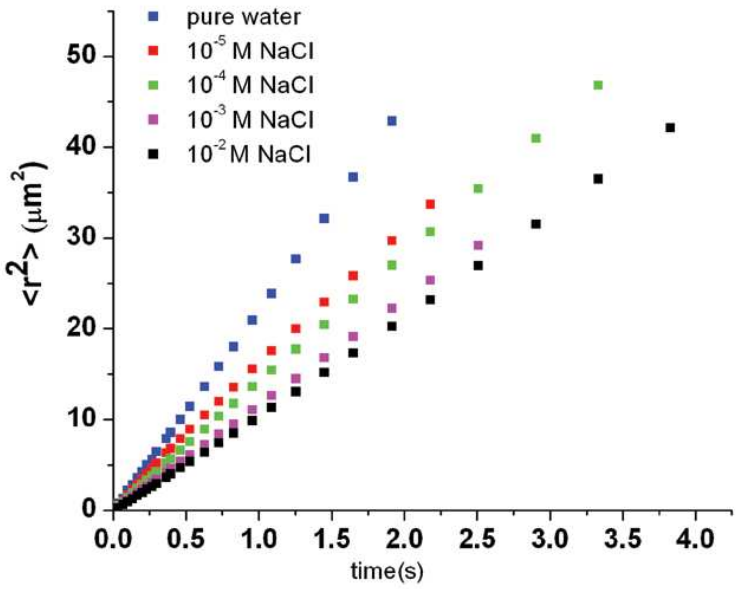

Figure 6.3: Plot of single particle mean square displacement (MSD) for carboxylate modified fluorescent microspheres (radius = 170 nm) vs. time for different concentrations of NaCl. The slope of the line decreases linearly indicating a direct correlation to the electrostatic charges on the particles.

The generation of forces on the tracer particles gives rise to Marongoni effects at interfaces. Marongoni stress is a tangential surface stress generated by gradients in surface density of surfactants. This stress becomes most pronounced in the limit of vanishing surface compressibility $\kappa_s \eta a \dot{\gamma} \ll 1$ (κ_s the surface compressibility, η the 3d viscosity, a the radius of the object moving in the interface and $\dot{\gamma}$ the shear rate). In this limit the Marangoni effects are simply incorporated into the theoretical description by approximating the surface or interface as incompressible. Marangoni effects often dominate over viscous effects as has been theoretically predicted by Saffmann, Hughes [35,120] and Stone [57] and experimentally confirmed by Peters [121] for proteins undergoing Brownian motion in membranes and by Klinger, Schwartz and Steffen and coworkers [58–60], and Wurtlitzer and coworkers [62] for

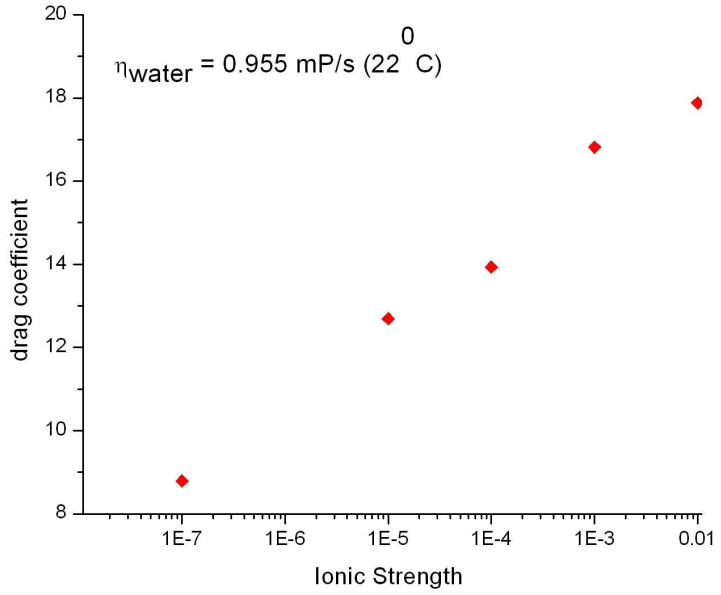

Figure 6.4: The drag on a sphere as a function of the electrolyte concentration of NaCl extracted from the mean square displacement (MSD) plots using a modified Stokes-Einstein formula for 170 nm sized particles at an air/water interface. The drag on the particle increases with increasing electrolyte concentration showing contributions due to viscous forces from the bulk water.

the motion of flat, circular objects embedded in a monolayer. Characteristic features of the incompressibility of the interface are logarithmic correction terms in the translational drag coefficients both in the high and low viscosity limits. Experiments evaluated with the formulas given by Danov et al. [**?**, 122] that lack these characteristics therefore lead to overestimation by an order of magnitude of the surface viscosity [61, 113, 116, 118] or an underestimation of the hydrodynamic radius of rafts [119] to which the colloidal beads are coupled [61]. Fischer et. al. [112] incorporate Marangoni forces into the treatment of a sphere immersed in a monolayer or a membrane by solving the equations for an incompressible interface. The translational, rotational and coupling drag coefficients are calculated for

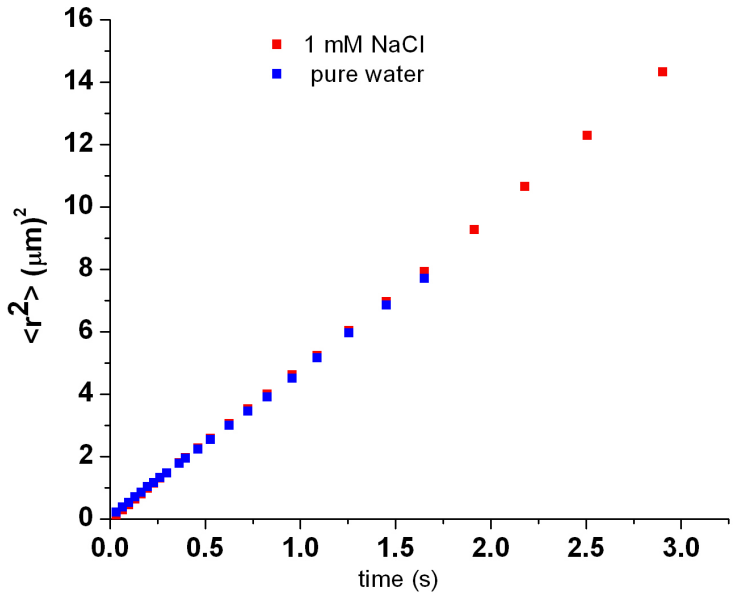

Figure 6.5: Plot of single particle mean square displacement (MSD) for carboxylate modified fluorescent microspheres (radius = 500 nm) vs. time for different concentrations of NaCl. The slope of the line is independent of the electrolyte concentration of the water. This implies that in this case the electrodipping effects are independent of the electrolyte concentrations.

objects incorporated into or near a two dimensional interface of surface shear viscosity η_s that is bounded by liquids of different or similar bulk viscosities η_1 and η_2.

In figure 6.2 a particle placed at an interface coupled to a bulk fluid is shown. The flow of the subphase is described by Stokes' equation and the continuity equation:

$$\begin{aligned} \mathbf{f} - \nabla p + \eta \Delta \mathbf{u} &= 0 \\ \nabla \cdot \mathbf{u} &= 0 \end{aligned} \tag{6.3}$$

where $\mathbf{f}$ is an external force, p is the subphase pressure, $\mathbf{u}$ denotes the subphase velocity and

$$\eta(z) = \eta\Theta(-z) \tag{6.4}$$

is the viscosity that equals to η for $z < 0$ in the subphase and vanishes for $z > 0$. $\Theta(z)$ is the Heaviside function.

The interface also fulfills a Stokes equation given by

$$\mathbf{f}_s - \nabla_s \pi_s + \eta_s \Delta_s \mathbf{u}_s + \left|\left| \eta \frac{\partial \mathbf{u}}{\partial z} \right|\right|_s = 0 \qquad for \quad \mathbf{x}_s \in A \tag{6.5}$$

where $\mathbf{f}_s$ is an external surface force parallel to the monolayer surface, π_s is the surface pressure, $\mathbf{u}_s$ is the surface velocity, and ∇_s denotes the surface gradient. The symbol $||C||_s = C(_{z=+0}) - C(_{z=-0})$ denotes the jump in C across the interface.

Since the Marangoni forces are maximal , the flow at the surface may be described by an incompressible flow given by :

$$\nabla_s \cdot \mathbf{u}_s = 0 \qquad for \quad z = 0 \tag{6.6}$$

$$\mathbf{u}_z(z = 0) = 0 \tag{6.7}$$

The approximation of the interface as incompressible is justified since surface compression waves travel with the speed of surface phonons that is much larger than the speed of the object. Hence Marangoni forces are transmitted instantaneously in this approximation. The cause of these Marangoni forces are small surfactant density gradients that drop out of the equations in the limit of vanishing compressibility. The incompressibility of the surface is a well accepted approximation that has been introduced in the work of Saffmann, Hughes [35, 120] and Stone [57]. In the work of Danov, [?, 122] this approximation has been replaced by the condition of a constant surface pressure that neglects the Marangoni forces. The difference of the theory presented here in comparison to the work of Danov [?, 122] therefore is to put the theory of protuding objects into the same framework as the work of Saffmann , Hughes [35, 120] and Stone [57] that treat non-protuding objects at an interface. The boundary conditions at the interface require that the velocity must coincide with the velocity $U\mathbf{e}_x$ of the object (non-slip boundary condition):

$$\mathbf{u} = U\mathbf{e}_x \qquad for \quad \mathbf{x} \in \partial O, \tag{6.8}$$

where ∂O denotes the surface of the sphere that is immersed in the water.

The interface is assumed to be flat and located at the position $z = 0$ and no deformation of the surface by, e.g. electro capillary effects [123, 124] are considered. Such an approximation is reasonable if the viscous drag is small compared to capillary stresses ($\eta U/\sigma_s \ll 1$, U the

speed of the object, σ_s the tension of the monolayer/membrane). The flatness of the interface under such conditions also leads to the effect that rotation of a sphere is strongly suppressed when being immersed into the interface. A rotation of a sphere in a flat interface leads to a divergent stress near the contact line that forbids the rotation of the bead [[125–127]]. Hence no rotation of the bead occurs within the level of this approximation as soon as it touches the interface.

The various parameters on which the friction coefficient depends may be expressed by two dimensionless groups: The 1st group is the Boussinesq number

$$\mathcal{B} = \frac{\eta_s}{\eta a} \tag{6.9}$$

while the second is the ratio of the immersion depth of the bead to the bead radius i.e d/a. The theoretical analysis of Fischer solves the drag coefficient as a power series in the Boussinesq number,

$$f = f^0 + \mathcal{B}.f^{(1)}.$$

. Within an accuracy of 3% the coefficients are found to be

$$f^0 \approx 6\pi\sqrt{\tanh\left[\frac{32(d/a+2)}{9\pi^2}\right]} \tag{6.10}$$

and

$$f^{(1)} \approx \begin{cases} -4 * \ln(\frac{2}{\pi}\arctan(\frac{2}{3}))\frac{a^{3/2}}{(d+3a)^{3/2}} & for \quad d > 0 \\ -4 * \ln(\frac{2}{\pi}\arctan(\frac{d+2a}{3a})) & for \quad d < 0 \end{cases} \tag{6.11}$$

6.4 Discussions

In section 6.3 we found that the mobility of the microspheres decreases with increase in the electrolyte concentration of the bulk water for the 170 nm sized beads but no such effect was seen for the 500 nm beads. For the smaller particles the drag coefficient was found to increase with the electrolyte concentration of the water. As mentioned earlier mobility of a sphere at an interface may be affected by the Marangoni forces, surface viscous effects as well as immersion depth. Since the interface is non-viscous under the present experimental conditions, any contributions from the surface viscous effects are ruled out. The interface may be regarded as incompressible since a absolutely clean surface cannot be realized in

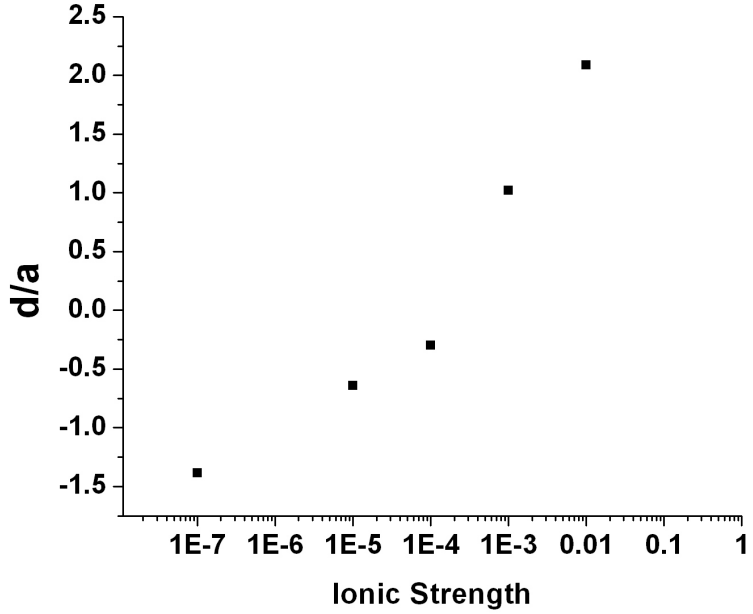

Figure 6.6: The immersion depth of a sphere at an air/water interface as a function of the electrolyte concentration of the bulk reservoir.

the presence of tracer particles, due to experimental limitations of cleaning. As a result the incompressibility of the interface implies that the Marangoni forces acting on the sphere at the interface are maximum. Under these circumstances the change in the mobility of the sphere may only be attributed to a change in the immersion depth of the sphere at the interface.

Therefore, assuming an incompressible interface, the single particle theory of Fischer et.al [112] outlined in section 6.3.1 may be used and the immersion depth calculated using equation 6.10. The immersion depths are plotted as a function of the electrolyte concentration in Figure 6.6.

The carboxylate modified spheres when placed in water have a net negative surface charge. The $COOH$ on the sphere dissociates into COO^- and H^+ in water such that there is a net negative charge on the surface of the spheres. Since there is a strong dependence

of the diffusion constant of the beads (for the spheres with smaller radius (170 nm)) on the electrolyte concentration, electrostatic forces may be regarded as a strong contributor to the forces on the sphere at the interface.

However, the absence of any effect of the salinity of the water on the diffusion constant of the larger sphere (500 nm) suggests that the size of the sphere may also be an important factor. The data of the 500 nm beads is in agreement with the results of Danov et.al [124] who found electrodipping effects to be independent of salt concentrations in case of large beads (radius = 200 to 300 microns).

An attractive interaction between colloid particles in a water/air interface was first measured by Nicolaides and Weitz [123]. According to them the normal force acting on a particle at an interface is of electrostatic (rather than gravitational) origin. A strong contrast in the electrostatic properties of the bead and the air/water would be enough to push the colloidal particles into the subphase. This normal electrostatic force was termed electrodipping by Danov, [124]. Although attractive interactions between interfacial beads have been attributed to these electrodipping effects by other groups the exact cause of the interaction is controversial to date. Our results suggest that the electrostatic forces and the size of the particle may both contribute to the geometric arrangement of a sphere at an interface. A change in the electrostatic forces (electrodipping) by changing the electrolyte concentration would alter the immersion depth of the sphere. Considering the distribution of the negative charges on the sphere one would expect that the addition of salt would screen the electrostatic charges on the sphere resulting in a decrease in the electric forces on the sphere. This would cause the spheres to pop out of the interface. Our experimental results, however, are contrary to this expectation since we find that the addition of salt causes the spheres to be more deeply immersed in the bulk water. While it is evident from the results that the electrostatic charges contribute to the immersion depth of a sphere at a monolayer the electrodipping theory in its present form cannot explain the dipping direction obtained in the figure 6.6. For a more complete analysis, one would be required to further investigate this phenomemon. Experiments involving beads of different sizes would indicate a clearer dependence on the bead size. Microspheres with opposite charges would need to be investigated to analyze the influence of the contrast between the electric dipoles of the water and the beads. Further, surface potential measurements of the water and beads need to be done for various electrolyte concentration for a clear understanding of this phenomenon.

6.5 Summary and Conclusions

In this chapter we investigated the effects of electrostatic interactions on charged beads at an air/liquid interface. To enable us to study the pure electrostatic effects, a bare air/water interface was used. The electrostatic forces are altered by changing the electrolyte concentration of the bulk water reservoir. Further two different sized spheres with similar charges were used for the experiments. It was already known from a theory of Nikolaides et al. [123] that electrostatic forces might be significant for spheres at an interface. The mobility of carboxylate modified spheres of two different sizes (170 nm and 500 nm) were analyzed for five different salt concentrations of the bulk water using a single particle tracking program. Applying a modified Stokes- Einstein formula to convert the measured MSD into a drag coefficient. We found that the drag coefficient of the smaller spheres increased with increasing salt concentration. This effect was absent for the larger spheres (500 nm diameter) in compliance with experimental observations of Danov et al. who used even larger spheres (200-300 microns). Since the mobility of the sphere may only depend on the viscous forces at the interface or the immersion depth, the absence of surface shear viscosity points towards a change in the immersion depth. The change of immersion depth depends on the electrolyte concentration of the bulk water, suggesting that the reason for it lies in electrostatic forces. The larger beads did not show a similar dependence on the electrolyte concentration suggesting that the ratio between the Debye length and size of the particles need to be significantly higher for the electrostatic effects to be effective. Although, one can claim that the change in the drag coefficient is due to electrostatic effects, present theories fail to explain the direction of the change. An improved theory would require considering the contrast in the surface potentials at the interface and relate it to a change in the electrostatic interactions at the interface. Therefore, further analysis, taking these interactions into account need to be done. This effect is, however, significant when considering the motion of nanomotors at interfaces. It is of special relevance in biology where the membranes are surrounding by water, ions (Na^+ , K^+) and other molecules. Electrostatic effects become significant for the mobility of molecular motors at interfaces where the size of the nanomotor may be orders of magnitude smaller than the Debye length of the surrounding medium.

CHAPTER 7

Materials and Methods

In this chapter we outline the details of the procedures necessary to perform the experiments described in the previous chapters. The steps involved in the preparation of the interfaces and the active components are described. The culture techniques of the biological active components are described in details. We have also outlined some of the imaging techniques used to view the active components at the interface. Some of the steps involved in the preparation are common to more than one experiment, as indicated, while there are some steps that are unique to one experiment. These differences have also been highlighted in this chapter.

7.1 Autonomously Moving Nanorods

7.1.1 Extraction of the rods from the alumina template

The bimetallic Platinum Gold nanorods are synthesized by the group of Ayusman Sen and Thomas Mollouk at Pennsylvania State University. The metals were electrochemically deposited into the pores of Anopore alumina membranes. The different metals were plated sequentially to obtained striped nanorods. A more detailed description may be found in ref [39]. To extract these rods from the alumina template we undertook the following steps

1. The membrane was kept in 5M nitric acid for 5 minutes, making sure that the template was completely submerged in the acid.

2. It was then washed thoroughly with deionized water.

3. The washed membrane was dropped into a solution of 5M NaOH solution. It was left for 30 minutes till the membrane completely dissolved.

4. The solution was transferred to a acid cleaned test tube and centrifuged and sonicated till a neutral pH was obtained.

7.1.2 Rods at liquid/liquid interface

For the experiments described in chapter 2, to disperse the rods in the methanol solution, the following steps were followed.

1. About 500 ml of the solution was placed in a dialysis tube which was floating on methanol placed in a beaker. It was left like this for about half an hour after which the rod solution in methanol was pipetted out from the dialysis tube.

7.1.3 Metallic Nanorods

The metallic nanorods, studied in chapter 3 and chapter 4, were prepared similarly where platinum, nickel and gold were sequentially plated electrochemically into the alumina membrane pores. The same steps of extraction was also followed as for the platinum/gold

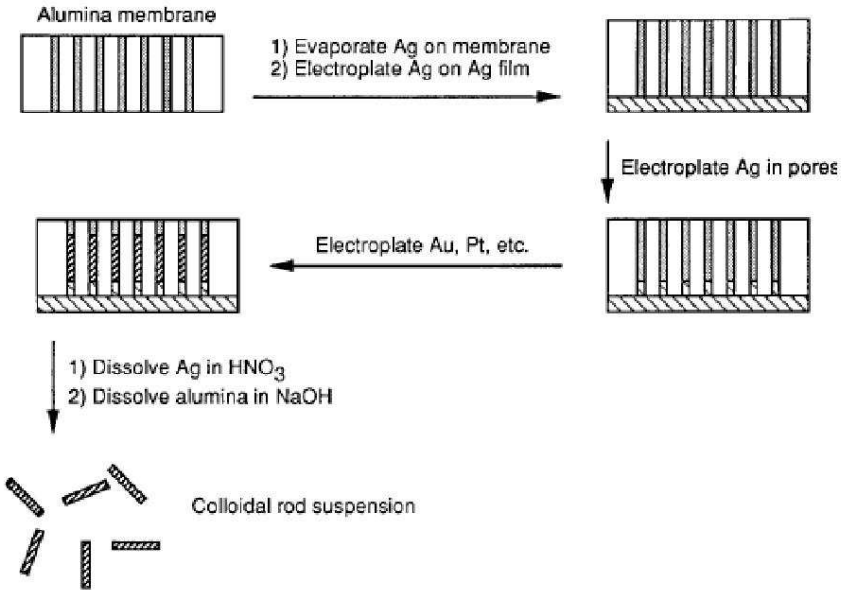

Figure 7.1: Schematic of the synthesis and extraction of the Pt/Au nanorods

rods. However, in step 4, instead of sonication the rods were dispersed in the media by vortexing gently.

7.2 Surfactants at Air/Water and Decane/Water Interface

Before spreading a monolayer at an air/water interface the following steps were always taken into account. These steps were followed for the experiments described in chapters 2 and 6.

7.2.1 Trough cleaning

To clean the Langmuir trough

1. The trough was filled with water and allowed to sit for about 5 minutes.
2. The water was then slowly sucked out using a suction mechanism keeping the suction pipette close to the surface. The suction was continued until all the water has been removed.
3. Step 1 and 2 were repeated a few times.
4. Kimwipes wet with Chloroform were then used to wipe down the trough thoroughly a couple of times.

All of the above steps were repeated a few times until the interface appeared to be clean. A good test used to check for a relatively clean surface was the formation of spherical droplets of water at the surface.

7.2.2 DPPC and SDS

To prepare 1mM solution of DPPC the following steps were followed:

1. 0.0074 g = 0.7 mg of DPPC powder was measured out into a previously clean and dry glass bottle.
2. 10 ml of 99.9% pure chloroform was added to this bottle and the contents swirled till a clear solution was obtained.
3. 300 to 500 μl of the dye solution was added to this solution. If a dye powder was being used then about 0.0007 gms of the dye was used.

4. This solution was allowed to sit for about 20 minutes before it was ready to be stored or used.

DPPC solution was always stored in the freezer if not being used immediately. If reusing a solution, the DPPC was allowed to sit at room temperature for a while (until it achieved room temperature) before it was used for spreading. To spread the DPPC first the volume of DPPC solution required to obtain a particular area per molecule was calculated using the formula

$$V = (b \times l)/(6.023 \times 10^{20} \times 1 \times area/molecule)ml$$

This volume was then carefully spread on the interface.

To prepare 0.25 M solution of SDS :

1. 0.72095 grams of SDS powder was measured out into a previously clean and dry glass bottle.

2. 10 ml of water was added to this bottle and the contents swirled till a clear solution is obtained.

3. This solution was allowed to sit for about 20 minutes before it was ready to be stored/used.

SDS may be stored at room temperature. The volume of SDS to be added was calculated stoichiometrically using the relation

$$m_f v_f = m_s v_s$$

where m_f is the final concentration in moles, v_f is the total final volume, v_i is the initial volume of the stock and m_s is the concentration of the stock solution. Therefore, the volume of the stock solution to be added was

$$v_s = m_f v_f / m_s ml$$

.

7.2.3 The Spreading

The DPPC was spread on the air/water interface. About 5ml of water was added to the trough such that it rose to the notch in the barrier height in the Langmuir trough. The volume of DPPC required for a desired area/molecule was then spread at this interface.

For the liquid/liquid interface used in Chapter 2, the following was done:

1. Approximately 5 ml of 3.5 % solution of the aqueous hydrogen peroxide was taken in the trough.

2. 400 μl of the methanol solution of the rods was spread on the surface and the methanol was allowed to evaporate.

3. After 15 to 20 minutes, 10 ml of decane is added to it.

The interface between the aqueous solution and decane formed the bare liquid/liquid interface. To change the surface viscosity at this interface various volumes of SDS were added into the aqueous solution to get the desired concentration of the Gibbs monolayer. After the addition of each volume, the experiment was allowed to sit for 45 minutes to allow the equilibrium amount of the SDS to come to the interface. After waiting for 45 minutes the interface was imaged by using a 100x oil immersion microscope. We ensured that we were focusing on the interface by either moving into or out of the plane at which point the rods disappeared. The fact that the rods were not in the bulk was also ensured by this method. At the same time the depth to which the lens was immersed in the trough confirmed that the rods were not present at the bottom of the trough. All this led us to the conclusion that the rods were indeed spread at only one plane, at the interface between the two liquids.

7.3 Beads at the Air/Water Interface

For the experiments involving the microspheres at the air/water interface, the following steps were followed.

7.3.1 Cleaning the beads

1. Carboxylate modified fluorescent microspheres of diameter 170 nm (MS Spec Kit) were bought from Molecular Probes.
2. The beads were sonicated for 5 minutes to get rid of any agglomeration.
3. 1 ml of the bead solution was passed through a column of ion-exchange resin bed which was prepared by packing a glass pipette with the resin-bed and collected in a clean glass bottle.
4. The collected clean solution of the beads was sonicated again for 10 minutes.
5. 200 μl of this bead solution was dissolved in 800 ml of isopropanol and sonicated again.

The solution of the bead in isopropanol was then ready to be used for the experiment.

7.3.2 Spreading

To spread the beads at the air water interface:

1. 200 μl of the bead in isopropanol solution was carefully added dropwise (5 μl at a time) such that the solution can be seen spreading on the surface and not sinking into the water.
2. After spreading the beads, the isopropanol was allowed to evaporate by waiting for 45 minutes before performing the experiments

To observe the fluorescent microspheres, a LEICA fluorescence microscope with Texas Red filter was used. Movies of the diffusion of the spheres were recorded with a WinTV software and were digitized later for analysis.

In all experiments involving the air/water interface, the thermal convection at the interface was significantly reduced by covering the microscope with a plastic sheet.

7.4 Preparing for Experiments using the Magnetic Garnet Films

7.4.1 Preparing the PSS solution

To prepare the solution of PSS for coating the magnetic film with a thin layer of negative charges the following procedure was followed:

1. 5 mg of poly sodium 4-styrene sulfonate (PSS) was dissolved in 1 ml of ultrapure water placed in a tube.
2. 0.029 g of NaCl (0.5 M) was added to the solution.
3. The cap of the bottle was sealed and stored.

7.4.2 Cleaning the Magnetic Garnet Film

The garnet films are cleaned using the following steps.

1. The garnet piece that needed cleaning was placed into a tube containing ultrapure water and sonicated for 10 minutes.
2. The water was replaced by 1N HCl and sonicated again 10 minutes.
3. The HCl was discarded and the garnet washed with ultrapure water a few times to ensure that no acid remained.
4. Step 1 was repeated.
5. The water was replaced by 1M NaOH and sonicated for 10 minutes.
6. The NaOH was discarded and the film washed with ultrapure water a few times to ensure that no base remained.
7. Step 1 was repeated.
8. The water was discarded and the garnet film was gently wiped with a wet KIMwipe.

7.4.3 Coating with PSS.

The garnet is then ready to be treated to make the surface more negative. For doing this we followed the steps described below.

1. The garnet film was dropped vertically into a tube containing a solution of PSS as described in 7.4.1 and sonicated for 5 minutes.

2. The solution was sucked out to let as little of the liquid to remain as possible.

3. The garnet film was taken out of the tube and held vertical on a KIMwipe to let any remaining liquid to drain off.

7.4.4 Correct side up

To be able to perform the experiments described in chapters 3 and 5 we need to ensure that the correct side (the side containing the film) is facing up. To ensure this we did the following

1. The film was placed on the polarization microscope stage such that one of the edges of the garnet film is in the field of view.

2. The focusing was adjusted to focus on the first surface that we encountered.

3. If we encountered the stripe pattern first instead of a plane surface then we knew that we had the correct side. Else the film was flipped over and the above steps repeated.

7.5 Magnetotactic Bacteria

The magnetotactic bacteria were cultured by Priya Pal, an undergraduate student in Brian Miller's group at Florida State University and by me. The microorganisms were initially obtained from DSMZ Deutsche Sammlung von Mikroorganismen und Zellkulturen GmbH. To culture the cells in the lab, the protocol described in [74] was followed. The steps undertaken are described below.

7.5.1 Preparation of the media

1. The media was made up by adding the materials listed below to 100 ml of deionized water at pH 7 in a conical flask and the contents stirred using a magnetic stirrer.

KH_2PO_4	0.01 g
$MgSO_4.7H_2O$	0.015 g
HEPES	0.238 g
Yeast extract	0.01 g
Soy bean peptone	0.3 g
EDTA chelated trace element mix [74]	100 μ l
Na^+ Lactate	.3025 g
$NaNO_3$	0.034 g
Fe(III)Citrate	0.00245 g

Table 7.1: Composition of the materials/salts used to make up the culture media for the magnetotactic bacteria are listed.

2. After the materials went into solution 15 ml aliquots of the media were placed in 5 Hungate tubes such that about 20 % of the tube volume was empty. This was done to ensure the correct percentage of oxygen required for the best growth conditions for the bacteria.

3. The caps on the tubes were sealed and the tubes autoclaved.

4. The tubes were removed from the autoclave, cooled and then stored at room temperature on a bench rack.

7.5.2 Propagating Bacteria Cultures

The bacteria were cultured as follows

1. 100 μl of the original saturated culture stock was placed in one of the previously prepared Hungate tubes by puncturing the rubber seal with a syringe.

2. This tube was then placed in an incubator at 27^0 C for three days.

3. The appearance of a cloudy culture solution suggested that it was saturated. At this point it was taken over to the Fischer lab for the experiments described in 3

4. This process was repeated every three days to allow the bacteria to grow continuously. Fresh cultures were always used for the experiments since the bacteria are healthiest as they approach or when they have just reached saturation.

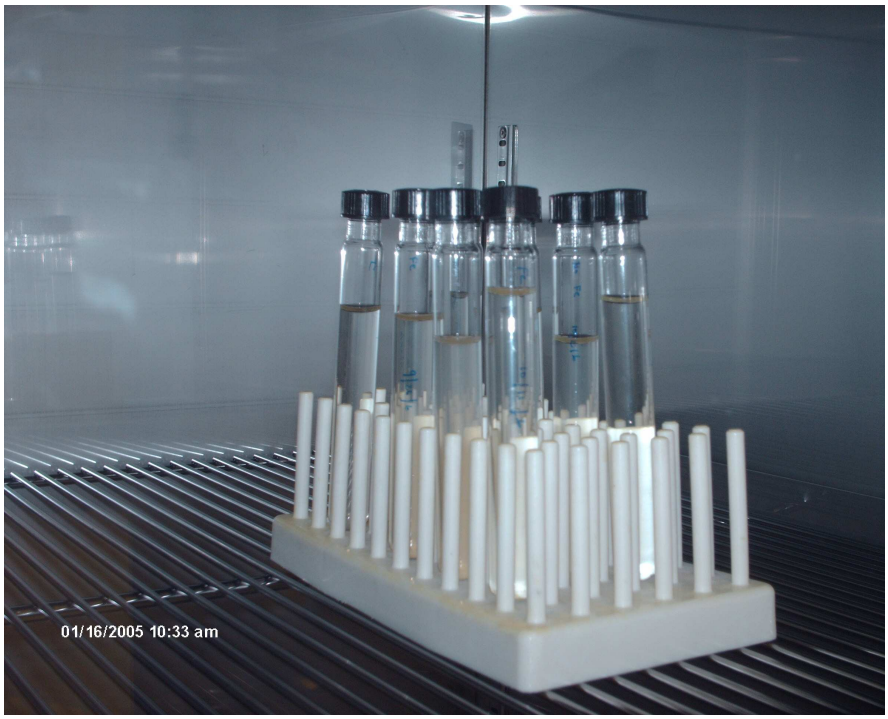

Figure 7.2: Image of the Hungate tubes containing the bacteria inside the incubator. Note the level of the culture media in the tube is almost three/fourths full to maintain the oxygen content desirable for the growth of the bacteria.

7.6 Cell Culture

Since we started a new cell line of mouse macrophages, Pixie 12j, it involved growing the cells following the protocols described below before we had the cells growing normally in culture.

7.6.1 Preparation of JMEM

2 Liters of JMEM or Medium Essential Media Eagle (Joklik's Modification) was prepared as follows.

1. The glass distilled water system was started ahead of starting to make the media and 2 liters of water was collected in the conical flask and allowed to cool by placing on ice.
2. Once the water had cooled enough, a washed and cleaned round bottom flask was placed on a magnetic stirrer plate and a magnetic stirrer dropped into it.
3. The flask was filled with 1 l of the freshly prepared glass distilled water to which two bottles of the free flowing JMEM powder was added through a funnel. The bottles were rinsed out with the glass distilled water and all the powder sticking to the neck of the flask was also washed out into solution.
4. The magnetic stirrer was started to stir the solution until all the powder went into solution.
5. At this point a yellow coloured solution was obtained.
6. 2 g/l $\times 2l = 4$g of sodium carbonate was measured out and added to the flask and the rest of the water added to make up a total volume of $2l$.
7. The magnetic stirrer continued to stir the solution until all the powder dissolved. At this point the color of the solution changed from yellow to pink.
8. Once it was clear that all the powder had gone into solution, four 500 ml bottles, the solution, and a filter were moved to the biosafety cabinet.
9. The media was filter sterilized in the biosafety cabinet using a 500 ml Sarstat filter via vacuum into the 4 bottles.

10. All four bottles were labeled.

11. Tests were drawn from all 4 bottles into 4 T25 flasks and each labeled.

12. The bottles were flamed, closed, and placed in the refrigerator for storage.

13. The T25s were placed in the incubator at 37^0 C and tested from time to time over a period of two weeks to check for any contamination.

7.6.2 Starting the cell line

Product Information sheet for CRL 2449 was used as a guideline to handle the cells. Since the cells arrived in the frozen state to insure the highest level of viability, the culture was initiated immediately. Proper safety gloves and clothing were worn and as much as possible most of the work was done in the hood. The steps undertaken were as follows.

1. The heat enactive calf serum was set aside to thaw by placing in a beaker containing tap water ensuring that the top of the bottle was above the water level.

2. The biosafety cabinet was wiped down with 70 % ethanol.

3. The antibody/antigen (AB/AM) mixture was allowed to thaw by placing in the biosafety cabinet.

4. After the serum and AB/AM had thawed, the JMEM (7.6.1) was made up further by addition of 50 ml of serum, 5 ml of Ab/Am and 0.5 ml of Gentamycin. Before opening and after closing, each bottle was flamed.

5. 25 ml of this JMEM media in a T75 flask was placed in the 37^0 C incubator and warmed to the desired temperature for growth.

6. The vial containing the cell line was thawed quickly but carefully by gentle agitation in a 37^0 water bath for about 2 minutes.

7. As soon as the contents of the vial had thawed, it was removed from the water bath and decontaminated by spraying with 70 % ethanol and placed in the biosafety cabinet.

8. The T75 flask containing the 25 ml of media was removed from the incubator, opened and flamed and the contents of the vial were immediately transferred to the T75 flask.

9. The T75 flask was closed and flamed again.

10. The cells were watched under the microscope.

11. The rounded shape of the cells suggested that they were alive and were hence placed in the 37^0 incubator with a 5 % CO_2 in the air atmosphere. The cap of the flask was closed loosely to allow the passage of air. The cells were placed on a rocker to prevent attaching.

7.6.3 Subculturing procedure

To let the cell line to continue to thrive in culture, the following was done.

1. After 24 hours the T75 flask was removed from the incubator, the cap tightened and placed on the microscope to check the appearance of the cells.

2. The cells were counted by pipetting out 100 μl from the original cell culture after gently shaking to ensure that the cells are uniformly dispersed.

3. After counting the cells in 3 boxes in the Hemacytometer, the average was calculated and agreed upon as the number of cells per liter of medium.

7.6.4 Medium Renewal

To renew the medium, a calculated amount of the fresh warmed media was replaced by the original medium. The calculation was done such that after adding the fresh medium we always had a starting culture of 4.5×10^5 cells/ml. For example, suppose we found that there were 9.0×10^5 cells/ml in the media, and we would like to bring the cell count down to around 4.5×10^5 cells/ml. So we would need

$$(9.0 \times 10^5 \times 25) \div (4.5 \times 10^5) = 12.5ml$$

of fresh media. We discarded 12.5 ml of the original media, put back 12.5 ml of the fresh media and then placed the T25 flask back on the rocker in the incubator. The cells were counted and medium was renewed everyday to allow for the best growth conditions.

7.6.5 Ferrofluid ingestion

To allow the macrophages to phagocytize the ferrofluid the following steps were undertaken:

1. Before renewing the media in the T25 flask, 1 ml of the culture was placed in a Petri dish

2. 100 μl ferrofluid containing 5-50nm sized Fe_3O_4 particles were added to the Petri dish with 1 ml of fresh media and placed back in the incubator.

3. After 48 hours the culture dish was removed and viewed under a microscope. 90 % of the cells were found to have adhered to the dish and the magnetic particles had been phagocytized.

4. The medium was removed carefully by sucking out with a pipette.

5. 1 ml of 1-x trypsin was added, allowed to sit for 30 seconds and then replaced with 2 ml of fresh media.

6. The cells were mechanically detached from the surface by repeated forceful expulsion of media at a 45^0 angle to the dish surface with a narrow-tip transfer pipette.

7. The Petri dish was viewed under the microscope to ensure that most cells had been detached before they were walked over to the microscope in the Fischer Lab.

CHAPTER 8

Summary

The need for motion is of topmost priority in nature. Organisms need to be able to transport themselves towards food and away from predators. Life, in general, can only be sustained by a constant influx of energy, material and entropy on various scales. Material fluxes occur due to either passive or active transport. Passive transport is a form of transport where the material to be transported does not move on its own, but is advected by its surroundings. Passive transport is encountered on the macroscopic scale for example in jelly fish that uses the current in the sea to be advected toward its prey. It also appears on smaller scales down to the micron scale in the form of transport of nutritients, oxygen and proteins in our blood. On even smaller scales passive transport no longer is a efficient way of motion. Hydrodynamic friction, Brownian fluctuations and other forms of dissipation make it increasingly difficult to achieve a directed motion from one position to another. Nature has solved this problem by switching to active forms of transport. A rich variety of motor proteins are responsible for cell trafficking on the nanometer to micrometer scale. These motors are able to overcome fluctuations in the environment that usually would randomize their direction of motion.

In technology we often try to use solutions that are borrowed from nature that have been perfected due to evolutionary optimization over millions of years. A significant part of current research efforts are directed toward the fabrication of microfluidic devices that are little chemical labs of the size of a credit card. In these devices (commonly referred to as lab-on-chip)specific materials are transported via advection through microfluidic channels to detection systems where the analytes are detected (for example certain diseases maybe detected by analysing a blood sample). Of course scientists have borrowed solutions from nature also in creating such devices. It is therefore not suprising that the choice of transport

in such devices is a passive form of motion. As the race for miniaturization continues, lab-on-the-chips of smaller sizes but with more specific functionalities are seeked upon. However, upon miniaturization technology encounters the same difficulties associated with passive transport as encountered in nature. It is therefore clear that developing technology relies on the use of active transport for more efficient functioning of the devices.

This dissertation aims at laying some foundations for the understanding of the motion of active components. We try to understand the strategies required to be adopted to achieve guided motion in a dissipative, fluctuating and heterogeneous surrounding. Some of the important questions associated with active transport are:

- The function of the motor. Nanomotors are powered by an energy source,where the ideal fuel should not involve the generation of any waste productts or damage to the motor. As a result one of the common choices of fuel is of chemical origin. The Gibbs free energy released in a chemical reaction needs to be converted into mechanical energy. Chemical reactions usually occur on a very local scale, where things are isotropic. A priori chemical reactions usually do not have a preferred spatial direction. The conversion of the chemical energy into a directed motion is a typical problem of chemical engineering. We have to consider the coupling of the chemistry to the hydrodynamic flows that the chemical reactions are accompanied with. Smart ways of synergetic activity of chemistry and hydrodynamics are needed to achieve a functioning motor.

- Once we have designed a forward propelling motor we still need to guide it by laying out some track to follow. Fluctuations from the surroundings will try to randomize the motion. Therefore , strategies of confining the motor motion to its track, strong enough to overcome these fluctuations, are needed.

- The efficiency of the motors can be increased, if a part of the environmental fluctuations could be converted into directed motion. The laws of thermodynamics apply to our motors and hence it is impossible to convert thermal equilibrium fluctuations into something more ordered like the directed motion. However, if the fluctuations differ from equilibrium fluctuations we might try to use at least the non-equilibrium part of those fluctuations to our advantage and convert it into a directed motion.

- The heterogeneity of the environment leads to complex questions of the geometric arrangement of the motors with respect to these heterogeneities. Often the electrostatic contrast associated with the heterogeneities leads to complex interactions of the motor with the electrostatic fields. For a proper understanding of the motor motion geometric arrangements on the nanometer scale need to be determined.

We tried to address these major questions with this dissertation by studying several model systems. The question of the motor function is addressed in chapter 2, while strategies for the guidance of the motors were studied in chapter 3. Some examples how to use fluctuations and dissipation to orient and guide active components were addressed in chapters 4 and 5. Finally in chapter 6 we showed how the fluctuating motion can be used to learn about the geometric arrangement of our moving components.

Our model air/liquid and liquid/liquid interfaces have a Gibbs monolayer on an aqueous solution and platinum-gold nanorods and fluorescent beads are incorporated into the interface. The design of these components is such that they have a size much smaller than the Boussinesq length (l_B) of the system under study. Fluctuations are able to confine and guide some of these components at interfaces while nonequilibrium fluctuations can also induce directed motion in some biological components.

Our 1st project aimed at using the hydrodynamic rules to understand (a) what decides the direction of motion of the active component, (b)what is the correlation between the velocity of the active components and the rheological properties of the surrounding interfaces, (c)how to use active components to measure rheological properties of biologically relevant interfaces? The bimetallic nanorods were placed at the liquid-liquid interface(decane on aqueous solution of 5% hydrogen peroxide) and the surface properties of the interface were altered by using various concentrations of sodium dodecyl sulphate SDS. The rods moved at the interface due to the catalytic activity of the rods on the hydrogen peroxide aqueous subphase. Detailed analysis of the motion of the rods revealed a cross over from ballistic motion to normal diffusive motion at Boussinesq number $\mathcal{B} \approx 1$. It was then concluded that the direction of motion was caused by a *hydrodynamic friction asymmetry* and the rods tend to move in the direction of lower hydrodynamic friction. The fact that the cross over happens in the region of Boussinesq number $\mathcal{B} \approx 1$ supports this theory since the addition of rigid surfactant layer of the size of the Boussinesq length restores the symmetry of the

friction when the Boussinesq length exceeds the length of the rod. At the same time these rods were used as microscopic needle rheometers to calculate the surface viscosity of the interface with greater precision.

In chapter 3 we studied the response of a magnetotactic bacteria to heterogeneous magnetic fields on the colloidal scale produced by magnetic garnet films and found that the bacteria perform a dynamically frustrated guided motion. The response of the bacteria to the field was then used for strategies to design different synthetic nanorods to achieve guided motion along a particular path. We found that best guidance was achieved for paramagnetic nanorods, not for ferromagnetic rods. An interplay of the propulsion energy and magnetic energy contributed to the success or failure to achieve absolute guidance of the active components.

The viscous dissipation into the fluid environment was used to orient transversely magnetized rods when placed in a precessing magnetic field. We found that depending on the magnitude of the magnetic torque, the viscous torque and the friction, the rods would undergo a reorientation from horizontally laying in the plane to a vertical orientation where the rods rotate around their long axis. The precession frequency and the strength of the magnetic field are the important control parameters that decide on the orientation of the rods.

We use non equilibrium fluctuations and a pulsating magnetic ratchet potential to induce directed motion in magnetically labeled mouse macrophages. Ferrofluid ingested mouse macrophages were placed on a magnetic garnet film and an oscillating external magnetic field was applied normal to the film. It was proved both experimentally and theoretically that we could induce directed motion in the macrophages if the curvature of the stripe pattern in the film where the macrophages were located was above a certain minimum value.

In the last chapter we study the effects of electrostatic interactions on charged beads at an air/liquid interface. According to a theory of Nikolaides one would expect to see a change in the immersion depth of a bead at an interface due to electrostatic forces. We studied the Brownian diffusion of charged beads to probe their protrusion into an air/water interface. The mobility of carboxylate modified spheres of two different sizes (170 nm and 500 nm) were analyzed for five different salt concentrations of the bulk water using a single particle tracking program. Applying a modified Stokes- Einstein formula, the measured mean square displacement was converted into a drag coefficient. We found that the drag coefficient of the

smaller spheres increased with increasing salt concentration. This effect was absent for the larger spheres (500 nm diameter) in compliance with experimental observations of Danov et al. who used even larger spheres (200-300 microns). Since the mobility of the sphere only depends on the viscous forces at the interface or the immersion depth, the absence of surface shear viscosity points towards a change in the immersion depth. The change of immersion depth depends on the electrolyte concentration of the bulk water, suggesting that the reason for it lies in electrostatic forces. Although, one can claim that the change in the drag coefficient is due to electrostatic effects, present theories fail to explain the direction of the change. An improved theory would require considering the contrast in the surface potentials at the interface and relate it to a change in the electrostatic interactions at the interface. Therefore, further analysis, taking these interactions into account need to be done for further understanding of the observations.

APPENDIX A

Fundamentals

In this Appendix I would like to outline some fundamentals which I feel are important background to understand the principles dominating some of the effects described in this dissertation.

A.1 Behavior of Fluids in Slow Motions

Here we derive the equations of creeping flow. We start with the equation of continuity which maybe obtained by applying the law of conservation of mass to a small stationary volume element within a flowing fluid:

$$\partial\rho/\partial t = -(\nabla \cdot (\rho \mathbf{v})) \tag{A.1}$$

where ρ is the local density, $\mathbf{v}$ is the local mass average fluid velocity, $(\rho\mathbf{v})$ = rate of mass efflux per unit volume.

Incompressible fluids have a constant density, such that $\partial\rho/\partial t = 0$ and the equation of continuity simplifies to

$$\nabla \cdot \mathbf{v} = 0 \tag{A.2}$$

Further the equation of Linear Momentum for a continuous fluid may be written as

$$\underbrace{\partial(\rho\mathbf{v})/\partial t}_{rate of increase of momentum per unit vol} + \underbrace{\nabla \cdot (\rho\mathbf{v}\mathbf{v})}_{rate of momentum loss of convection, per unit volume} = \underbrace{\nabla \cdot \Pi}_{stress on the surface per unit volume} + ext \tag{A.3}$$

The left hand side of the equation is the rate of creation of momentum per unit volume while the right hand side denotes the external forces per unit volume. The pressure or stress tensor Π, is a 2^{nd} rank tensor such that if dS is a directed element of surface area, then $dS.\Pi$ is the contact force exerted by a fluid on a directed element of surface area dS. Rewriting equation A.3,

$$\rho(\partial/\partial t + \mathbf{v} \cdot \nabla)\mathbf{v} = \nabla \cdot \Pi + \rho F \tag{A.4}$$

In order to use these equations of motion for any continuous fluid, it is necessary to express the pressure tensor in terms of measurable pressures and velocities. The theory of Newtonian fluids leads to the following relation:

$$\Pi = -pI + \kappa(\nabla \cdot \mathbf{v})I + 2\mu\Delta \tag{A.5}$$

where:

p - is the hydrostatic pressure the fluid would be supporting if it were at rest at its local density and temperature T.

I - is the unit tensor δ_{ij}

κ - is the bulk or volume viscosity

μ - is the shear viscosity

$\mathbf{\Delta}$ - is the rate of deformation given by $= 1/2\left[\nabla v + (\nabla v)^T\right] - 1/3\mathbf{I}(\nabla \cdot v)$

Therefore for incompressible fluids, substituting A.5 into A.4 we find

$$\rho(\partial/\partial t + v \cdot \nabla)\mathbf{v} = -\nabla p + \mu\nabla^2\mathbf{v} + \rho\mathbf{F} \tag{A.6}$$

This is the ***Navier Stokes equation***.

Omission of the inertial terms compared to viscous terms in equation A.6 leads to :

$$\mu\nabla^2\mathbf{v} = \nabla p$$

which together with the equation of continuity

$$\nabla \cdot \mathbf{v} = 0$$

constitutes the ***Creeping Flow Equations***

A.2 Surface Torque on a Rotating Rod

The surface torque on a rotating rod of vanishing diameter arises from Marangoni and surface viscous effects only. The surface velocity is related the force density $\tau(x')$ via

$$\mathbf{u_s}(\mathbf{x}) = \int_P \mathbf{O}(\mathbf{x} - \mathbf{x}') \cdot \tau(x') \tag{A.7}$$

where P is the perimeter of the rods. $O(x-x')$ is the Oseen tensor, which is a point force solution to the Stokes equation. The transverse component of the Oseen tensor is given by

$$O_{\parallel}(\mathbf{r}_s) = \frac{1}{4(\eta_1+\eta_2)} \frac{d}{dr} \left\{ \mathbf{H}_1\left(\frac{r}{\mathcal{B}l}\right) - N_1\left(\frac{r}{\mathcal{B}l}\right) - \frac{2\mathcal{B}l}{\pi r} \right\} \tag{A.8}$$

r is the distance between the location of the force and the location of the velocity, $\mathcal{B} = \eta_s/(\eta_1+\eta_2)l$ is the Bousinesq number. $\mathbf{H_1}$ denotes the Struve function of order 1 and N_1 is a Bessel function of the second kind and order 1. We set the x coordinate in the interface perpendicular to the rod and the y coordinate is parallel to the rod. The distance r between the force excerted from the rod at one location and the resulting velocity of the fluid at another location on the rod is then given simply by $r = |y - y'|$. The requirement that the rod should rotate with angular velocity ω leads to the condition

$$\mathbf{u_s}(\mathbf{y}) = \omega y \mathbf{e}_x \qquad -l/2 < y < l/2 \tag{A.9}$$

Equations A.8 and A.9 define an integral equation for the force density $\tau(y)$. In the limit $\mathcal{B} \to 0$, $\mathcal{B} \to \infty$, the Oseen tensor may be written as

$$\lim_{\mathcal{B}\to 0} O_{\parallel}(|y-y'|) = \frac{1}{(\eta_1+\eta_2)\pi}\delta(y-y') \lim_{\mathcal{B}\to\infty} O_{\parallel}(|y-y'|) = \frac{1}{4(\eta_1+\eta_2)}[\ln\frac{|y-y'|}{2\mathcal{B}l} + \gamma + 1/2] \tag{A.10}$$

where $\delta(y-y')$ denotes the Dirac delta function and $\gamma = 0.5772$ is the Euler's number.

The analytical solutions to the force profile are

$$\lim_{\mathcal{B}\to 0} \tau(y') = \frac{12T_s y'}{l^3} \qquad , \lim_{\mathcal{B}\to\infty} \tau(y') = \frac{8T_s}{\pi l^2} \frac{y'}{\sqrt{l^2/4 - y^2}} \tag{A.11}$$

where T_s is the torque from the surface. This torque is then proportional to the angular velocity and is given by

$$T_s = (\eta_1+\eta_2)\omega l^3 f_s(\mathcal{B}) \tag{A.12}$$

where $f_s(\mathcal{B})$ is the dimensionless friction coefficient. Inserting the solutions A.11 into A.7 with the asymptotic Oseen tensors A.10 and comparison with the equation A.12 then yields

$$\lim_{\mathcal{B}\to 0} f_s(\mathcal{B}) = \pi/12 \qquad , \lim_{\mathcal{B}\to\infty} f_s(\mathcal{B}) = \pi/4\mathcal{B} \tag{A.13}$$

A.3 Mathematical Basis of the Ratchet Effect

A Brownian particle in one dimension may be described by the equation of motion [111] given by :

$$m\ddot{x}(t) + V'(x(t)) = -\eta\dot{x}(t) + \xi(t) \tag{A.14}$$

where V(x) is a periodic potential with period L,

$$V(x + L) = V(x)$$

The periodic potential exhibits a broken spatial symmetry which has a typical form given by [111]

$$V(x) = V_0[\sin(2\pi x/L) + 0.25\sin(4\pi x/L)] \tag{A.15}$$

while the fluctuations $\xi(t)$ satisfy the fluctuation dissipation relation

$$\langle \xi(t)\xi(s) \rangle = 2\eta k_B T\delta(t - s) \tag{A.16}$$

such that the noise is uncorrelated in time and

$$\langle \xi(t) \rangle = 0$$

Since viscous forces dominate over inertia, the inertia maybe neglected and the fluctuation dynamics is governed by an overdamped Langevin dynamics [128]. This leads to the *minimum equilibrium ratchet model*:

$$\eta\dot{x}(t) = -V'(x(t)) + \xi(t) \tag{A.17}$$

which leads to an average particle current

$$\langle \dot{x}(t) \rangle = 0$$

.

Therefore an additional homogeneous static force F is added such that

$$\eta\dot{x}(t) = -V'(x(t)) + F + \xi(t) \tag{A.18}$$

As a result the Brownian particle experiences a single effective potential $V_{eff}(x) = V(x) - xF$ where the symmetry is broken when $F \neq 0$. This leads to a nonzero current where $\eta\dot{x} < 0$ for $F < 0$ and $\eta\dot{x} > 0$ for $F > 0$.

APPENDIX B

Definitions

In this Appendix we define some of the terms which have been extensively used in this dissertation.

B.0.1 Interface

An interface is a boundary between phases. The 5 types of interfaces commonly encountered are: liquid-gas, liquid-liquid, liquid-solid, solid-solid and solid-gas. Since molecules at interfaces are subject to different interactions than those in the surrounding bulk phases, they exhibit unique behavior. The interfaces give rise to special forces that may be modified by the presence of amphiphilic substances called surfactants.

B.0.2 Surfactant

Surfactants or surface active agents are wetting agents containing molecules that have an energetic preference for the interface. These are usually organic compounds with *hydrophobic* and *hydrophillic* parts. These dissolve in organic solvents and adsorb at the interfaces. As a result they effect the intermolecular forces at the interface, i.e the interfacial tension as well as the surface tension in a liquid. The soluble surfactants may also assemble in the bulk liquid to form aggregates to form micelles. The concentration of the surfactants at which they begin to form micelles is called the critical micelle concentration (cmc). These surfactants are important in everyday life, in industry, at home and even in the biological entities. One of the most important surfactant in biological systems is dipalmitoylphosphatidylcholine(DPPC). DPPC is a major component of the surfactant composition of the lungs that aids in the process of breathing by forming a coating on the air sacs in the lungs, the Alveoli, where the gas exchange occurs. The study of the interfaces, the interfacial forces and surfactants is termed interfacial phenomenon.

B.0.3 Surface Tension

A molecule in the interior of a liquid is under attractive forces in all directions, the vector sum of these forces is zero. On the other hand a molecule at the surface of a liquid is acted on by a net inward cohesive force that is perpendicular to the surface. Hence it requires work to move molecules to the surface against this opposing force and the surface molecules have more energy than the interior. The surface tension of the liquid, σ is defined as the work done to bring enough molecules from inside the liquid to the surface to form one new

unit area of that surface.

$$\sigma = \delta F / \delta L$$

δF is the transverse elastic force to surface of length δL.

B.0.4 Surface Viscosity

The surface viscosity is a 2-dimensional analog of bulk viscosity. The surface shear viscosity reflects the resistance of a 2-dimensional film at an interface to flow under an applied shear stress. It is measured in the units of surface Poise (N/sm). Mathematically it is written as

$$\eta_s = \frac{tangential \quad force \quad per \quad unit \quad area}{rate \quad of \quad strain}$$

B.0.5 Faraday Effect

The Faraday effect is a magneto-optic effect discovered by Michael Faraday in 1845. When light passes through an optical piece in the presence of a magnetic field, the plane of polarization is rotated. The angle of rotation is empirically given by

$$\theta = VBL$$

where V is the Verdet constant, B is the magnetic field and L is the thickness of the optical piece. This phenomenon is a result of the asymmetry of the refractive index of left-handed and right-handed circularly polarized light in the presence of a magnetic field.

REFERENCES

[1] Z. Khattari, Y. Ruschel, H. Z. Wen, A. Fischer, and Th. M. Fischer. Compactification of a myelin mimetic langmuir monolayer upon adsorption and unfolding of myelin basic protein. *J. Phys. Chem. B*, 109:3402–3407, 2005.

[2] C. Mavroidis, A. Dubey, and M.L. Yarmush. Molecular machines. *Annu. Rev. Biomed. Eng.*, 6:363–395, 2004.

[3] G. Oster. *How protein motors convert chemical energy into mechanical work.* Wiley, New York, molecular motors edition, 2003.

[4] J. Howard. Molecular motors: Structural adaptations to cellular functions. *Nature*, 389:561–567, 1997.

[5] P. D. Vogel. Natures design of nanomotors. *European Journal Of Pharma. and Biopharma.*, 60:267–277, 2005.

[6] M. C. T. Fyfe and J. F. Stoddart. Synthetic supramolecular chemistry. *Acc. Chem. Res.*, 30:393–401, 1997.

[7] C. D. Chin, V. Linder, and S. K. Sia. Lab on a chip devices for global health: Past studies and future opportunities. *Lab-on-Chip*, 7:41–57, 2007.

[8] P. Yager, T. Edwards, E. Fu, K. Helton, K. Nelson, R. T. Milton, and B. H. Weigl. Microfluidic diagnostic technologies for global public health. *Nature*, 442:412–418, 2006.

[9] M. Toner and D. Irimia. Blood-on-a-chip. *Annu. Rev. Biomed Eng*, 7:77–103, 2005.

[10] G. M. Whitesides. The origins and the future of microfluidics. *Nature*, 442:368–373, 2006.

[11] J. W. Hong and S. R. Quake. Integrated nanoliter systems. *Nature Biotechnol*, 21:1179–1183, 2003.

[12] D. B. Weibel, M. Kruithof, S. Potenta, S. K. Sia, A. Lee, and G. M. Whitesides. Torque actuated valves for microfluidics. *Anal. Chem.*, 77(15):4726–4733, 2005.

[13] D. J. Laser and J. G. Santiago. A review of micropumps. *J. Micromech and Microeng.*, 15:R35–R64, 2004.

[14] J. M. Catchmark, S. Subramanian, and A. Sen. Directed rotational motion of microscale objects using interfacial tension gradients continually generated via catalytic reactions. *Small*, 1:202–206, 2005.

[15] Y. Hiratsuka, T. Tada, K. Oiwa, T. Kanayama, and T. Q. Uyeda. Controlling the direction of kinesin-driven microtubule movements along microlithographic tracks. *Biophysical Journal*, 81:1551, 2001.

[16] J. Clemmens, H. Hess, R. Lipscomb, Y. Hanein, K. F. Böhringer, C. M. Matzke, G. D. Bachand, B. C. Bunker, and V. Vogel. Mechanisms of microtubule guiding on microfabricated kinesin-coated surfaces: Chemical and topographic surface patterns. *Langmuir*, 19:10967–10974, 2003.

[17] Y. M. Huang, M. Uppalapati, W. O. Hancock, and T. N. Jackson. Microfabricated capped channels for biomolecular motor-based transport. *IEEE Trans. Adv. Packag.*, 28:564–570, 2005.

[18] H. Hess and V. Vogel. Molecular shuttles based on motor proteins: active transport in synthetic environments. *Rev. in Mol. Biotech.*, 82:67–85, 2001.

[19] R. Yasuda, H. Noji, K. Kinosita, and M. Yoshida. F1-atpase is a highly efficient molecular motor that rotates with discrete 120 steps. *Cell*, 93:1117–1124, 1998.

[20] K. Visscher, M. J. Schnitzer, and S. M. Block. Single kinesin molecules studied with a molecular force clamp. *Nature*, 400:184–189, 1999.

[21] M. G. L. van den Heuvel, M. P. de Graaff, and C. Dekker. Molecular sorting by electrical steering of microtubules in kinesin-coated channels. *Science*, 312:910–914, 2006.

[22] S. Diez, C. Reuther, C. Dinu, R. Seidel, M. Mertig, W. Pompe, and J. Howard. Stretching and transporting dna molecules using motor proteins. *Nano. Lett.*, 3:1251–1254, 2003.

[23] H. Hess, J. Clemmens, C. Brunner, R. Doot, S. Luna, K. H. Ernst, and V. Vogel. Molecular self-assembly of "nanowires" and "nanospools" using active transport. *Nano. Lett.*, 5:629–633, 2005.

[24] H. Hess. Toward devices powered by biomolecular motors. *Science*, 312():860–861, 2006.

[25] R. A. Bissell, E. Cordova, A. E. Kaifer, and J. F. Stoddart. A chemically and electrochemically switchable molecular shuttle. *Nature*, 369:133–137, 1994.

[26] A. Alteri, F.G.Gatti, E. R. Kay, D.A. Leigh, D.Martel, F. Paolucci, A. M. Z. Slawin, and J. K. Y. Wong. Electrochemically switchable hydrogen-bonded molecular shuttles. *J. Am. Chem. Soc.*, 125:8644–8654, 2003.

[27] S. Nygaard, B. W. Laursen, A. H. Flood, C. N. Hansen, J. O. Jeppesen, and J. F. Stoddart. Quantifying the working stroke of tetrathiafulvalene-based electrochemical-lydriven linear motor-molecules. *Chem. Comm.*, pages 144–146, 2006.

[28] J. N. Lowe, S. Silvi, J. F. Stoddart, J. D. Badjic, and A. Credi. A mechanically interlocked bundle. *Chem. Euro. J.*, 10:1926–1935, 2004.

[29] W. Browne and B. L. Feringa. Making molecular motors work. *Nature Nanotech.*, 1:25–35, 2006.

[30] T. R. Kelly, H. De Silva, and R. A. Silva. Undirectional rotary motion in a molecular system. *Nature*, 401:150–152, 1999.

[31] V. Balzani, M. Clemente-Leon, A. Credi, B. Ferrer, M. Venturi, A. H. Flood, and J. F. Stoddart. Autonomous artificial nanomotor powered by sunlight. *Proc. Natl. Acad. Sci.*, 103:1178–1183, 2006.

[32] Y. Morin J. F. Shirai and J. M. Tour. En route to a motorized nanocar. *Org. Lett*, 8:1713–1716, 2006.

[33] J. Berná, D. A. Leigh, M. Lubomska, S. M. Mendoza, E. M. Pérez, P. Rudolf, G. Teobaldi, and F. Zerbetto. Macroscopic transport by synthetic molecular machines. *Nature Mat.*, 4:643–710, 2005.

[34] R. Eelkema, M. M. Pollard, J. Vicario, N. Katsonis, B. S. Ramon, C. W. M. Bastiaansen, D. J. Broer, and B. L. Feringa. Molecular machines: Nanomotor rotates microscale objects. *Nature*, 440:163, 2006.

[35] P. G. Saffman and M. Delbrück. Brownian-motion in biological-membranes. *Proc. Nat. Acad. Sci. (USA)*, 72:311–313, 1975.

[36] T. E. Mallouk, A. Sen, and W. F. Paxton. Catalytic movement of nanoscale objects. *Chem. Eur. J.*, 11:6462–6470, 2005.

[37] T. Harder and K. Simons. Caveolae, digs, and the dynamics of sphingolipid-cholesterol microdomains. *Curr. Op. Cell Biol.*, 9:534–542, 1997.

[38] P. Girard, J. Prost, and P. Bassereau. Passive or active fluctuations in membranes containing proteins. *Phys. Rev. Lett.*, 94:088102, 2005.

[39] W. F. Paxton, K. C. Kistler, C. C. Olmeda, A. Sen, St. S. K. Angelo, Y. Cao, T. E. Mallouk, P. E. Lammert, and V. H. Crespi. Catalytic nanomotors: Autonomous movement of striped nanorods. *J. Am. Chem. Soc.*, 126:13424–13431, 2004.

[40] R. Golestanian, T. B. Liverpool, and A. Adjari. Propulsion of a molecular machine by asymmetric distribution of reaction products. *Phys. Rev. Lett.*, 94:220801, 2005.

[41] B. A. Grzybowski, H. A. Stone, and G. M. Whitesides. Dynamic selfassembly of magnetized, millimetre-sized objects rotating at a liquid air interface. *Nature*, 405:1033–1036, 2000.

[42] B. A. Grzybowski and G. M. Whitesides. Three-dimensional dynamic self-assembly of spinning magnetic disks: Vortex crystals. *J. Phys Chem. B*, 106:1188–1194, 2002.

[43] P. Lenz, J. F. Joanny, F. Jülicher, and J. Prost. Membranes with rotating motors. *Phys. Rev. Lett.*, 91:108104, 2003.

[44] S. Ramaswamy, J. Toner, and J. Prost. Nonequilibrium fluctuations, traveling waves, and instabilities in active membranes. *Phys. Rev. Lett.*, 84:3494–3497, 2000.

[45] M. J. Kim and K. S. Breuer. Enhanced diffusion due to motile bacteria. *Phys. Fluids*, 16:L78–L81, 2004.

[46] N. Darnton, L. Turner, K. Breuer, and H. C. Berg. Moving fluid with bacterial carpets. *Biophys. J.*, 86:1863–1870, 2004.

[47] H. A. Stone, A. D. Stroock, and A. Ajdari. Engineering flows in small devices microfluidics toward a lab-on-a-chip. *Annual Review of Fluid Mechanics*, 36:381–411, 2004.

[48] D. A. Edwards, H. Brenner, and D. T. Wasan. *Interfacial transport processes and rheology*. Butterworth-Heinemann Series in Chemical Engineering. Butterworth-Heinemann, 1991.

[49] T. M. Kline, W. F. Paxton, T. E. Mallouk, and A. Sen. Catalytic nanomotors: Autonomous movement of striped metallic nanorods. *Angewante Chem*, 44:744–746, 2005.

[50] R. S. Ghaskadvi and M. Dennin. Effect of subphase ca^{++} ions on the viscoelastic properties of langmuir monolayers. *J. Chem. Phys.*, 111:3675–3678, 1999.

[51] R. S. Ghaskadvi and M. Dennin. Alternate measurement of the viscosity peak in heneicosanoic acid monolayers. *Langmuir*, 16:10553–10555, 2000.

[52] J. Ignes-Mullol and D. K. Schwartz. Shear-induced molecular precession in a hexatic langmuir monolayer. *Nature*, 410:348–351, 2001.

[53] A. T. Ivanova, J. Ignes-Mullol, and D. K. Schwartz. Microrheology of a sheared langmuir monolayer: Elastic recovery and interdomain slippage. *Langmuir*, 17:3406–3411, 2001.

[54] G. B. Bantchev and D. K. Schwartz. Surface shear rheology of betacasein layers at the air/solution interface: Formation of a two dimensional physical gel. *Langmuir*, 19:2673–2682, 2003.

[55] M. Twardos and M. Dennin. Comparison of steady-state shear viscosity and complex shear modulus in langmuir monolayers. *Langmuir*, 19:3542–3544, 2003.

[56] C. Barentin, C. Ybert, J. M. diMeglio, and J. F. Joanny. Surface shear viscosity of gibbs and langmuir monolayers. *J. Fluid. Mech*, 397:331–349, 1999.

[57] H. A. Stone and A. Ajdari. Hydrodynamics of particles embedded in a flat surfactant layer overlying a subphase of finite depth. *J. Fluid. Mech*, 369:151–173, 1998.

[58] D. Schwartz, C. M. Knobler, and R. Bruinsma. Direct observation of langmuir monolayer flow-through a channel. *Phys. Rev. Lett.*, 73:2841–2844, 1994.

[59] J. F. Klingler and H. McConnell. Brownian-motion and fluid-mechanis of lipid monolayer domains. *J. of Phys. Chem.*, 67:6096–6100, 1993.

[60] P. Steffen, P. Heinig, S. Wurlitzer, Z. Khattari, and Th. M. Fischer. The translational and rotational drag on langmuir monolayer domains. *J. Chem. Phys.*, 115:994–997, 2001.

[61] M. Sickert and F. Rondelez. Shear viscosity of langmuir monolayers in the low-density limit. *Phys. Rev. Lett.*, 90/94:126104/139604, 2003/2004.

[62] S. Wurlitzer, H. Schmiedel, and Th. M. Fischer. Electrophoretic relaxation dynamics of domains in langmuir monolayers. *Langmuir*, 18:4393–4400, 2002.

[63] Th. M. Fischer. Comment on: Shear viscosity of langmuir monolayers in the low-density limit. *Phys. Rev. Lett.*, 92:139603, 2004.

[64] M. F. Shlesinger, B. J. West, and J. Klafter. Levy dynamics of enhanced diffusion: application to turbulence. *Phys. Rev. Lett.*, 58:1100, 1987.

[65] J. M. Burgers. Second report on viscosity and plasticity. Technical report, North-Holland Publ. Co, Amsterdam, 1938.

[66] F. Bouchama and J. M. di Meglio. Two-dimensional rheology of soap films. *J. Phys.: Condens. Matter*, 8:9525–9529, 1996.

[67] S. Fourier-Bidoz, A. C. Arsenault, I. Manners, and G. A. Ozin. Synthetic self-propelled nanorotors. *Chem. Comm.*, pages 741–743, 2005.

[68] R. Golestanian, T. B. Liverpool, and A. Adjari. Propulsion of a molecular machine by asymmetric distribution of reaction products. *Phys. Rev. Lett.*, 94:220801(1–4), 2005.

[69] L. E. Helseth, T. Backus, T. H. Johansen, and Th. M. Fischer. Colloid crystallization and transport in stripes and mazes. *Langmuir*, 21:7518–7523, 2005.

[70] R. P. Blakemore. Magnetotactic bacteria. *Science*, 190:377–379, 1975.

[71] D. A. Bazylinski and B. Frankel. Magnetosome formation in prokaryotes. *Nature Microbiology*, 2:217–230, 2004.

[72] E. Wajnberg, L. H. de Souza Solva, H. G. P de Barros, and D. M. S. Esquivel. A study of magnetic properties of magnetotactic bacteria. *Biophys. J.*, 50:451–455, 1986.

[73] Y. Sahoo, A. Goodarzi, M. T. Swihart, T. Y. Ohulchanskyy, N. Kaur, E. P. Furlani, and P. N. Prasad. Aqueous ferrofluid of magnetite nanoparticles: Fluorescence labeling and magnetophoretic control. *J. Phys. Chem. B*, 109:3879–3885, 2005.

[74] U. Heyen and D. Schuler. Growth and magnetosome formation by microaerophilic magnetospirillum strains in an oxygen-controlled fermentor. *Appl Microbiol Biotechnol*, 61:536–544, 2003.

[75] A. J Kalmijn and R. P. Blakemore. The magnetic behavior of mud bacteria. In *Proceedings in life science. Animal migration, navigation and homing*, pages 354–355. Springer-Verlag KG, 1978.

[76] M. Esashi, T. Ono, and S. Tanaka. Micro industry equipments. *JSME Int. J. Series B - Fluids and Thermal Eng.*, 47:429–438, 2004.

[77] N. Yazdi, F. Ayazi, and K. Najafi. Micromachined inertial sensors. *Proc. of the IEEE.*, 86(8):1640–1659, 1998.

[78] S. Lee, S. Park, and J. Kim. Surface/bulk micromachined single-crystalline-silicon micro-gyroscope. *J. of Micromelectromechanical Sys.*, 9(4):557–567, 2000.

[79] M. Schliwa. *Molecular Motors*. Wiley-VCH, Weinheim, 2002.

[80] A. R. Pease, J. O. Jeppesen, J. F. Stoddart, Y. Luo, C. P. Collier, and J. R. Heath. Switching devices based on interlocked molecules. *Acc. Chem. Res.*, 34(6):433–444, 2001.

[81] R. Ballardini, V. Balzani, A. Credi, M. T. Gandolfi, and M. Venturi. Artificial molecular-level machines: Which energy to make them work? *Acc. Chem. Res.*, 34(6):445–455, 2001.

[82] C. M. Keaveney and D. A. Leigh. Shuttling through anion recognition. *Angew. Chem. Int. Ed.*, 43(10):1222–1224, 2004.

[83] M. F. Hawthorne, J. I. Zink, J. M. Skelton, M. J. Bayer, C. Lui, E. Livshits, R. Baer, and D. Neuhauser. Electrical or photocontrol of the rotary motion of a metallacarborane. *Science*, 303:1849–1851, 2004.

[84] Z. Dominguez, T. A. V. Khuong, H. Dang, C. N. Sanrame, J. E. Nunez, and M. A. Garcia-Garibay. Molecular compasses and gyroscopes with polar rotors: Synthesis and characterization of crystalline forms. *J. Am. Chem. Soc.*, 125(29):8827–8837, 2003.

[85] N. L. Koumura, R. A. van Delden, R. W. J. Zijlstra, N. Harada, and B. L. Feringa. Light-driven monodirectional molecular rotor. *Nature*, 401:152–155, 1999.

[86] B. L. Feringa, N. L. Koumura, R.A. van Delden, and M. K. J. ter Wiel. Light-driven molecular switches and motors. *Appl. Phys. A.*, 75:301–308, 2002.

[87] D. A. Leigh, J. K. Y. Wong, F. Dehez, and F. Zerbetto. Unidirectional rotation in a mechanically interlocked molecular rotor. *Nature*, 424:174–179, 2003.

[88] R.D. Astumian. Thermodynamics and kinetics of a brownian motor. *Science*, 276:917–922, 1997.

[89] R. F. Fox. Rectified brownian movement in molecular and cell biology. *Phys. Rev. E*, 57:2177–2203, 1998.

[90] L. I. McCann, M. Dykman, and B. Golding. Thermally activated transitions in a bistable three-dimensional optical trap. *Nature*, 402:785–787, 1999.

[91] L. Ghislain and W. W. Webb. *Opt. Lett*, 18:1678, 1993.

[92] L. Gammaitoni, P. Hanggi, P. Jung, and F. Marchesoni. Stochastic resonance. *Rev. Mod. Phys.*, 70:223–287, 1998.

[93] S. Broersma. Rotational diffusion constant of a cylindrical particle. *J. Chem. Phys.*, 32:1626, 1960.

[94] S. Seeger, S. Monajembashi, K. J. Hutter, G. Futterman, J. Wolfrum, and K. O. Greulich. Applications of laser optical tweezers in immunology and molecular-genetics. *Cytometry*, 12:497–504, 1991.

[95] B. J. Battersby, G. A. Lawrie, A. P. R. Johnston, and M. Trau. Optical barcoding of colloidal suspensions: applications in genomics, proteomics and drug discovery. *Chem. Comm.*, 14:1435–1441, 2002.

[96] A. Terray, J. Oakey, and D. W. M. Marr. Microfluidic control using colloidal devices. *Science*, 296:1841–1844, 2002.

[97] F. C. MacKintosh and C. F. Schmidt. Microrheology. *Curr. Op. Coll. Int. Sci*, 4:300–307, 1999.

[98] J. C. Crocker, M. T. Valentine, E. R. Weeks, P. D. Kaplan, A. G. Yodh, and D. A. Weitz. Two-point microrheology of inhomogeneous soft materials. *Phys. Rev. Lett*, 85:889–891, 2000.

[99] S. Yamada, D. Wirtz, and S. C. Kuo. Mechanics of living cells measured by laser tracking microrheology. *Biophys. J*, 78:1736–1747, 1997.

[100] F. Gittes, B. Schnurr, P. D. Olmsted, F. C. MacKintosh, and C. F. Schmidt. Microscopic viscoelasticity: Shear moduli of soft materials determined from thermal fluctuations. *Phys. Rev. Lett.*, 79:3286–3289, 1997.

[101] T. G. Mason, K. Ganesan, J. H. van Zanten, D. Wirtz, and S. C. Kuo. Particle tracking microrheology of complex fluids. *Phys. Rev. Lett.*, 79:3282–3285, 1997.

[102] A. Palmer, T. G. Mason, J. Y. Xu, S. C. Kuo, and D. Wirtz. Diffusing wave spectroscopy microrheology of actin filament networks. *Biophys. J*, 79:1063–1071, 1999.

[103] V. I. Furdui, J. K. Kariuki, and D. J. Harrison. Microfabricated electrolysis pump system for isolating rare cells in blood. *J. Micromech. Microeng.*, 13:S164–S170, 2003.

[104] R. H. Liu, J. N. Yang, R. Lenigk, J. Bonanno, and P. Grodzinski. Microfluidics for diagnostics. *Annal. Chem.*, 76:1824, 2004.

[105] S. Lindquist. The heat shock response. *Annal. Rev. Biochem.*, 55:1151–1191, 1986.

[106] M. Babincova, D. Leszczynska, P. Sourivong, and P. Babinec. Selective treatment of neoplastic cells using ferritin-mediated electromagnetic hyperthermia. *Med. Hypotheses*, 54:177–179, 2000.

[107] I. Hilger, W. Andra, R. Hergt, R. Hiergeist, H. Schubert, and W. A. Kaiser. Electromagnetic heating of breast tumors in interventional radiology: In vitro and in vivo studies in human cadavers and mice. *Radiology*, 218:550–575, 2001.

[108] I. Hilger, K. Frhauf, W. Andra, R. Hiergeist, R. Hergt, and W. A. Kaiser. Heating potential of iron oxides for therapeutic purposes in interventional radiology. *Acad. Radiology*, 9:198–202, 2002.

[109] A. K. Gupta and M. Gupta. Cytotoxicity suppression and cellular uptake enhancement of surface modified magnetic nanoparticles. *Biomaterials*, 26:1565–1573, 2005.

[110] P. Reimann, R. Kawai, C. van den Broeck, and P. Hänggi. Coupled brownian motors: Anomalous hysteresis and zero-bias negative conductance. *Europhys. Lett.*, 45(5):545–551, 1999.

[111] P. Reimann and P. Hänggi. Introduction to the physics of brownian motors. *Applied Physics A*, 75:169–178, 2002.

[112] Th. M. Fischer, P. Dhar, and P. Heinig. The viscous drag of spheres and filaments moving in membranes or monolayers. *J. Fluid Mech.*, 558:451–475, 2006.

[113] J. T. Petkov, N. D. Denkov, K. Danov, O. D. Velev, R. Aust, and F. Durst. Measurement of the drag coefficient of spherical particles attached to fluid interfaces. *J. Coll. Int. Sci.*, 172:147–154, 1995.

[114] M. B. Forstner, J. A. Käs, and D. S. Martin. Single lipid diffusion in langmuir monolayers. *Langmuir*, 17:567–570, 2001.

[115] M. B. Forstner, D. S. Martin, A. M. Navar, and J. A. Käs. Simultaneous single-particle tracking and visualization of domain structure on lipid monolayers. *Langmuir*, 19:4876–4879, 2003.

[116] R. Dimova, C. Dietrich, A. Hadjiisky, K. Danov, and B. Pouligny. Falling ball viscosimetry of giant vesicle membranes: finite-size effects. *Eur. Phys. J. B*, 12:589–598, 1999.

[117] R. Dimova, C. Dietrich, A. Hadjiisky, K. Danov, and B. Pouligny. *Motion of particles attached to giant vesicles: falling ball viscosimetry and elasticity measurements on lipid membranes*. John Willey & Sons, Ltd., 1999.

[118] R. Dimova, K. Danov, B. Pouligny, and I. B. Ivanov. Drag of a solid particle trapped in a thin film or at an interface, influence of the surface viscosity and elasticity. *J. Coll. Int. Sci.*, 226:35–43, 2000.

[119] A. Pralle, P. Keller, E. L. Florin, K. Simons, and J. K. H. Horber. Sphingolipid-cholesterol rafts diffuse as small entities in the plasma membrane of mammalian cells. *J. Cell. Bio.*, 148:997–1007, 2000.

[120] B. D. Hughes, B. A. Pailthorpe, and L. R. White. The translational and rotational drag on a cylinder moving in a membrane. *J. Fluid Mech.*, 110:349–372, 1981.

[121] R. Peters and R. J. Cherry. Lateral and rotational diffusion of bacteriorhodopsin in lipid bilayers: Experimental test of saffman-delbrck equations. *Proc. Nat. Acad. Sci. USA*, 79:4317–4329, 1982.

[122] K. Danov, R. Dimova, and B. Pouligny. Viscous drag of a solid sphere straddling a spherical or flat surface. *Phys. of Fluids*, 12:2711–2722, 2000.

[123] M. G. Nikolaides, A. R. Bausch, M. F. Hsu, A. D. Dinsmore, M. P. Brenner, and D. A. Weitz. Electric-field-induced capillary attraction between like-charged particles at liquid interfaces. *Nature*, 420:299–301, 2002.

[124] K. D. Danov, P. A. Kralchevsky, and M. P. Boneva. Electrodipping force acting on solid particles at a fluid interface. *Langmuir*, 20:6139–6151, 2004.

[125] M. E. O'Neill, K. B. Ranger, and Brenner H. Slip at the surface of a translating-rotating sphere bisected by a free surface bounding a semi-infinite viscous fluid: Removal of the contact-line singularity. *Phys. Fluids*, 29:913–924, 1986.

[126] C. Huh and L. I. Scriven. Hydrodynamic model of steady movement of a solid/liquid/fluid contact line. *J. Coll. Int. Sci.*, 35:85–101, 1971.

[127] E. B. Dussan and S. H. Davis. Motion of a fluid-fluid interface along a solid-surface. *J. Fluid Mech.*, 65:75, 1974.

[128] P. Hänggi and H. Thomas. Stochastic processes: Time-evolution, symmetries and linear response. *Phys. Rep*, 88:207, 1982.

BIOGRAPHICAL SKETCH

Prajnaparamita Dhar

The author was born on June 27^{th}, 1979 in Kolkata, India. She received her Bachelors degree in Physics(Honors) from Presidency College, Calcutta. She went on to receive a Masters Degree in Physics from Indian Institute of Technology, Bombay, India. After this she moved to Florida State University to pursue a Ph.D in Physical Chemistry at the Department of Chemistry and Biochemistry. Her research interests include Experimental Soft Matter and biophysics.

Parts of the research work outlined in this dissertation have been published in: **Publications**:

1. **P. Dhar**, P. Tierno, J.Hare, T. Johansen, T. Fischer; *Curvature driven motion of mouse macrophages in a pulsating magnetic film ratchet* ***J. Phys. Chem. B*** , 111, 13097-13100(2007).

2. **P. Dhar**, C. Swayne, T. Kline, A. Sen, T. Fischer,; *Orientations of over damped magnetic nano-gyroscopes* **Nano Letters**, 7, 1010-1012(2007).

3. **P. Dhar**, Y. Cao, T. Kline, P.Pal , C. Swanye, T. Fischer, B Miller, T. Mallouk, A Sen, T Johensen *Autonomously moving Local Nanoprobes in Heterogeneous Magnetic Fields* **J. Phys. Chem. C**, 111, 3607-3613(2007).

4. **P. Dhar** Th. M. Fischer, Y. Wang, T. E. Mallouk, W. E. Paxton and A. Sen, *Autonomously moving nanorods at a viscous interface*, **Nano Letters** 6(1), 66-72(2006).

5. Th. M. Fischer, **P. Dhar**, Peter Heinig, *The viscous drag of sphere and filaments moving in membranes or monolayer* , **J. Fluid Mech.** .558, 451-475(2006).

Seminars and Conferences:

1. **Physical Chemistry Divisional Seminar**
   Title: *Autonomous Motion of Active Components at Interfaces*
   Date: 3rd Dec, 2007.

2. **Gordon Research Conference**, Physics & Chemistry Of Microfluidics,
   Selected Student Poster Oral Presentation: *Microfluidics in channels without walls*
   Date: July15th-July 20th, 2007.

3. **FAME 2007**
   Title: *Autonomously moving Local Nanoprobes in Heterogeneous Magnetic Fields*
   Date: May 11, 2007.

4. **MRS Spring 2007**
   Title: *Autonomously moving Local Nanoprobes in Heterogeneous Magnetic Fields*
   Date: April 13th, 2007

5. **FAME 2006**

   Title: *Autonomous motion of Nanorods at a Viscous Interface.*

   Date: May 12th, 2006.

6. **Physical Chemistry Divisional Seminar**

   Title: *Autonomous Motion of Nanorods at a Viscous Interface*

   Date: 28th Nov, 2005.